Technische Universität München
Physik-Department
Lehrstuhl für Biophysik E22

The mechanics of asymmetric spindle positioning in the *Caenorhabditis elegans* embryo

Stephan W. Grill

Vollständiger Abdruck der von der Fakultät für Physik der Technischen Universität München zur Erlangung des akademischen Grades eines

Doktors der Naturwissenschaften

genehmigten Dissertation.

Vorsitzender:		Univ.-Prof. Dr. H. Friedrich
Prüfer der Dissertation:	1.	Univ.-Prof. Dr. E. Sackmann
	2.	Univ.-Prof. Dr. M. Schliwa, Ludwig-Maximilians-Universität München

Die Dissertation wurde am 04.02.2002 bei der Technischen Universität München eingereicht und durch die Fakultät für Physik am 28.03.2002 angenommen.

for my parents

Contents

1 Introduction

Self-reproduction is the most fundamental characteristic of cells [1]. Cells reproduce by dividing in two, with each producing two functional copies of itself upon completion of the cycle of cell division. These daughter cells then continue to grow and divide, giving rise to a population of cells formed by the growth and division of a single parent cell. This process allows a single bacterium to form a colony consisting of millions of progeny during overnight incubation. In more complex cases, a single fertilized egg develops into more than 10^{13} cells forming the human body.

Cell division must be carefully coordinated and regulated both with respect to cell growth and DNA replication and segregation. Defects in these processes are a common cause of the abnormal proliferation of cancer cells, explaining the close relationship of the research on cell division to the studies of cancer.

The work presented focuses on *asymmetric* cell division, whereby one mother cell gives rise to two daughter cells with different developmental fates. Both biological and biophysical techniques are used to gain insight into the *mechanics* of asymmetric cell division, which is at the heart of generating cellular diversity in a developing organism. In particular, the mechanical principles contributing to the asymmetric placement of the mitotic spindle in the single cell stage *Caenorhabditis elegans* embryo are investigated.

This chapter is divided into three parts: The first part is a general introduction (based on [1, 2]), followed by a more detailed review of processes required for cell division. Second, the biological model organism *Caenorhabditis elegans* is introduced. Third, both established biophysical techniques that allow for the study of the mechanics of a complex biological process as well as the experimental setup are presented.

Some of the figure legends contain references to quicktime movies, which can be found on the compact disc attached to the hardcover of this document.

1.1 Cell division

This section is separated into a general introduction to the biology of cell division (focussing on spindle positioning), and a review of properties of components and mechanisms involved in spindle positioning.

1.1.1 Biological features of cell division

The division cycle of eukaryotic cells is divided into *interphase* and *mitosis*. During mitosis the chromosomes segregate and are distributed into the two daughter cells. *Cytokinesis* turns the two blastomeres into separate entities. In a typical non-embryonic cell, mitosis lasts only about 5% of the cell cycle. The remaining 95% is spent in interphase, which is defined as the time between mitoses. Interphase is divided into three parts, G_1 (gap 1), which is the gap between mitosis and the initiation of DNA replication, S phase (synthesis) corresponding to the time of DNA replication, and G_2 (gap 2), the time between the end of DNA replication and the beginning of M phase (mitosis).

The duration of cell cycle phases varies considerably in different kinds of cells. Typical rapidly proliferating human cells go through a complete cycle in a day, whereas much shorter cell cycles (less than 30 minutes) occur in early embryo cells shortly after fertilization [1]. There is no G_1 and G_2 phase in these cells, instead early embryonic cells go through rapid rounds of division, alternating between S and M phases only.

Mitosis

Mitosis is conventionally divided into four stages (see figure 1.1 for an animal cell).

Prophase starts with the appearance of condensed chromosomes, each of which consists of two sister chromatids (the daughter DNA molecules produced in S phase). In higher eukaryotes the condensed sister chromatids are connected at the centromere. *Spindle microtubules* attach to the kinetochore, which is bound to the centromeric DNA sequences and consists of many proteins. In addition to chromosome condensation a *mitotic spindle* forms during late prophase. The mitotic spindle is a highly dynamic structure consisting of two *centrosomes* and *microtubules* responsible for chromosome segregation and cleavage plane specification. In higher eukaryotes, prophase ends with the breakdown of the nuclear envelope.

Following prophase, the cell enters *prometaphase*, where the microtubules of the spindle attach to the kinetochores of the condensed chromosomes.

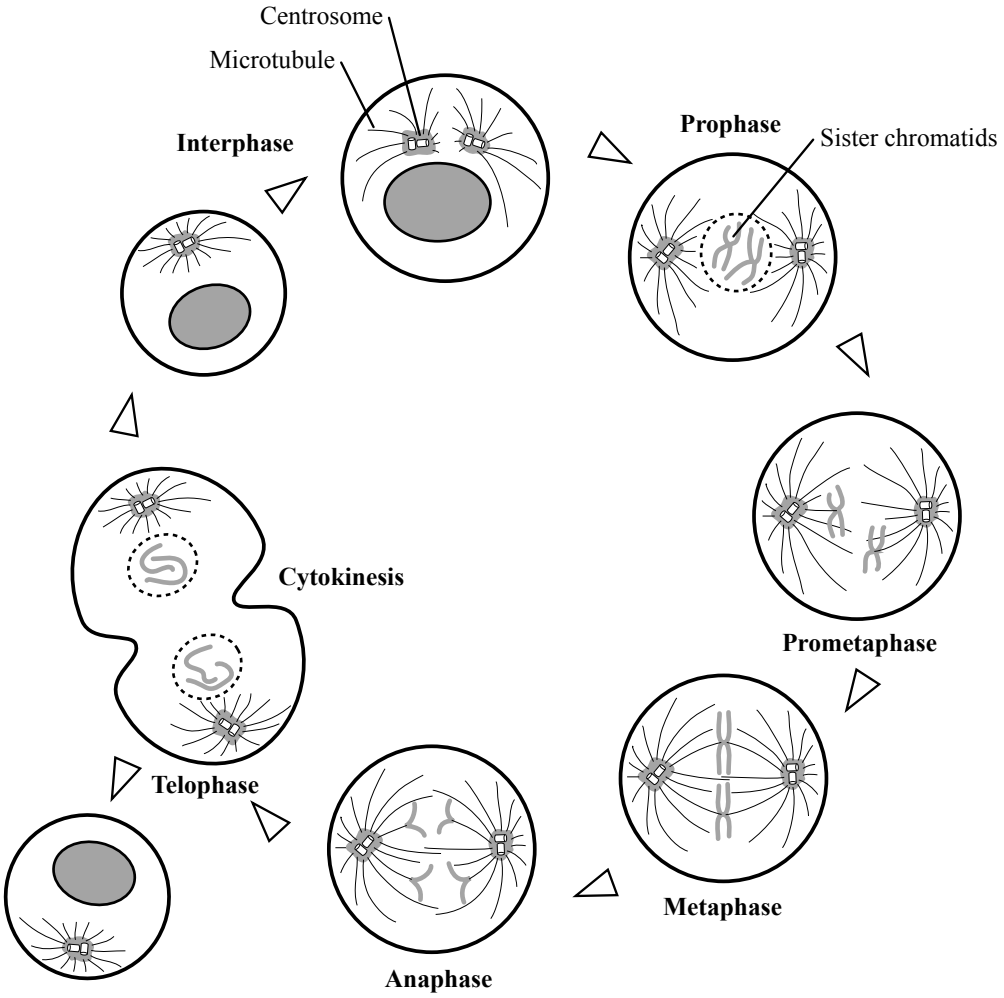

Fig. 1.1 Stages of mitosis in an animal cell. Chromosomes condense during prophase. Centrosomes move to opposite sides of the nucleus to initiate the formation of the mitotic spindle. Breakdown of the nuclear envelope, allowing spindle microtubules to attach to the kinetochores of chromosomes. During prometaphase chromosomes shuffle back and forth between the centrosomes and the center of the cell, eventually aligning in the center of the spindle at metaphase. The sister chromatids separate and move to opposite poles of the spindle during anaphase A. Following spindle elongation (anaphase B), mitosis ends with the reformation of the nuclear envelope and the decondensation of chromosomes during telophase. Cytokinesis creates two independent interphase daughter cells, each receiving one centrosome which duplicates prior to the next mitosis.

The kinetochores of sister chromatids are oriented on opposite sides of the chromosomes, allowing microtubules emanating from opposing poles of the spindle to attach to them. The chromosomes are forced to align in the center of the spindle on the *metaphase plate* during *metaphase*.

The transition from metaphase to *anaphase A* is triggered by the breakage of the link between sister chromatids, allowing them to separate and to move towards the opposite poles of the spindle. The spindle then elongates during *anaphase B*. Mitosis ends with *telophase*, during which nuclei reform and chromosomes decondense. Cytokinesis lasts from late anaphase throughout telophase, resulting in the formation of two separate interphase daughter cells.

Cytoskeleton

During mitosis the cell undergoes a dramatic change in multiple cellular components, one of the most remarkable being the complete reorganization of the *cytoskeleton* of the cell. The cytoskeleton is commonly defined as a network of protein filaments extending throughout the cytoplasm of eukaryotic cells. It provides a structural framework for the cell and serves as a scaffold determining cell shape as well as the general organization of the cytoplasm. The cytoskeleton has many functions, among which are the movement of whole cells and the movement of objects within cells (e.g. organelles or mitotic chromosomes). Importantly, the cytoskeleton is a highly dynamic structure responsible for the complete structural reorganization of a cell during mitosis.

The cytoskeleton is composed of three principal types of protein filaments: *actin filaments*, *intermediate filaments*, and *microtubules*. Actin polymerizes to form actin filaments, which are thin, flexible fibers approximately 7 nm in diameter and up to several μm in length. These organize into higher-order structures. A number of actin-binding proteins govern the assembly, disassembly and the association of actin filaments with other cell structures. Actin filaments are present beneath the cell surface, where a network providing mechanical support and determining cell shape is formed. Furthermore, actin filaments govern cytokinesis, where an actin *contractile ring* pinches off the two daughter cells, marking the end of cell division.

Intermediate filaments have a diameter of about 10 nm. In contrast to actin filaments they are not directly involved in cell movements, but play a structural role and provide mechanical support.

Microtubules are rigid hollow rods with a diameter of approximately 25 nm. Similar to actin filaments they are highly dynamic structures undergoing continuous assembly and disassembly. They function to determine cell shape and are involved in a variety of cell movements (e.g. some forms of

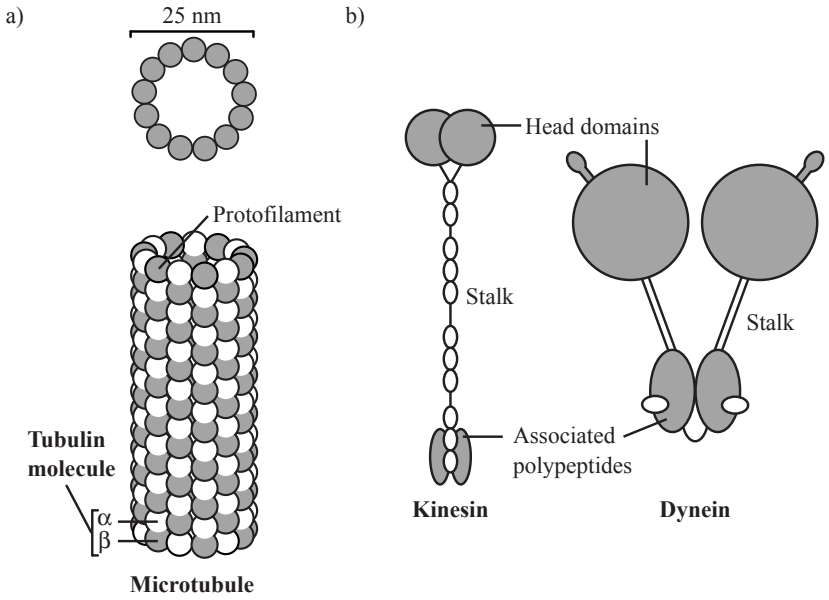

Fig. 1.2 Microtubules and motor proteins. a), Dimers of α- and β-tubulin polymerize into 13 protofilaments assembled around a hollow core to form microtubules. b), Conventional kinesin on the left, cytoplasmic dynein on the right. Both motors consist of a dimer of two heavy chains with catalytic domains, stalk domains, and associated polypeptides. The "antenna" extending from each dynein head domain contains the microtubule binding site. For kinesin, the binding domain is part of the compact head.

cell locomotion and the intracellular transport of organelles). Importantly, microtubules build up the mitotic spindle.

Microtubules are composed of *tubulin*, a dimer consisting of two closely related 55 kD polypeptides, α-tubulin and β-tubulin. In addition, a third type of tubulin (γ-tubulin) specifically localizes close to the centrosome where it initiates microtubule assembly.

Tubulin dimers polymerize to form microtubules, which generally consist of 13 linear protofilaments assembled around a hollow core (figure 1.2). The protofilaments are arranged in parallel, consisting of head-to-tail arrays of tubulin dimers. Consequently, a microtubule is a polar structure with two distinct ends: a fast growing plus end and a slow growing minus end. The intrinsic polarity of microtubules is an important feature dictating the direction of movement along microtubules.

Motor proteins

Microtubules participate in a variety of cellular movements. Importantly, they serve as tracks upon which *motor proteins* walk by utilizing energy derived from ATP hydrolysis to generate force. There are in principal two large families of motor proteins powering the variety of microtubule-based movements, *kinesins* and *dyneins* [3, 1].

Motor proteins possess a catalytic domain, also referred to as the "head", characterized by an ATP- and a microtubule-binding site (see figure 1.2). The microtubule-binding domain is small for kinesins (about 350 amino acids) and relatively large for dyneins (over 4000 amino acids). Outside the motor domain the two motors differ even more, suggesting that functional diversity emerges from the non-motor domains.

Some members of the kinesin family (e.g. conventional kinesin itself) move along microtubules in the plus end direction, whereas others move in the opposite direction. The members differ in their tails, thereby specifying for different types of "cargo" (vesicles, organelles, chromosomes). However, all members of the dynein family move towards the minus ends of microtubules. Again, each cytoplasmic dynein may transport a specific type of cargo.

Motors play an important role in spindle-assembly. Crosslinking motors like bipolar kinesins (a motor protein consisting of two linked conventional kinesins) or asymmetric crosslinkers with microtubules for cargo (see figure 1.3 for an example) can help focus microtubules. These assemble into organized structures with the minus ends of all microtubules arranged together (*spindle poles*) [4, 5, 6]. Dynein has been suggested to be involved in spindle positioning, where a dynein molecule attached to the actin cortex can exert a force on a spindle pole by walking along an astral microtubule (e.g. [4]).

It is clear that the biophysical properties of motor proteins, such as the speed of movement as a function of the load force, the average time of attachment to a microtubule (processivity), or the dependency of the speed on the concentration of ATP, together with the properties of microtubules play an immense role in spindle assembly, chromosome segregation and spindle positioning. Modifications of a specific parameter for a population of motor proteins can result in a different steady-state solution for the whole system [7, 8, 9].

Centrosome

Microtubules usually extend outward from a *microtubule-organizing center* (MTOC), to which the minus ends of microtubules are anchored. In animal cells, the major MTOC is the centrosome, which is located close to the nu-

cleus during interphase. At mitosis, the centrosome has duplicated and an array of *astral microtubules* radiates outward from each centrosome-containing MTOC. This focused structure of microtubules at metaphase and anaphase is referred to as a *spindle pole* or a *microtubule aster*.

Centrosomes take part in the process of spindle assembly, which is thought to be governed by two pathways: self-assembly of microtubules and motor proteins, and spatially confined centrosomal nucleation of microtubules. Both of these manage to establish polarity within the microtubule cytoskeleton as all microtubule minus-ends are located at the spindle pole. Centrosomal nucleation plays a large role in many animal cells. In mouse fibroblasts, for example, microtubules grow outward from the centrosome following disassembly of microtubules by treatment with colcemid [10].

The centrosomes of most animal cells contain a pair of *centrioles*, which are surrounded by a meshwork of *pericentriolar material* [11]. Centrioles are cylindrical structures built of nine triplets of microtubules. However, the capacity of centrosomes to assemble microtubules comes from within the pericentriolar material, where γ-tubulin is localized. Complexes of γ-tubulin form ring-structures with a diameter similar to that of a single microtubule. These structures contain between 10 and 13 γ-tubulin molecules and serve as nucleation sites for the assembly of microtubules.

In summary, microtubule-organizing centers are essential for the spatial and temporal organization of mitosis. They function in spindle assembly, chromosome segregation and cleavage plane specification. To fulfill their task, however, they are dependent on the properties of microtubules and motor proteins.

Mitotic spindle

The mitotic spindle is a bipolar, self-organizing, and highly dynamic structure responsible for chromosome segregation and cleavage plane specification during mitosis. It is built from microtubules and motor proteins. The mitotic spindle consists of two spindle poles, where the microtubules are focused into an aster with the minus ends of all microtubules located close to the center (figure 1.3). Three classes of microtubules build up the mitotic spindle. Astral microtubules radiate out from each spindle pole towards the cell cortex. Kinetochore microtubules connect spindle poles with the kinetochores of chromosomes. Polar microtubules overlap with each other and are crosslinked, mechanically connecting the two spindle poles.

Spindle positioning and elongation has been proposed to be controlled by the action of different motor proteins (figure 1.3). The minus-end directed motor dynein, linked to the actin cell cortex, could exert a “pulling” force on

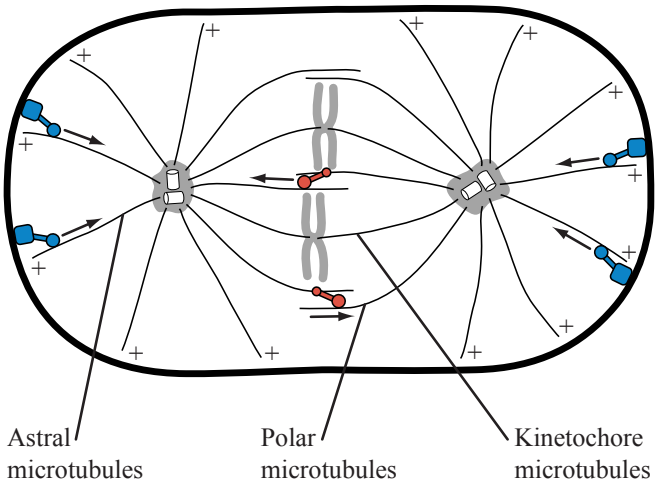

Fig. 1.3 The mitotic spindle is a bipolar structure. The two spindle poles are polarized, with the minus ends of microtubules focused together. Three classes of microtubules comprise the mitotic spindle: astral microtubules, kinetochore microtubules, and polar microtubules. Blue, a proposed localization and function of dynein. Red, a proposed localization and function of an asymmetric crosslinker (a motor protein with microtubules for cargo).

a spindle pole by walking along an astral microtubule emanating from the spindle pole [12, 4, 1]. Crosslinking plus end directed motor proteins could "push" spindle poles apart during anaphase [4, 1].

The position of the mitotic spindle at the time of late anaphase defines the plane of cleavage [13, 14, 15, 16, 17, 12, 18], as the spindle is symmetrically bisected by the cleavage furrow (an exception to this rule is reported in [19]). This is of particular interest for asymmetric cell divisions.

1.1.2 Properties of microtubules and motor proteins

This section presents some of the properties of microtubules and motors essential to the understanding of the mechanics of processes involved in cell division.

Microtubule polymerization forces and aster positioning

Microtubules polymerize and depolymerize by the addition and loss of tubulin dimers from their ends [20]. Microtubules switch between the polymerizing and the depolymerizing state, a behavior referred to as *dynamic instability* [21]. The transition from a polymerizing to a depolymerizing microtubule

has been termed a *catastrophe*, whereas the reverse transition is called a *rescue*. A solution of purified tubulin is already capable of exhibiting dynamic instability [22, 23], and catastrophes and rescue transitions have been observed in a physiological cytoplasmic environment [24, 25]. However, these occur at different rates when compared to purified tubulin in vitro.

There are specific proteins that modify the dynamic properties of microtubules. *Microtubule-associated proteins* (MAPs) are capable of increasing polymerization rates, whereas destabilizing proteins such as XKCM1 (a member of the Kin1 subfamily of kinesins in *Xenopus*) [26, 27] increase catastrophe rates. In *Xenopus*, the dominant stabilizing MAP appears to be XMAP215 [28, 29]. By combining XKCM1 and XMAP215 with purified tubulin in vitro it is possible to reconstitute physiological levels for essential features of microtubule dynamics [30]. A general increase of polymerization rates results in large microtubule asters, whereas increasing the catastrophe rate leads to small asters with short microtubules. Therefore, a cell can control the average length of microtubules in an aster by varying the levels of regulatory proteins such as XKCM1 and XMAP215 [28, 31, 26, 27, 29].

Dynamic instability is a nonequilibrium process and therefore requires an energy source. Both α- and β-tubulin bind GTP. The GTP bound to β-tubulin can be hydrolyzed to GDP and thereby provide the required energy [20]. By the use of non-hydrolyzable GTP variants, the fraction of the total free energy released by GTP hydrolysis involved in polymerization and depolymerization was estimated to be $\Delta G_{poly} \sim -3\,\mathrm{kcal\ mol^{-1}}$ [20] and $\Delta G_{depol} \sim -5\,\mathrm{kcal\ mol^{-1}}$ [32], respectively. The maximum pushing force that a polymerizing microtubule can generate and the maximum pulling force that a depolymerizing microtubule can exert is estimated [33, 34] according to $F = \frac{\Delta G}{d}$ (referred to as the *thermodynamic force* [35]). d is the change of length of a microtubule upon addition of one tubulin dimer and equal to 0.61 nm for a 13-protofilament microtubule (the length of a single tubulin dimer is about 8 nm).

According to this estimate, the thermodynamic force of polymerization is 35 pN per microtubule, for depolymerization it is -60 pN per microtubule [20]. It should be noted, however, that several of the parameters required for the determination of the in vivo values of ΔG_{poly} and ΔG_{depol} were estimated. In comparison, an estimation in [35] provides maximal polymerization and depolymerization forces of 40 pN and -15 pN, respectively. In any way, these forces are considerably larger than those generated by motor proteins [35], providing that polymerizing and depolymerizing microtubules realize a high efficiency in turning chemical energy to work. It is possible to extend the discussion to derive a general force-velocity relationship for growing microtubules [36], describing the rate of microtubule elongation as a function of

the force exerted while growing.

In conclusion, the thermodynamic cycle of polymerization and depolymerization of tubulin provides estimates for the forces that can be generated in the process.

To understand the contribution of microtubules to the mechanics of cell division it is necessary to determine their material properties. Using optical tweezers to capture a microtubule and to move it through the viscous buffer medium, the flexual rigidity of single microtubules from pure tubulin was determined to be $(4.7 \pm 0.4) \times 10^{-24}\,\mathrm{Nm}^2$ [37]. Addition of a microtubule stabilizing factor (taxol) reduces the flexual rigidity, whereas addition of MAPs results in an increase, leading to stiffer microtubules [37, 38].

If microtubules are grown in a confined space, they will bend as they continue to polymerize. By utilizing the measured values for the flexual rigidity one can experimentally determine the force-velocity relationship for a microtubule polymerizing at both ends by having it bend as it continues to grow [39]. A microtubule will grow at a rate of about $0.5\,{}^{\mu\mathrm{m}}/_{\mathrm{min}}$ if it exerts a force of 1.7 pN [39]. The rate drops as the force is increased. The highest force measured was a value of about 4 pN at a growing speed close to zero [39]. In comparison, the thermodynamic force of a microtubule polymerizing at the plus end is an order of magnitude higher (the exact factor depending on the speed of polymerization). From this it is concluded that the efficiency of turning chemical energy into mechanical work is in the range of 10%. It should be noted that the stall force for growing microtubules has not been precisely measured [39, 40].

In conclusion, a number of biophysical parameters of microtubules have been experimentally determined by the use of different biological and biophysical techniques. Care has to be taken, however, when applying these data to different in vivo systems, as distinct proteins might interact with microtubules and change the material properties as well as dynamic parameters, as shown for example for the flexual rigidity of microtubules [37].

Properties of microtubules have been utilized to generate theoretical models predicting different features of force generation as well as steady state parameters of aster assembly [36, 40, 41]. Furthermore, it is possible to develop a model which predicts the positioning behavior of microtubule asters in a confined area [42]. This follows from experiments suggesting that it is possible for a MTOC to find and maintain its correct position with the help of either motor forces, forces generated by microtubule polymerization, or a combination of both [43, 44, 45]. To analyze the positioning behavior resulting from microtubule polymerization forces, a MTOC was placed in a superficial confined area and allowed to develop into a microtubule aster [46]. However, a thorough comparison between the theoretical model and in vitro

aster positioning has not yet been performed, although some of the aspects are reproduced in the model [42].

In conclusion, the experimental accessibility to a number of the dynamic parameters of microtubules as well as the material properties has lead to the generation of theoretical models describing the behavior of a population of microtubules growing from a MTOC. It has been demonstrated that microtubule polymerization forces clearly take part in the process of aster positioning. However, their relative contribution for the in vivo situation, where motor proteins also act, remains to be determined.

Forces generated by conventional kinesin

Similar to determining the biophysical properties of microtubules, it is necessary to establish the dynamic parameters of the motor proteins involved in spindle assembly, positioning and elongation.

Single molecule techniques have demonstrated that conventional kinesin is processive, it can walk along a microtubule for hundreds of nanometers, even when it is put under load [47]. The motion is stepwise with an amplitude of about 8 nm, corresponding to the length of a single tubulin dimer [35]. Kinesins utilize the energy derived from ATP hydrolysis to perform work.

The maximum force that conventional kinesin can work against is in the range of 6 pN. Stall forces in the range of 4 to 8 pN have been measured by the use of optical tweezers [48, 49, 47, 50], glass fiber bending [51], microtubule bending [52] and using hydrodynamic forces [53]. Similar to growing microtubules, kinesins display a force-velocity relationship, which is linear for forces below about 3 pN [35]. Conventional kinesin walks at a speed of about 800 $^{\mathrm{nm}}/_{\mathrm{s}}$ if no load is present [51]. In addition, kinesins from different species have been studied by related approaches [54].

The stall force can be compared to the thermodynamic force of kinesin (calculated form the free energy derived from the hydrolysis of ATP). This comparison provides an efficiency of about 50% of turning chemical energy to mechanical work [35].

Table 1.1 displays a summary of experimental data for dynamic parameters of microtubules polymerizing from pure tubulin in vitro and conventional kinesin walking along a microtubule in vitro. It should be noted that kinesin speed is much higher than the speed of microtubule polymerization. Consequently the power produced by kinesin (the mechanical work per unit of time) is three orders of magnitude higher.

The dynamic parameters of kinesin together with the material constants of microtubules as well as the corresponding dynamic parameters have been used to study the self-assembly of microtubules and crosslinking multi-headed

Parameter	Description	Microtubule	Kinesin
F_{max}	Force at $v = 0$	4 pN [a]	6 pN [b]
v_{max}	Velocity at $F = 0$	1 μm/min [a]	0.8 μm/s [c]
P	Power at intermediate speeds	4×10^{-10} pW	8×10^{-7} pW

Table 1.1 Summary of experimental data for a single microtubule polymerizing in pure tubulin and a conventional kinesin walking along a microtubule. Both processes play an important role in determining the mechanical and the dynamic properties of the mitotic spindle. F_{max} corresponds to the stall force of kinesin walking along a microtubule, or the highest measured force exerted by a polymerizing microtubule. v_{max} is either the velocity of kinesin or the speed of microtubule growth at zero load. Values indicate the order of magnitude only. [a] [39], [b] [48],[c] [51].

kinesin molecules [7, 8]. Different steady-state solutions as a function of the concentration of the various molecules are predicted in a model and experimentally verified. The steady-state assemblies correspond to polarized asters or vortex-like structures, and there can be more than one set of conditions resulting in similar solutions. These studies suggest that further parameters, such as the rate of kinesin detachment at the end of a microtubule, need to be taken into account to make precise predictions [8].

In conclusion, the biophysical properties of kinesin have been extensively studied. However, no in vitro experiments have been performed to study aster positioning both with polymerization forces and forces exerted by motor proteins present, as is the case for a dividing cell. Furthermore, the in vivo analysis is obstructed by the fact that not all of the proteins involved in spindle positioning are known, although there are systems where a complete list is within reach [55]. Of the known proteins that participate, a detailed analysis of the dynamic parameters and the material properties have only been performed for kinesin and microtubules. For other proteins these parameters have to be estimated. In particular, dynein has not been studied as extensively as kinesin [35]. For these reasons it is not possible at this date to generate a "bottom-up" model of spindle positioning in a living cell, which is based on the biophysical properties of the molecular components.

1.1.3 Mechanisms of spindle positioning

The mitotic spindle is built of microtubules and motor proteins. One of its functions is to define the plane of cleavage, as the spindle is symmetrically bisected by the cleavage furrow at the end of anaphase in most of the cases. In this section the mechanisms contributing to the correct placement of the

spindle, both for symmetric and asymmetric cell divisions, are discussed.

It has been mentioned before that microtubule asters are capable of positioning themselves at a center of an artificial geometry through the action of microtubule polymerization forces. Similarly, MTOCs in living cells can find the center of a cell, responding to changes in cell shape. Experiments performed in fish pigment cells demonstrate that microtubules rearrange and form a new MTOC in a fragment of the cell which has been cut off with a needle. This MTOC lacks centrosomes and is capable of positioning itself at the center of the cell fragment [56, 57]. Furthermore, MTOCs assume an eccentric position towards the leading edge of a migrating cell in some cell types, although an eccentric position does not initiate migration [58]. In *Schizosaccharomyces cerevisiae*, the three to four astral microtubules emanating from the spindle poles interact with the cell cortex, thereby orienting the spindle properly in the bud neck [59]. In conclusion, positioning of MTOCs is likely to depend both on polymerization forces generated by the highly dynamic microtubule aster and on forces generated at the sites of interaction between astral microtubules and the cell cortex.

Cortical force generation in spindle positioning

We distinguish between *global* force generation, where forces are a product of non-localized interactions all over the cell cortex, and *confined* force generation, where the interactions and the resulting forces are limited to a cortical domain. The latter is realized in many systems with predetermined polarity, where spindle positioning is asymmetric and follows specific polarity cues [60].

The microtubule motor dynein and its regulator dynactin participate in cortical force generation [59]. Dynein and dynactin are thought to attach astral microtubule to the cortex, where dynein exerts a pulling force on the corresponding spindle pole by walking towards the minus end of the microtubule [12, 61, 62] (see figure 1.3). Dynein and dynactin contribute to spindle positioning in *S. cerevisiae* [59], *Dictyostelium discoideum* [63], *Caenorhabditis elegans* [64], *Drosophila melanogaster* [65], and mammalian cells [60].

Dynein and dynactin are considered to take part in a more global mechanism of force generation in some situations, as dynein localizes to the cytoplasm and the mitotic spindle and not to a specific cortical region in the one cell stage *C. elegans* embryo [64]. Similarly, dynein localizes to spindle poles and astral microtubules at metaphase in rat epithelial cells [62, 60]. In other examples, such as the P1 cell of the two cell stage *C. elegans* embryo, dynein and dynactin localize to a cortical domain acting in a more confined manner [66, 67, 12].

A different mechanism of force generation functions through the microtubule-associated protein Kar9p and the microtubule-binding protein Bim1p in the asymmetric division of *S. cerevisiae* [68, 69, 59]. This is also referred to as the Kip3p pathway, for the initial member kinesin Kip3p [59]. Cells lacking either protein fail to initially align the metaphase spindle towards the bud. It is thought that Bim1p and Kar9p promote the depolymerization of microtubules while still keeping the microtubule tethered to the cortex, thereby generating a pulling force on the microtubule [59]. Kar9p localizes to a dot on the bud cortex in the absence of microtubules [70], which probably corresponds to the site of microtubule attachment. Consequently, Kar9p and Bim1p are considered to be part of a more confined mechanism of force generation.

As a further possibility, the mitotic spindle can be simply mechanically connected to the cortex, as it might be the case in *Drosophila* embryos [71]. This is referred to as a *passive* attachment or a *rigid body constraint*.

In conclusion, there are different means of cortical force generation which can act in a more global or in a more confined manner. All these mechanisms take part in spindle positioning, and their relative contributions have to be determined for each case.

Molecular basis of the cortical interactions

In budding yeast, many proteins have been identified that are involved in the interactions between microtubules and the cortex. To summarize the events for the dividing yeast cell, the Kip3p pathway is required for the initial movement of the nucleus towards the bud, the alignment of the spindle with the mother-bud axis, and the movement of the spindle into the bud neck [72, 73]. The molecules which serve as cortical anchor molecules for these processes are [73]: Kar9p [70], Bni1p (a yeast formin [74]), Bud6p (an actin-interacting protein [75]), Myo2p (a type V myosin [76]), and actin itself. Several interactions among these molecules have been reported [59]. Importantly, Kar9p interacts with Bim1p, which is localized to the plus end of microtubules [59]. Kar9p itself localizes to the bud cortex, this localization is dependent on Myo2p [76]. An interesting hypothesis is that a Kar9p-Bim1p-Myo2p complex pulls microtubules along actin cables, thereby orienting the spindle properly [59]. On the other hand, Myo2p could serve to rapidly transport Kar9p to the bud cortex, where it can locally interact with Bim1p attached to the plus ends of the astral microtubules to generate force.

The movement of the spindle into the bud neck as well as the oscillations within the neck are dependent on dynein and dynactin [73]. For these proteins the molecular basis of attachment to the cortex is unknown. Inter-

estingly, the dynein-dependent oscillations do not require filamentous actin [73], which raises the question as to how dynein and dynactin are anchored.

In mammalian cells as well as *Drosophila*, microtubules are possibly attached to the cortex by the action of adenomatous polyposis coli protein (APC) and β-catenin in a complex with dynein [77]. β-catenin is a member of the wingless pathway [78] and acts as a link between cadherins and α-catenin, which is indirectly linked to the actin cytoskeleton. As APC binds to β-catenin, this is thought to be a way of attaching APC to the cortex [77]. APC, however, binds to microtubules, both directly and indirectly through EB1, the mammalian homologue of Bim1p in yeast [79]. Furthermore, cytoplasmic dynein has been shown to associate with β-catenin, allowing for another possibility of microtubule capture and attachment [80]. APC2 in *Drosophila* [71] has been demonstrated to play a role in attaching microtubules to the cortex in a fashion similar to APC. In this case, however, the link between APC2 and microtubules has not yet been identified, and it is not clear whether this is simply an attaching or a force generating interaction.

In conclusion, many proteins serve to establish and regulate the connections between microtubules and the cortex. There are similarities among different species, suggesting that basic principles of attachment and regulation are conserved [59].

Mechanisms allowing for MTOC and spindle centering

How do the different mechanisms of force generation manage to position the mitotic spindle properly? For eccentric spindle positions, confined force generation provides an obvious mechanism. This is realized in the P1 cell of the two cell stage embryo [67], where a cortical site containing dynein and dynactin [66] is thought to exert a pull onto one of the spindle poles and thereby rotates the mitotic spindle onto the proper axis.

Microtubule polymerization forces, as an example for global force generation, provide a way of positioning the mitotic spindle in the center of the cell [81, 46]. There are different possibilities in the case of global cortical pulling forces generated by, for example, dynein and dynactin (figure 1.4). Although simulations have been performed [82, 83, 84], no thorough theoretical model has been developed so far. Length dependent forces [85] have been implied to function in spindle positioning [60, 84]. If a microtubule grows out from a MTOC and is aligned along the cortex, the probability of a cortically anchored motor protein to attach increases linearly with the length of the microtubule. For flat cells this is an attractive mechanism, as astral microtubules could contact the cortex along their whole length. In egg-shaped embryonic cells with mostly straight microtubules the contributions

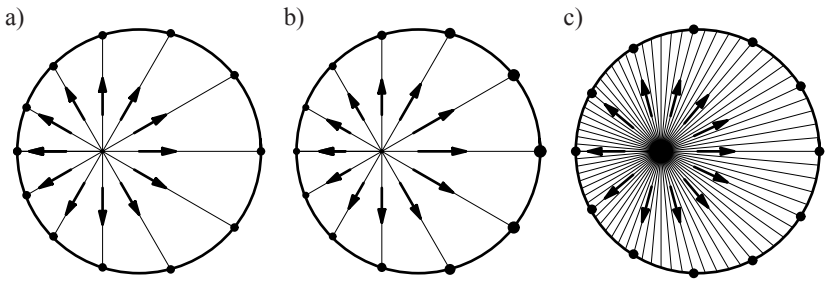

Fig. 1.4 Possible mechanisms of aster positioning by global cortical force generation. The connections between microtubules and the cortex that are indicated by a disc exert a pulling force on the aster. The magnitude of the force is proportional to the length of arrows. a) Forces are not dependent on the length of a microtubule. Centering is not possible. b) Length-dependent forces. Any displacement away from the center results in a force pointing towards the center. c) Anchor points are sparse. Forces are independent of microtubule length, but the connections where forces are generated at the cortex are limited. Furthermore, if these connections are evenly distributed along the cortex, a displacement of the spindle pole away from the center results in a force pointing towards the center.

of such a mechanism are questionable. Length dependent forces have not been proposed to be involved in spindle pole positioning in yeast. In these systems there is another possibility which has not yet been considered: If the connections to which microtubules attach and where forces are generated are limited and evenly distributed around the cortex, a displacement of an aster away from the center will generate a force pointing back towards the center (figure 1.4 c). It should be noted, however, that positioning is most likely the result of a combination of the different mechanisms presented (polymerization forces, passive attachment, active pulling by anchored motor proteins). Furthermore, the dynamics of cortical attachment play an important role.

In conclusion, confined cortical force generation through dynein/dynactin and Bim1/Kar9 has been implied to function in asymmetric cell division. Global cortical force generation through dynein/dynactin is thought to play a role in centering the mitotic spindle in the middle of a cell, possibly through length-dependent forces or through limited anchor points.

Spindle positioning and spindle elongation

The different mechanisms of global or confined force generation result in a net force acting on each spindle pole, which is the sum of all the participating forces (the vector sum of all arrows in figure 1.4 b, for example). Several

experiments have been performed to determine the net force acting on each spindle pole during anaphase in symmetrically dividing cells [86, 87, 88, 89]. These forces are involved in spindle positioning and elongation.

To review the results and conclusions described in the literature, a simplified one-dimensional model (along the axis of cell division) is established following the concepts of classical mechanics [90, 91].

Two particles, x_1 and x_2, describe the position of two spindle poles. The forces acting on the two spindle poles are divided into *internal* forces F^{int}, exerted by one particle on the other, and *external* forces F^{ext}. The cortical forces described in the previous section fall in the category of external forces.

The general equation of motion, containing a term describing frictional forces proportional to the speed of a spindle pole $\dot{x}_i$, is written as:

$$\frac{d^2}{dt^2}\sum_i m_i x_i = \sum_i F_i^{ext} + \sum_{i,j \;\; i\neq j} F_{i,j}^{int} - \sum_i \beta_i \dot{x}_i, \tag{1.1}$$

where m_i denotes the mass of each particle ($m_1 = m_2$), and β_i is the friction coefficient. As the distance between the two spindle poles is constant (they are mechanically connected) the following constraint is added:

$$(x_1 - x_2)^2 - l^2 = 0, \tag{1.2}$$

where l describes the length of the spindle. The process of spindle elongation is not considered at this point. Any constraint of the form $(x_i - x_j)^2 - l_{i,j}^2 = 0$ is referred to as a *rigid body constraint*. Rigid body constraints lead to the generation of internal forces, keeping the two particles at a constant distance to each other. This follows from Newtons third law, the equality of action and reaction.

Two more particles x_3 and x_4 are added, they represent the cell cortex at either end of the cell. These are fixed in space ($m_3 = m_4 = \infty$).

To allow the two spindle poles to position themselves properly, any combination of the following mechanisms can act in positioning the spindle poles x_1 and x_2:

1. External forces F^{ext} can act on spindle poles.

2. Additional internal forces F^{int}, not resulting from rigid body constraints, can act on each spindle pole.

3. Further rigid body constraints can keep the distance of either spindle pole to the cortex (x_3 or x_4) constant.

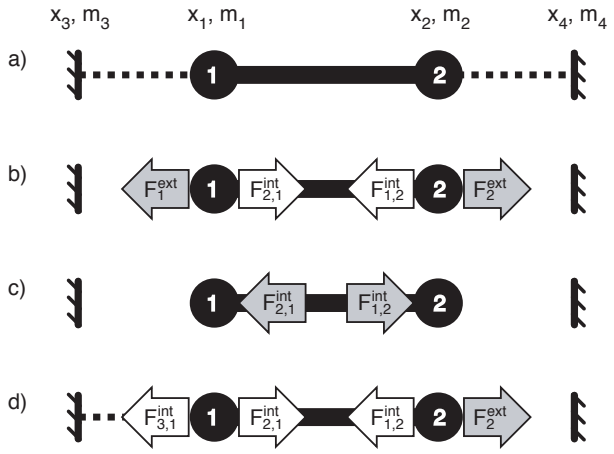

Fig. 1.5 Possible forces acting on two spindle poles x_1 and x_2. Forces acting on the cortical elements x_3 and x_4 are not drawn. Dashed and solid lines represent rigid body constraints. Shaded arrows display *active forces*, not resulting from rigid body constraints, white arrows denote forces resulting from rigid body constraints. Removing the spindle midzone (solid line) corresponds to setting $F_{1,2}^{int} = F_{2,1}^{int} = 0$. Afterwards, only the forces that do not result from rigid body constraints will cause the displacement of a spindle pole.

Both an external force and an additional internal force, not resulting from rigid body constraints, is referred to as an *active force*. Figure 1.5 displays various possible combinations of active forces and additional constraints. Once all of these are defined, the general equation of motion can be solved (equation 1.1).

There is a possibility to test for the presence of active forces. Removing the spindle midzone (this corresponds to ignoring equation 1.2) results in setting the internal forces $F_{1,2}^{int}$ and $F_{2,1}^{int}$ to zero. Active forces will then begin to accelerate a spindle pole. Consequently, if the spindle poles start to move apart after the removal of the spindle midzone, there are external forces pulling on them. This implies that the spindle was under mechanical tension prior to the removal.

In symmetrically dividing mitotic diatoms, for example, spindle poles do not move apart following spindle severing with a UV laser [87]. The authors conclude from these results that there are no external forces present, and that spindle elongation must be a consequence of internal forces only. This corresponds to scenario c in figure 1.5. However, severing the mitotic spindle in symmetrically dividing *Fusarium* [86] and PtK2 cells [88] leads to an increase in pole-to-pole distance for both cases. The authors conclude that external forces are contributing to spindle elongation. This corresponds

to scenario b in figure 1.5.

No experiments have been performed to study the forces involved in asymmetric cell divisions. Scenario d in figure 1.5 shows a hypothetical mechanism. An additional constraint keeps the distance between the spindle pole x_1 and the cortex x_3 constant. There is an external force acting on x_2, which might function in elongating the spindle as it relaxes to the tension. If this happens, the spindle will assume an eccentric position due to the new constraint. If the spindle midzone constraint is removed, however, only spindle pole x_2 will accelerate, as this is the only spindle pole with an active force pulling. In chapter 2, active forces and additional rigid body constraints acting in the asymmetrically dividing one cell stage *C. elegans* embryo are determined by the method of rigid body constraint removal.

1.2 Asymmetric cell division in *Caenorhabditis elegans*

Asymmetric cell divisions play a critical role for the generation of diverse cell types during development and differentiation in virtually all organisms [92, 93, 94]. Either daughter cells differing both in morphology and fate, or two morphologically identical cells with different fates are created. The asymmetric distribution of a specific factor, a *cell fate determinant*, leads to the generation of different daughter cells [95]. To ensure segregation of a cell fate determinant to only one of the blastomeres, three fundamental steps have to be executed [12]: First, an initial asymmetric cue has to be set up. This is a symmetry breaking event, as an axis of division is specified and the two future daughter cells can be distinguished from this point on. Second, this asymmetric cue is utilized to distribute cell fate determinants to a specific cellular localization. This involves the translation of the asymmetric cue to an asymmetric distribution of *markers of polarity*, which control the events that follow. Third, the plane of cleavage has to be oriented and positioned in a way to ensure the proper segregation of cell fate determinants to daughter cells. In some cases this involves an eccentric position of the cleavage plane, leading to two morphologically different daughter cells of different size.

The mechanisms regulating these processes display extensive parallels among different species, for example *Drosophila* neuroblasts and the single cell stage *C. elegans* embryo [96, 97]. This section summarizes the events leading to the specification and generation of two different daughter cells following fertilization of the *C. elegans* oocyte.

Caenorhabditis elegans

C. elegans is a free-living, 1 mm long soil nematode found in many parts of the world [98]. It feeds on bacteria and reproduces with a life cycle of about 3 days, depending on the surrounding temperature and food availability. There are two sexes, hermaphrodites and males. These differ in adult morphology, the male is a bit thinner and shorter. Hermaphrodites produce both sperm and oocytes and can reproduce by self-fertilization. Males, which arise spontaneously with a low probability ($1/500$), fertilize hermaphrodites. A hermaphrodite that has not mated lays about 300 eggs. The young worms hatch and subsequently go through four stages of development (larval stages) before emerging into a mature adult. The adult is fertile for about 4 days and lives on for an additional 10-15 days.

C. elegans is a simple organism both with respect to its anatomy and its genome. The adult hermaphrodite consists of exactly 959 somatic nuclei, the adult male has 1031. One of the most prominent features is the invariant cell lineage, resulting in a cell lineage diagram listing which cells give rise to which daughters at what time [99]. The genome, which is completely sequenced [100], contains about 18000 predicted genes.

C. elegans is simple to maintain in the laboratory. It is grown on agarose plates or in liquid cultures, feeding on *Escherichia coli*. Individual animals can be easily observed under the microscope as the animal is transparent. Its small size allows a complete anatomical description even at the electron microscope level. Furthermore, the method of double stranded RNAi interference [101] enables the study of loss-of-function phenotypes within 24-36 hours.

Cell cycle stages

C. elegans embryogenesis commences when a mature oocyte, arrested in meiosis I, is fertilized by a sperm [102]. Prior to fertilization, the oocyte pronucleus moves away from the position where the spermatheca is contacted. The sperm enters at the contact site, the point of entry is thought to define the future posterior end of the embryo [103]. These events represent the first fundamental step, where symmetry is broken in the oocyte. After fertilization, meiosis is completed with the extrusion of two polar bodies, these are usually located at the anterior of the embryo. At this stage a rigid, ovoid-shaped chitin eggshell is created.

Following completion of meiosis the centrosomes, which are brought in by the sperm, organize large microtubule asters (see figure 1.6 for a depiction of the various cell cycle stages). The maternal pronucleus then migrates

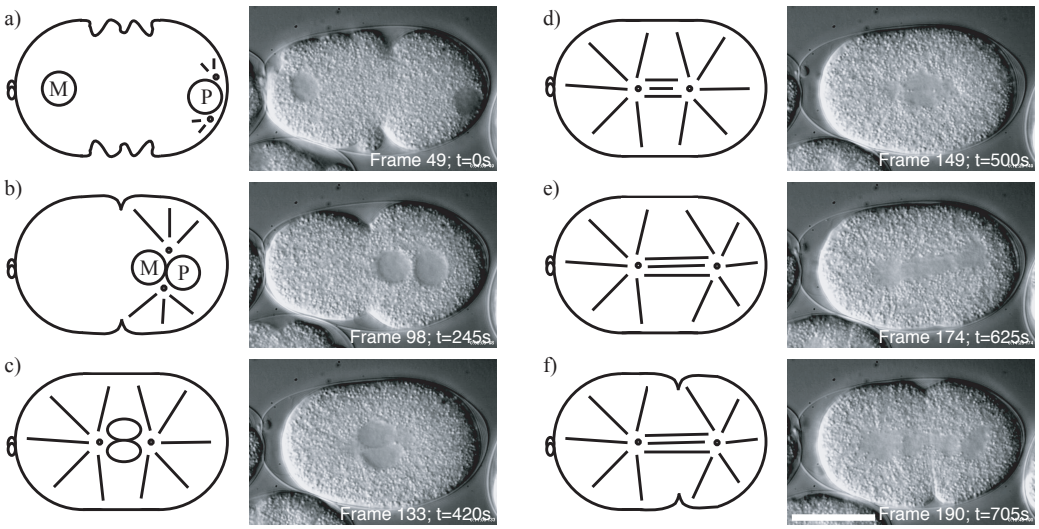

Fig. 1.6 Differential interference contrast (DIC) image timeseries of cell cycle stages in the one cell *C. elegans* embryo after fertilization. Anterior is on the left, posterior on the right. Areas void of yolk granules in the DIC images represent structures such as the pronuclei and the mitotic spindle. a) *Pronuclear migration*, the maternal pronucleus (M) migrates towards the paternal pronucleus (P), which has two centrosomes associated with it. Note the polar body at the anterior of the embryo. b) *Pronuclear meeting* close to where the paternal pronucleus was originally positioned. c) *Centering and rotation* of the pronuclear-centrosomal complex onto the anterior-posterior axis. d) *Setup of a mitotic spindle* shortly after pronuclear-envelope breakdown. e) Spindle elongation towards the posterior of the embryo during *anaphase*. f) *Cleavage* leading to a smaller daughter cell at the anterior and a larger daughter cell at the posterior of the embryo. Please refer to the movie "Ch1M01 WT DIC.mov" (corresponding frame numbers are indicated). Scale bar: 20 μm.

and meets the paternal pronucleus, concomitant with the generation of large cortical contractions (*pseudocleavage*). With the regression of the contractions cytoplasmic flows occur, towards the posterior inside the embryo and towards the anterior near the cortex. Notably, microtubules are required for some features of pronuclear migration, and microfilaments are necessary for the generation of cytoplasmic flows and the establishment of polarity [104, 105, 106]. Pronuclear meeting occurs towards the posterior of the embryo, followed by centration and rotation of the pronuclear-centrosomal complex onto the anterior-posterior (AP) axis. P granules, which play a role in determining germline fate, localize to the posterior end of the embryo [107] (corresponding to the second fundamental step). The mitotic spindle initially sets up in the center of the embryo. Following pronuclear envelope break-

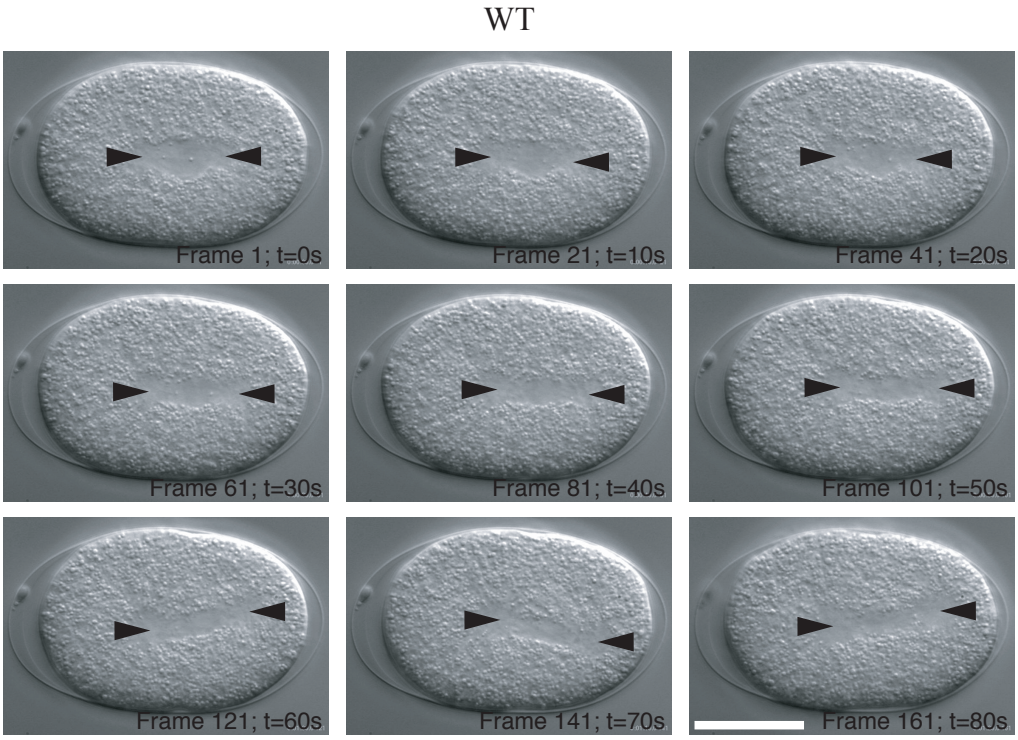

Fig. 1.7 DIC image series of a *C. elegans* embryo at the metaphase to anaphase transition. Anterior is on the left, posterior is on the right. Spindle poles are indicated (arrowheads). Note the polar body at the anterior of the embryo. Please refer to the movie "Ch1M02 WT Anaphase DIC.mov" (corresponding frame numbers are indicated). Scale bar: 20 μm.

down, the spindle elongates towards the posterior of the embryo, producing an eccentric position of the spindle apparatus at the end of anaphase. This process is accompanied by prominent transverse oscillations of the posterior spindle pole [15] at a frequency of about $^1/_{25}$ Hz. The anterior spindle pole remains in a relatively fixed position (see figures 1.7 and 1.8 for a detailed time-lapse series). The asymmetrically positioned spindle dictates the cleavage furrow towards the posterior end (corresponding to the third fundamental step), resulting in a larger blastomere at the anterior end and a smaller one at the posterior end (termed AB and P1, respectively). The spindles orient along different axis in these two daughter cells, and the cell-cycle times vary. Importantly, P granules segregate into the germline precursor cells P1, P2, P3 and P4 [107].

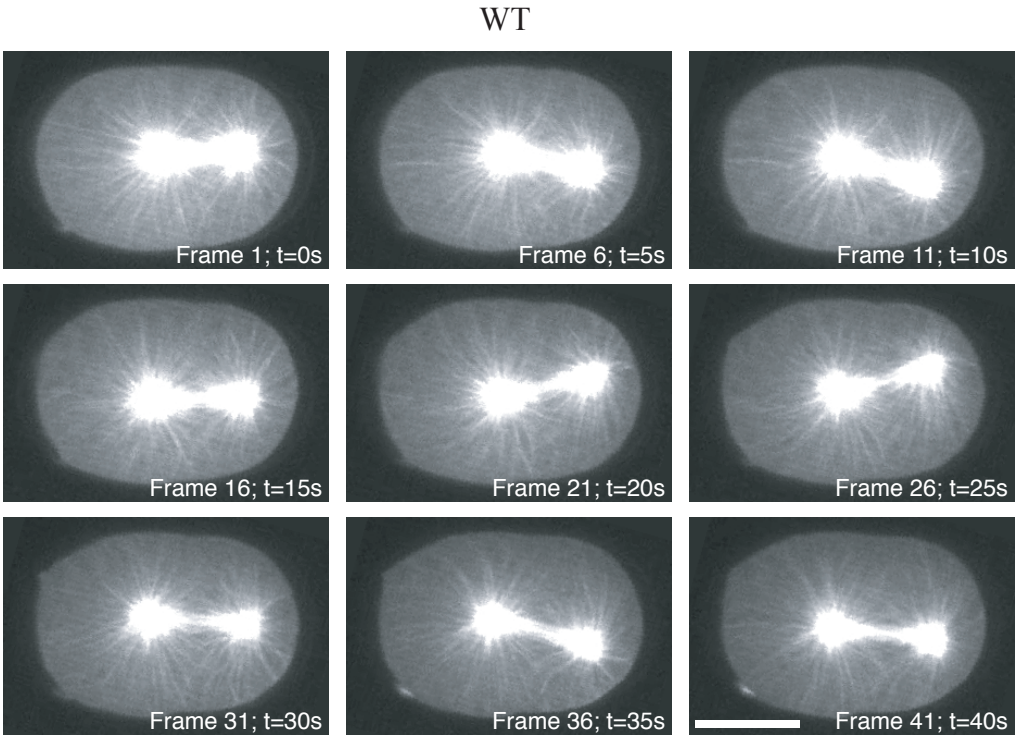

Fig. 1.8 Spinning disc confocal (SDC) image series of a GFP-tubulin *C. elegans* embryo during anaphase. Anterior is on the left, posterior is on the right. The image plane is not changed over the course of the recording. A water immersion lens with a numerical aperture of 1.2 was used for recording. Please refer to the movies "Ch1M03 WT Anaphase SDC.mov" and "Ch1M04 WT Anaphase SDC.mov". Scale bar: 20 μm.

Establishment and transduction of cell polarity

As previously mentioned, the sperm entry point defines the posterior end of the embryo. Oocytes fertilized by sperms that are lacking DNA still manage to establish polarity, suggesting that a centrosomal or a microtubule aster component might play a role in initial establishment of polarity [108]. Two studies suggest that a MTOC is necessary and sufficient for some aspects of AP polarity [109, 110]. However, this is in contradiction to results previously obtained by the depolymerization of microtubules with the drug nocodazole, suggesting that microtubules are not involved [111].

The initial asymmetric cue is translated into an asymmetric distribution of a group of proteins, termed the PAR-proteins (for partitioning-defective) [107]. PAR-1, a serine-threonine kinase, and PAR-2, a RING finger protein,

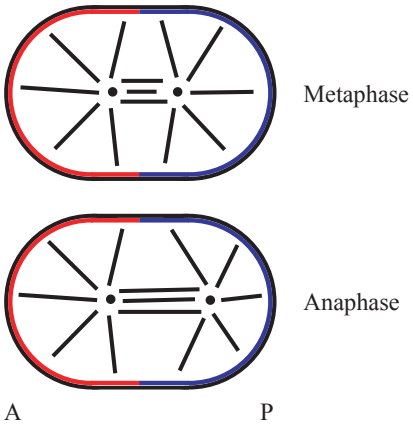

Fig. 1.9 Metaphase to anaphase transition. PAR-2 localization is indicated in blue, PAR-3 in red. Anterior (A) on the left, posterior (P) on the right. The anterior spindle pole remains in a relatively fixed position along the anterior-posterior axis, whereas the posterior spindle pole is displaced to the posterior while it oscillates transversely.

localize to the posterior cortex [112, 113, 114]. PAR-3, PAR-6 and PKC-3, an atypical protein kinase C, localize to the anterior cortex [115, 116, 117]. Both PAR-3 and PAR-6 contain PDZ domains, which are important for protein-protein interactions. Mutation in either of these genes disrupt various aspects of the observed asymmetries, such as protein localizations, spindle positioning, P granule localization and the fates of the AB and P1 cells [102, 118]. In conclusion, the PAR proteins function in transmitting the initial polarity cue to downstream events such as spindle positioning and cell fate determination.

As an example, PAR-3, which is localized to the anterior cortex in the wild-type embryo [115] (figure 1.9), is found both at the anterior and posterior cortex in a *par-2* mutant embryo. This leads to a cortex with anterior character throughout [107, 115, 119]. Conversely, PAR-2, restricted to the posterior cortex in the wild-type (figure 1.9), fills the entire cortex in a *par-3* mutant embryo, which subsequently has posterior character throughout [114, 119]. In both of these cases the spindle stays symmetrically positioned throughout anaphase, as polarity is not properly established [120].

Interestingly, a cortex of posterior character leads to the generation of transverse spindle pole oscillations, as both spindle poles in the *par-3* mutant embryo undergo transverse oscillations prior to the end of anaphase. The spindle, however, stays symmetrically positioned [107]. In contrast, in a *par-2* mutant embryo neither of the spindle poles oscillate. Similar oscilla-

tions have been reported for other asymmetrically dividing cells, for example budding yeast, where the oscillations within the bud neck are dependent on dynein [73]. This raises the question whether the generation of transverse oscillation and the asymmetric positioning of the mitotic spindle are related events. Interestingly, the localization of PAR-2 and PAR-3 divide the embryo equally [107] (figure 1.9). Therefore, polarity could possibly modify force-generating interactions between microtubules and the cortex in a rather global way (half of the surface area of the embryo cortex) to dictate the spindle to an eccentric position. The transverse oscillations may play a key role in understanding this process.

In transducing overall cell polarity to asymmetric spindle positioning, heterotrimeric G proteins are of importance [102]. Both GPB-1, the Gβ-subunit of a heterotrimeric G protein, and GOA-1 and GPA-16, two Gα-subunits, are required for the orientation of the one cell stage division axis [121, 122]. GOA-1 and GPA-16 function redundantly; the removal of both of these proteins by RNAi (Gα (RNAi)) leads to a symmetric cleavage without transverse spindle poles oscillations, similar to the *par-2* mutant phenotype. Interestingly, however, polarity is properly established as markers of polarity are correctly localized in Gα (RNAi) embryos [122], in contrast to the *par-2* mutant embryo. This suggests that heterotrimeric G proteins act downstream of polarity as to position the spindle correctly. Furthermore, the inhibition of both *ags-3.2* and *ags-3.3* by RNAi [55] (*ags-3* (RNAi)), which are receptor independent activators of G protein signalling homologous to mammalian Ags-3, results in a phenotype identical to removing both Gα proteins by RNAi. *Ags-3.2* and *ags-3.3* are 98% identical at a sequence level and thus indistinguishable by RNAi. Markers of polarity are properly localized in *ags-3* (RNAi) embryos (Kelly Colombo, personal communication). Consequently, the receptor independent activation of Gα-subunits is required for polarity-controlled positioning of the mitotic spindle in *C. elegans*.

In conclusion, the proteins involved in establishing polarity and transducing polarity to downstream processes have been studied in great detail. However, little is known about the mechanical principles underlying the asymmetric positioning of the mitotic spindle in the one cell stage *C. elegans* embryo. It is unknown whether global or confined forces are acting. The role of transverse oscillations is obscure. Do heterotrimeric G proteins function in cortical force generation, or do they specifically transduce cell polarity? One of the most intriguing questions is: What is changed at the anterior or at the posterior cortex as to cause the spindle to assume an eccentric position?

1.3 Biophysical techniques

The experimental accessibility of dynamic parameters and material constants through the controlled application of forces is a result of the development of different biophysical techniques. It is distinguished between *contact-free* force transduction through *electromagnetic fields*, force transduction through *elastic deformation*, and *hydrodynamic forces*.

Force transduction through electromagnetic fields

Magnetic bead microrheometer (magnetic tweezers) [123, 124, 125]) use magnetic beads a few μm in diameter for probes. A inhomogeneous magnetic field is generated by a magnet with a soft iron core extending into the sample chamber [123]. This extension is typically placed $10 - 100\,\mu$m away from the magnetic bead. The forces that are generated depend on the type of the bead, the size of the bead, and the gradient of the magnetic field. For paramagnetic beads with a diameter of $4.5\,\mu$m forces as large as 10 nN can be generated [123].

Single-beam gradient-force optical trap (optical tweezers) [126, 127, 128, 129] utilize a dielectric particle as a probe, which is typically either a polystyrene bead with a size in the order of one μm, a gold particle, or biological material. Due to the momentum transfer of photons onto the particle, these are trapped in water in the focus of a highly convergent laser beam. The three-dimensional trapping potential can be calculated in a vectorial approach using the theory of electromagnetism [130]. The forces that are generated depend of the dielectric properties of the particle, the particle size, the laser wavelength, and the laser power. Typically, $10 - 100$ pN are applicable for biological systems [131], where care needs to be taken that the sample temperature does not increase due to the absorption of light. As an application, forces that actively transport organelles in living amoeba have been measured by the use of optical tweezers [132]. The organelles themselves were trapped, force calibration was performed by comparing the transport in a living cell with the viscous drag in water following homogenization of the cells. Both magnetic tweezers and optical tweezers are referred to as contact-free methods, as no mechanical cantilever or force transducer is required.

Force transduction through elastic deformation

AFM-based cantilever methods [131, 133] use an atomic-force-microscopy (AFM) cantilever to apply forces, the deflection of the cantilever being proportional to the force exerted. The forces that can be applied solely depend

on the elastic properties of the cantilever. This technique is used to study adhesive forces and receptor-ligand interactions of single molecules [131, 133]. Measurements inside cells are problematic due to the mechanical cantilever, but have been performed using glass fiber cantilevers [52].

Biological force sensors [134], where for example a cell sized membrane is used as a force transducer. A microscopic bead attached to the membrane functions as a surface probe. The deflection of the bead is proportional to the force applied and inversely proportional to the membrane tension [134]. By varying the membrane tension through changes of the pressure inside, material properties over a force range of $0.01 - 1000\,\mathrm{pN}$ are accessible. This is also not a contact-free method, as the membrane needs to be anchored.

Hydrodynamic methods

Hydrodynamic forces can be applied by moving the sample relative to a viscous medium. It is possible to trap a microtubule with optical tweezers and move it through a viscous liquid, the elastic deformation of the microtubule being related to its flexual rigidity [37]. Hydrodynamic forces are often used as a mean of calibration, for example in the case of optical tweezers with microscopic beads as probes [135].

To conclude, these techniques provide different means of determining the material properties of a biological medium.

1.3.1 Material properties

All materials can be characterized by their relation to two idealized types of media: fully *viscous materials*, where all energy added is dissipated into heat, and fully *elastic materials*, where all energy added is stored in the material. Real media display both properties, a material is termed viscous if it mainly comprises properties of viscous material, and it is termed elastic if the elastic properties are dominant. For a sufficient description of most materials it is necessary to take both properties into account, these media are referred to as *viscoelastic*. Elastomers are an example, and biological material also falls in this category.

The deformation of isotropic continuous media in a linear approximation is described by a strain and a stress tensor [136, 137]. The strain tensor represents the deformation of the medium, whereas the stress tensor describes the mechanical tension required for the deformation. The basic equation of viscoelasticity relates strain and stress through the *relaxation modulus* G, following the principle that the stress at any given time t is derivable from all

earlier deformations (Boltzmann superposition principle). In one dimension, this relationship can be written as:

$$\sigma(t) = \int_{-\infty}^{t} G(t-t') \, \frac{\partial \epsilon(t')}{\partial t} \mathrm{d}t', \tag{1.3}$$

where $\sigma(t)$ refers to the mechanical stress and $\epsilon(t)$ to the mechanical strain. In a complementary form, the strain-response $\epsilon(t)$ for a given stress is:

$$\epsilon(t) = \int_{-\infty}^{t} J(t-t') \, \frac{\partial \sigma(t')}{\partial t} \mathrm{d}t', \tag{1.4}$$

where $J(t)$ is the *creep compliance*, functioning as a viscoelastic response-function.

For a time-independent $G(t) = const.$, equation 1.3 results in a Hookian behavior:

$$\sigma(t) = G \, \epsilon(t). \tag{1.5}$$

In this case, G is referred to as the *Young's modulus*.

If, however, $G(t)$ is set to $G(t) = \eta \, \delta(t)$, with $\delta(t)$ being Dirac's delta function, equation 1.3 results in Newtons law of viscous fluids for shear stress:

$$\sigma(t) = \eta \frac{\partial \epsilon(t)}{\partial t}, \tag{1.6}$$

with η referring to the dynamic viscosity of the fluid. In summary, equations 1.3 and 1.4 are capable of describing the viscoelastic properties of any continuous material in a linear approximation valid for small deflections. When applying these to biological media, boundary-effects have to be taken into account [123].

Magnetic tweezers have been used to study of the local viscoelastic properties of biological samples because of the large force range and the contact-free method of force transduction. Magnetic beads are incorporated into a living cell through endocytosis, and the creep compliance $J(t)$ of the cytoplasm is measured by recording the deflection and recovery of a ferromagnetic bead following sequences of rectangular force pulses [138]. By applying a mechanical equivalent circuit, the effective viscosity inside living J744 macrophages is determined to be $\eta = (210 \pm 143)\,\mathrm{Pa\ s}$ [138]. The shear elastic modulus (the equivalent of G in the case of shear stress) varies considerably within a population of cells and is in the range of $20 - 735\,\mathrm{Pa}$ [138]. Viscoelastic prop-

erties have also been determined for a whole population of *Dictyostelium discoideum* cells in a pellet through a macrorheological study, where phenotypic differences are detected between wild-type cells and cells lacking α-actinin, a crosslinker for filamentous actin [139].

In the case of *C. elegans*, the viscoelastic properties of the cytoplasm of the one cell stage embryo have not been determined. These studies are hindered by the presence of an eggshell, a rigid structure surrounding the embryo not allowing for the incorporation of artificial probes. Importantly, it is unknown whether viscoelastic properties are isotropic throughout the asymmetrically dividing *C. elegans* embryo, or whether cell polarity manifests itself in a variation of these parameters within the embryo. To provide an estimate, chapter 2.1 presents the determination of the diffusion coefficient of yolk granules following a mean-square-displacement analysis of yolk granule motion. Average diffusion coefficients are established separately for yolk granules located close to the anterior cortex and close to the posterior cortex. From the average diffusion coefficients D, the local cytoplasmic viscosity η can be estimated via the Einstein relation:

$$D = \frac{k_B T}{\gamma}, \tag{1.7}$$

where k_B is the Boltzmann constant, T the temperature in Kelvin, and γ the viscous drag of a yolk granule. As $\gamma = 6\pi\,\eta\,R_H$, the Einstein relation connects the diffusion coefficient D with the cytoplasmic viscosity η via the thermal energy and the hydrodynamic radius R_H of a granule.

1.3.2 Active forces and tensile stress

Motor proteins are capable of actively generating force, as mentioned before. These forces generate tensile stress within the structures where the forces are produced. Tensile stress can be detected in a non-destructive manner via the measurement of the mechanical strain (*elastic deformation*), or in a destructive manner through *rigid body constraint removal*.

Elastic deformation

By growing cells on micropatterned elastic substrates, the mechanical stress generated within the cells is determined through the detection of the deformation of the elastic substrate [140]. Similarly, the strain field resulting from forces applied on magnetic beads incorporated into the cytoplasm can be mapped by measuring the displacement of other beads nearby [123].

Rigid body constraint removal

The existence of tensile stress within the spindle structure can be tested by severing the spindle apart, as mentioned previously (section 1.1.3). If tensile stress is present, forces that were acting in a static manner prior to the removal now function in moving the two spindle poles apart from each other. This is a destructive method, as the connection between the two spindle poles (the rigid body constraint) is physically removed.

Experimental analysis of the mechanics of asymmetric spindle positioning in *C. elegans*

In chapter 2.2, the existence of active forces exerted on both spindle poles in the asymmetrically dividing one cell stage *C. elegans* embryo is tested via rigid body constraint removal. The mitotic spindle in a wild-type embryo is severed using a pulsed UV laser, and the positions of the anterior and the posterior spindle pole as a function of time after removal are recorded. If the pole-to-pole distance increases, tensile stress is present within the spindle at the time of spindle severing. The experiments are repeated at the time of metaphase to study cell-cycle dependent changes. As a control experiment, the spindle midzone is disrupted via genetic interference by the removal of a kinesin. Furthermore, to study whether the the net force acting on each spindle pole is under control of overall cell polarity, spindle severing experiments are performed in symmetrically dividing *par-2* and *par-3* mutant embryos.

To investigate the phenomenon of transverse oscillations of the posterior spindle pole and to distinguish between confined and global cortical force generation, chapter 2.3 presents *optically induced centrosome disintegration* (OICD) experiments. The pulsed UV laser is used to rapidly destroy a centrosome, thereby releasing the microtubules from their anchor point. The long-term consequences of removing a centrosome from a cell has been studied previously [141], here the focus is on the immediate effect in the first seconds following the disintegration. This method also falls into the category of rigid body constraint removal, as tensile stress within the microtubule aster is detected by breaking the minus-end connections of all microtubules simultaneously and recording the movements that follow. The displacement of microtubules following OICD is visualized either directly through fluorescence-tagging of tubulin by GFP [142] (green fluorescent protein) or indirectly trough the movement of yolk granules. OICD is performed both with the stationary anterior and the oscillatory posterior spindle pole. Furthermore, the function of AGS-3 (a receptor independent activator of G protein signalling, see section 1.2) in the context of cortical force generation is

studied by performing OICD experiments in embryos lacking AGS-3 protein.

Finally, a phenomenological model for asymmetric spindle positioning based on the experimental results is presented in chapter 3.

1.3.3 Experimental setup

Spindle severing experiments were performed using a commercially available ultraviolet laser microdissection apparatus (PALM Mikrolaser Technologie GmbH). A pulsed N_2 laser with a wavelength of $\lambda = 337\,\mathrm{nm}$ and an energy of about $300\,\mu\mathrm{J}$ per pulse is focused into the focal plane of an inverted microscope. Due to the inherently non-gaussian beam profile of N_2 lasers, diffraction-limited focussing is not possible without reducing the pulse energy. Using a 100x objective lens (Fluar 100x, numerical aperture (NA) 1.3, oil immersion, Zeiss), the destruction spot size in the focal plane of the PALM setup was determined to be about $1.5\,\mu\mathrm{m}$. A motorized microscope stage is used to laterally deflect the sample, thus enabling the manipulation at different points within the sample. The effect of focussing pulsed UV laser light into a biological sample is described in the literature [143], where it is proposed that the energy density within the focal spot is sufficient for the generation of a physical plasma, providing that all light is absorbed. This leads to the breaking of every chemical bond. As the total energy deposition is small (for ten pulses it is at most $3\,\mathrm{mJ}$) the heating of the sample due to photon absorption is negligible. It should be noted, however, that the presence of stray UV light leads to photodamage.

With the PALM setup it was not possible to reproducibly perform OICD experiments. For these reason a new setup was constructed, based on a third-harmonic Nd:YAG laser (PowerChip, JDS Uniphase) with a wavelength of $\lambda = 354\,\mathrm{nm}$ and a pulse energy of $10\,\mu\mathrm{J}$ per pulse. This laser has a gaussian beam profile, thus allowing for diffraction-limited focussing. In the optical setup, the laser light is attenuated by a polarizer, expanded to fill the aperture of the microscope (Axiovert 200M, Zeiss) and focused into the back focal plane of the fluorescence illumination path of the microscope (figure 1.10). A water-immersion lens (C-Apochromat 63x, NA 1.2, Zeiss) was used for all OICD experiments. Figure 1.10 c displays the size and isotropy of the destructive spot as a function of the number of pulses (recorded by focussing into a UV absorbing glass sample). The destruction spot size $10\,\mu\mathrm{m}$ inside the sample is estimated to be about $500\,\mathrm{nm}$, depending on the total energy depositioned.

The microscope is controlled by a computer using custom-made software (CCC, Nick Salmon and Alfons Riedinger, EMBL Heidelberg). The CCC software allows for the control of all parts of the microscope via a visual-

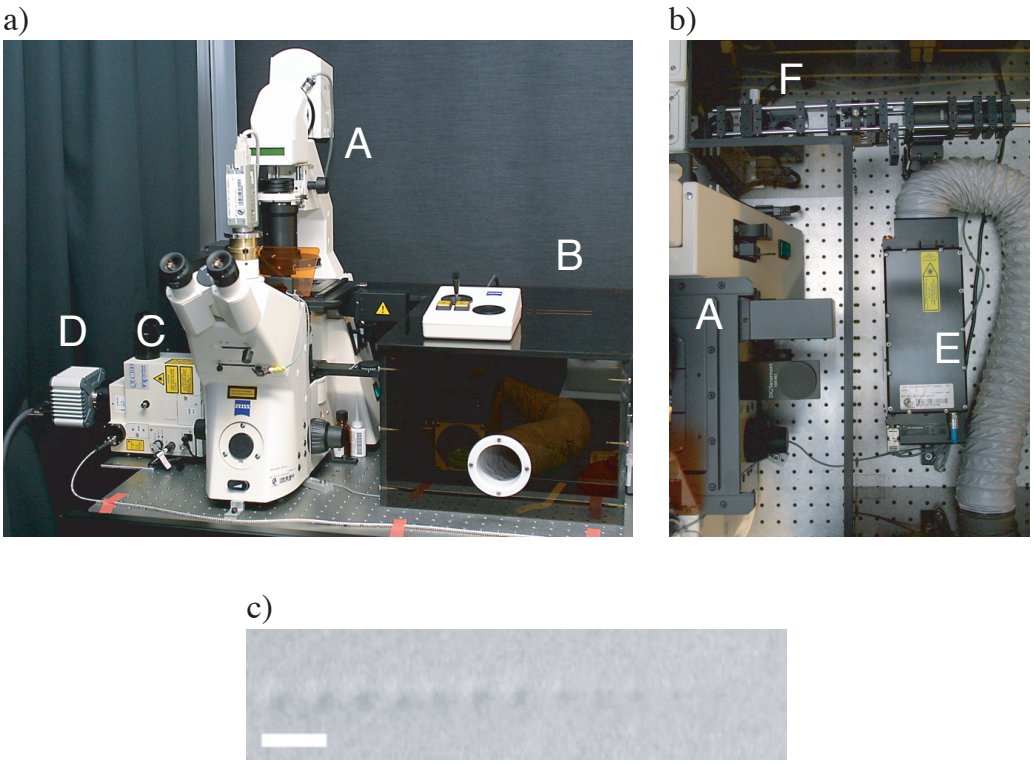

Fig. 1.10 The UV lasercutting setup. a) and b) Pictures of the setup. Axiovert 200M (Zeiss) (A), laser cutter housing (EMBL workshop) (B), Nipkow spinning disc confocal head (Yokogava) (C), ORCA ER camera (Hamamatsu) (D), pulsed UV laser (JDS Uniphase) (E) and optical elements (Linos) (F) are visible. c) Destruction spot size of the pulsed UV laser focused in glass with different amounts of energy depositioned. Image acquisition in DIC. Number of pulses decreases from 100 on the left to one on the right hand side. Scale bar: 2 μm.

basic interface (Microsoft), including the stage (Zeiss MCU 28), the camera (ORCA ER C4742-95, Hamamatsu), and the laser trigger generator (Georg Ritter, EMBL Heidelberg).

Reproducible OICD experiments are possible using the solid state laser, as the spot size is reduced in comparison to the PALM system. Furthermore, the CCC software is of importance because the visual-basic interface allows for the generation of patterns of illumination, thereby automating the disintegration of a whole centrosome. The user only needs to specify the location of the centrosome.

Image acquisition is performed in transmission using differential-interference-contrast (DIC) both for the spindle cut experiments and the OICD experiments. For the OICD experiments, fluorescent image series of

living manipulated embryos are recorded using a transgenic line expressing GFP-α-tubulin [142]. A cooled CCD camera (-20^{o}C, ORCA ER C4742-95, Hamamatsu) is utilized for the acquisition process. Furthermore, a Nipkow spinning disc confocal head (CSU10, Yokogawa) together with an argon-ion laser (50 mW laser power, 488 nm wavelength, Reliant Series, Laser Physics) for GFP excitation are used to reduce the thickness of the optical slice. This is necessary to acquire images with decent signal ratios of polymerized to unpolymerized tubulin at reasonable integration times (typically 800 ms), as the amount of cytoplasmic tubulin imaged per recording is reduced.

2 Experiments

This chapter is divided into three parts and presents the results of an analysis of yolk granule diffusion, spindle severing experiments, and optically induced centrosome disintegration experiments.

2.1 Analysis of yolk granule diffusion

To study the diffusion of yolk granules from DIC time lapse experiments, a mean square displacement analysis approach was employed.

2.1.1 Theoretical basis of the MSD analysis

The mean square displacement (MSD) as a function of the time interval Δt is an informative representation of an experimentally determined trajectory of a particle $\vec{r}(t) = \big(x(t), y(t)\big)$. This approach is used to study the diffusive properties of yolk granules in the one cell stage *C. elegans* embryo. For a particular granule, the x and y positions in the focal plane as a function of time (the trajectory) are determined using single particle tracking (SPT). Movement in the plane of focus is analyzed by computing the two-dimensional MSD as a function of the time interval Δt. Using this approach, a phenomenological diffusion coefficient can be calculated. This is a statistical method, as the diffusion of particles is a stochastic process.

The theoretical description presented here is based on [144, 145, 146]. For each trajectory of a particle the MSD as a function of Δt is computed by averaging over the whole trajectory [144]:

$$MSD(\Delta t) = \left\langle \big(\vec{r}(t + \Delta t) - \vec{r}(t)\big)^2 \right\rangle_t. \tag{2.1}$$

Experimentally it is only possible to determine the trajectory $\vec{r}(t)$ for times t that are a constant interval of δt apart. This is a consequence of the image acquisition process, as the camera records images at a rate of $\frac{1}{\delta t}$ images per second. If N denotes the total number of acquired images and δt

the constant time interval, the time interval Δt_n between n images is defined as:

$$\Delta t_n = n\ \delta t; \qquad n = 1, \ldots, N. \tag{2.2}$$

The mean square displacement then computes to [145, 146]:

$$\begin{aligned} MSD(\Delta t_n) &= MSD(n\,\delta t) \\ &= MSD_x(n\,\delta t) + MSD_y(n\,\delta t) \\ &= \frac{1}{N-n} \sum_{j=1}^{N-n} \Big(\big(x(j\,\delta t + n\,\delta t) - x(j\,\delta t)\big)^2 \\ &\qquad + \big(y(j\,\delta t + n\,\delta t) - y(j\,\delta t)\big)^2 \Big), \end{aligned} \tag{2.3}$$

where $\big(x(j\,\delta t{+}n\,\delta t), y(j\,\delta t{+}n\,\delta t)\big)$ describes the particle position following a time interval Δt_n after starting at position $\big(x(j\,\delta t), y(j\,\delta t)\big)$. Therefore the first value (n=1) in a $MSD(\Delta t)$ graph is the mean value of all displacements over the time interval δt. The second value (n=2) is the mean value of all displacements over $2\,\delta t$, and so on.

Equation 2.3 shows that the two-dimensional mean square displacement $MSD(\Delta t)$ is the sum over the two one-dimensional mean square displacements $MSD_x(\Delta t)$ and $MSD_y(\Delta t)$. As we expect no anisotropy in the experimental setup, only the two-dimensional $MSD(\Delta t)$ is calculated from the measured particle trajectories.

A $MSD(\Delta t)$ representation allows for the classification of different modes of diffusion. Three different modes can be distinguished [145]:

1. *Simple diffusion mode*, in which particles undergo simple Brownian diffusion. In this case, the $MSD(\Delta t)$ plot is linear with a slope of $4D$, and can be expressed as [145]:

$$MSD(\Delta t) = 4D\Delta t \tag{2.4}$$
$$4D = 2D_x + 2D_y, \tag{2.5}$$

   where D is the two-dimensional diffusion coefficient and D_x and D_y are the one-dimensional diffusion coefficients for the x and y directions, respectively.

   Figure 2.1 shows a theoretical $MSD_x(\Delta t)$ graph for a particle undergoing Brownian diffusion (graph a).

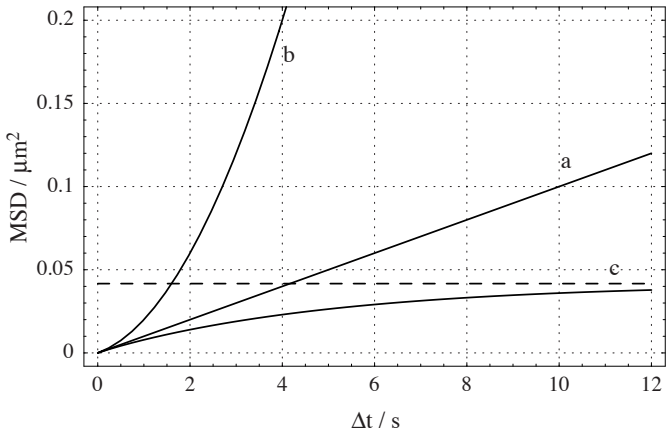

Fig. 2.1 Theoretical one-dimensional MSD as a function of Δt for diffusing particles. The diffusion coefficient is $D_x = 5 \times 10^{-3}\,\mu\mathrm{m}^2/\mathrm{s}$. a) Freely diffusing particle. b) Particle diffusing freely in a medium flowing at $v_x = 100\,\mathrm{nm/s}$. c) Particle diffusing freely in a confined rectangular space with a length of $L_x = 0.5\,\mu\mathrm{m}$. The dashed line represents the asymptotic behavior $L_x^2/6$.

2. *Directed diffusion mode (simple diffusion in a flowing medium)*, in which a particle moves in a direction at constant drift velocity (v_x, v_y) with random diffusion superimposed (two-dimensional diffusion coefficient D). The $MSD(\Delta t)$ plot is parabolic with a differential coefficient of $4D$ at time 0 (initial slope) [145]:

$$MSD(\Delta t) = 4D\Delta t + v^2(\Delta t)^2 \tag{2.6}$$

$$v^2 = v_x^2 + v_y^2. \tag{2.7}$$

Figure 2.1 shows a theoretical $MSD_x(\Delta t)$ graph for a particle undergoing directed diffusion (graph b).

3. *Restricted diffusion mode (simple diffusion in a confined area)*, in which a particle undergoes Brownian diffusion within a limited area and cannot move out of the area during the time of observation $(0 \le x \le L_x, 0 \le y \le L_y)$. The $MSD(\Delta t)$ plot can be expressed as [145]:

$$MSD_x(\Delta t) = \frac{L_x^2}{6} - 16\frac{L_x^2}{\pi^4} \sum_{n=1\ (odd)}^{\infty} \frac{1}{n^4} \exp\Big(- \Big(\frac{n\pi}{L_x}\Big)^2 D_x \Delta t\Big). \tag{2.8}$$

An analogous expression holds for $MSD_y(\Delta t)$. The two-dimensional $MSD(\Delta t)$ is the sum of $MSD_x(\Delta t)$ and $MSD_y(\Delta t)$ (equation 2.3).

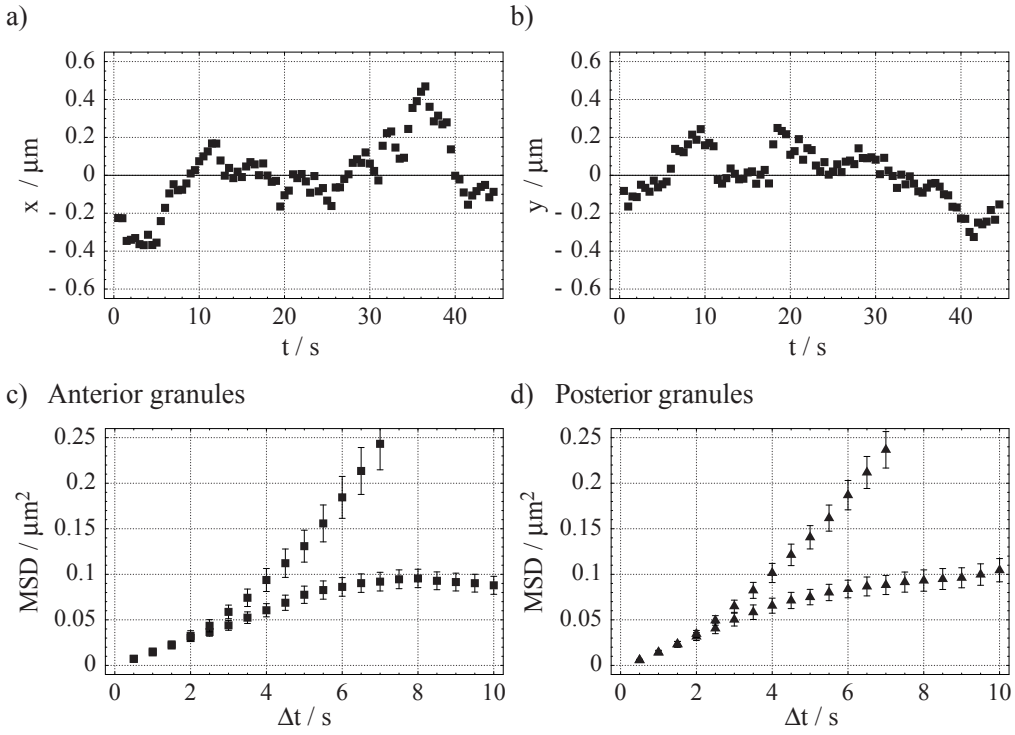

Fig. 2.2 Diffusion of granules in living *C. elegans* embryos. a) and b) The x and y coordinates of a single granule as a function of time. Recording was performed at 2 Hz. The error is position detection is estimated to be ±50 nm. c) and d) $MSD(\Delta t)$ plots of four randomly chosen granules, c) two at the anterior and d) two at the posterior. Error bars represent the standard error of mean.

The slope of $MSD_x(\Delta t)$ at time 0 is $2D_x$, and the curve asymptotically approaches $L_x^2/6$. Figure 2.1 shows a theoretical $MSD_x(\Delta t)$ graph for a particle diffusing freely in a confined space (graph c).

2.1.2 Application to yolk granules

92 granules located close to the anterior cell cortex of the one cell stage *C. elegans* embryo and 90 granules located close to the posterior cell cortex were automatically tracked from the DIC images ($\delta t = 0.5$ s, $N = 50$) using a SPT algorithm (methods section, chapter 6.1). By repeatedly tracking an immobilized structure of a size similar to the size of a yolk granule, the absolute error in position detection is estimated to be about ±50 nm. Please refer to "Ch2M01 Tracked YG.mov" for an animation of a tracked yolk granule using the SPT algorithm (scale bar: 2 μm).

Figure 2.2 a) and b) shows the x and y position of two arbitrarily chosen

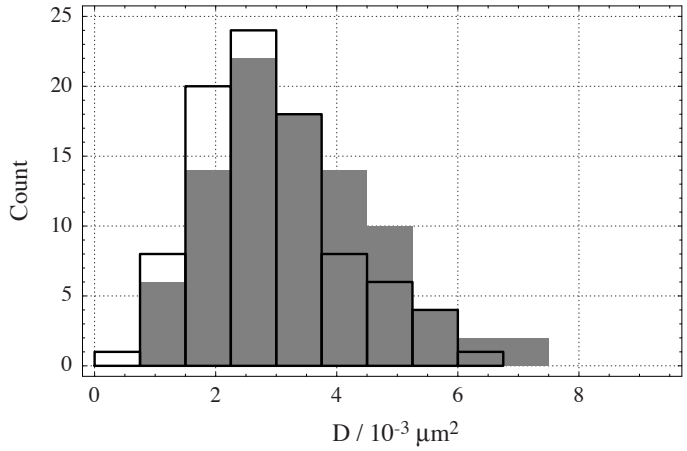

Fig. 2.3 Histogram analysis of diffusion coefficients for granules located close to the anterior (gray, $N = 92$) or the posterior (boxed, $N = 90$) cortex. The diffusion coefficients were computed for $\Delta t \leq 5s$. Binning size is $0.75 \times 10^{-3}\,\mu\mathrm{m}^2/\mathrm{s}$. The mean diffusion coefficient for granules at the anterior is $D_A = (3.3 \pm 1.4) \times 10^{-3}\,\mu\mathrm{m}^2/\mathrm{s}$, at the posterior it is $D_P = (2.9 \pm 1.2) \times 10^{-3}\,\mu\mathrm{m}^2/\mathrm{s}$.

yolk granules as a function of time. Figure 2.2 c) and d) are $MSD(\Delta t)$ plots of four randomly chosen granules, two at the anterior and two at the posterior. From the shapes of the graphs one can conclude that one of each is freely diffusing in a confined volume (lower graphs, compare to figure 2.1), whereas the other is diffusing in a flowing medium (upper graphs, compare to figure 2.1).

For $\Delta t \leq 5\,\mathrm{s}$, $MSD(\Delta t)$ plots of the 182 granules were characteristic for either simple diffusion or simple diffusion in a flowing medium. The $MSD(\Delta t)$ plots were fitted to equation 2.6 using the two dimensional diffusion coefficient D and the speed of the flowing medium v as fitting parameters ($\Delta t \leq 5\,\mathrm{s}$). Figure 2.3 shows a histogram distribution of all fitted two-dimensional diffusion coefficients D. For the 92 granules located close to the anterior cell cortex, the average diffusion coefficient D_A computes to $D_A = (3.3 \pm 1.4) \times 10^{-3}\,\mu\mathrm{m}^2/\mathrm{s}$, for the 90 granules close to the posterior cell cortex it is $D_P = (2.9 \pm 1.2) \times 10^{-3}\,\mu\mathrm{m}^2/\mathrm{s}$.

Furthermore, the average diameter of the tracked yolk granules was determined from the DIC recordings, it is $0.85 \pm 0.11\,\mu\mathrm{m}$ for granules at the anterior and $0.83 \pm 0.12\,\mu\mathrm{m}$ for granules located at the posterior cortex.

2.2 Spindle severing experiments

To test for the presence of tensile stress within the spindle of the one cell stage *C. elegans* embryo, spindle severing experiments were performed in wild-type, *par-2* and *par-3* embryos. To remove the spindle midzone, two experimental approaches were followed. First, the spindle was physically destroyed by severing with a pulsed UV laser (methods section, chapter 6.1). Second, the removal of a *C. elegans* kinesin homologous to XKCM1/MCAK [147, 148, 27, 55] (referred to as CeMCAK) by the method of double stranded RNA mediated interference (RNAi) [101] also results in a diminished spindle midzone (methods section, chapter 6.1).

2.2.1 Severing at anaphase in the wild-type embryo

To verify the disappearance of the spindle midzone, single embryo immunofluorescence experiments (methods section, chapter 6.1) with anti-tubulin antibodies were performed. This method allows for a precise timing of the cell cycle stage of fixed embryos. A single embryo is imaged up to the desired stage and irradiated with the UV laser, if applicable [83]. Following a rapid freeze, the embryo is stained using standard procedures [149]. While the spindle midzone is still visible in the wild-type control embryo (figure 2.4 a), it has disappeared after irradiation with the UV laser (figure 2.4 b). Astral microtubules are seemingly unaffected. The same is true after RNAi of *CeMCAK* (figure 2.4 c).

It is concluded that both experimental approaches are capable of selectively destroying the spindle midzone.

Wild-type *C. elegans* embryos were recorded using time-lapse DIC microscopy. At the beginning of anaphase B, identified by a slight transverse displacement of the posterior spindle pole, about 10 to 20 laser shots were applied to the spindle midzone. This resulted in a dramatic increase of pole-to-pole distance (figure 2.5 panel two, compare to panel one). In the *CeMCAK* (RNAi) embryos, time-lapse DIC recordings reveal that the spindle breaks apart at anaphase, also resulting in a sudden increase of pole-to-pole distance (figure 2.5 panel three, compare to panel one).

In both experimental situations the two spindle poles move outwards in direction of the cell cortex at speeds that are increased three-fold when compared to the unperturbed wild-type embryo. Most interestingly, the two spindle poles behave differently after the cut: the posterior spindle pole travels faster and further than the anterior one, and it moves transverse to the anterior-posterior (AP) axis as it gets close to the cortex, indicating the beginning of transverse oscillations (see figure 2.5 last frame). Note that

these oscillations occur about 20 to 30 seconds earlier than in untreated wild-type embryos. The anterior spindle pole quickly comes to rest far away from the cell cortex.

To analyze these results in further detail, spindle poles were manually tracked from the time lapse recordings. The x component (along the AP axis) $|v_x^{max}|$ of peak velocities as well as the displacement as a function of time after breakage were computed for each spindle pole (table 2.1). Repeated tracking of the same movie allowed to estimate the error in peak velocity determination to be about $\pm 0.05\,{}^{\mu m}/_{s}$. For the irradiated embryos, 34 experiments were performed. For the *CeMCAK* (RNAi) experiment, 20 embryos were recorded. As a comparison 20 untreated wild-type embryos were also analyzed. Figure 2.6 a) shows the average displacement of each

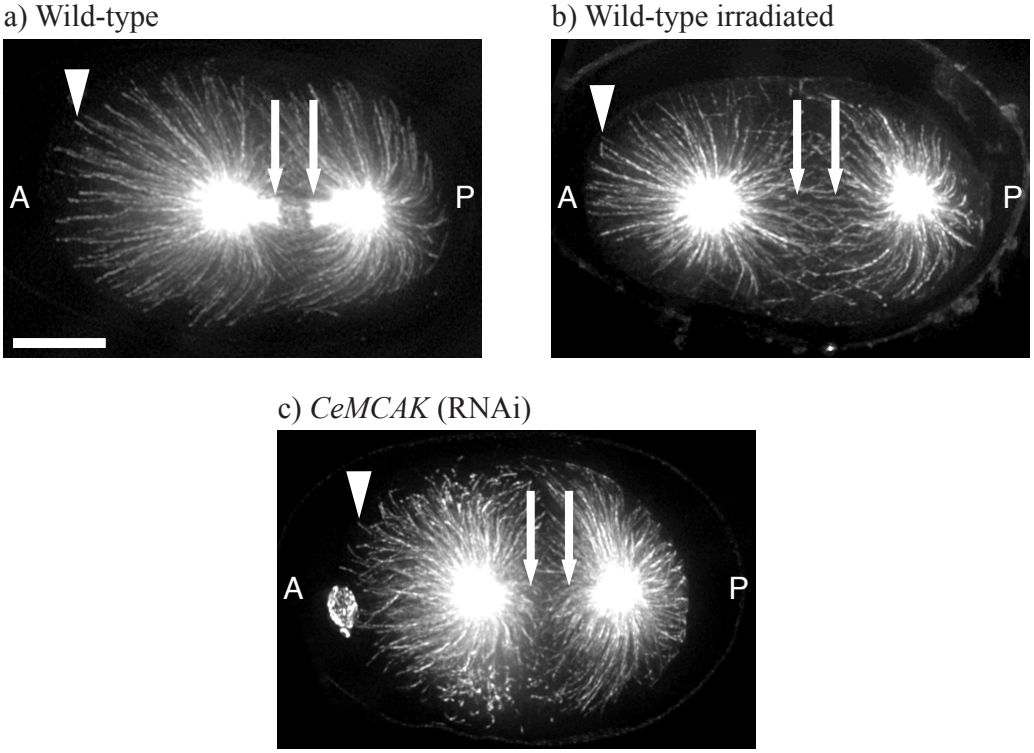

Fig. 2.4 Spindle midzone viewed by indirect immunofluorescence with anti-tubulin antibody. All embryos are in anaphase B. Anterior (A) is on the left, posterior (P) is on the right. a) In unirradiated wild-type embryos, both the spindle microtubules (arrows) and the astral microtubules (arrowheads) are visible. b) and c) Both in the irradiated wild-type and the *CeMCAK* (RNAi) embryos astral microtubules are visible (arrowheads), but spindle microtubules are not (arrows). Scale bar: $10\,\mu$m.

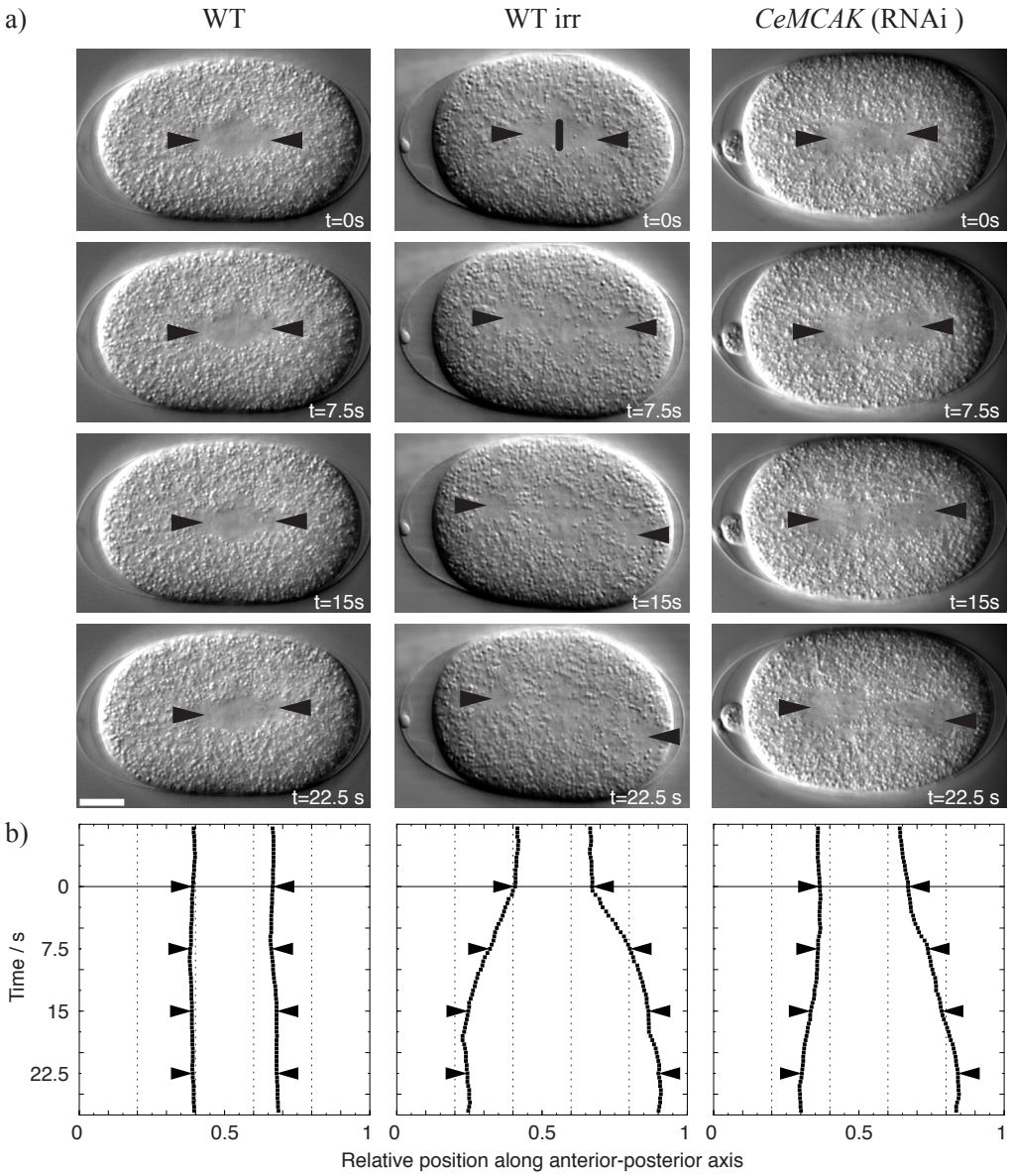

Fig. 2.5 Pole-to-pole distances increase after spindle severing. a) DIC image series of a wild-type *C. elegans* embryo, a wild-type embryo where the spindle has been severed with the UV laser at $t = 0\,\mathrm{s}$ (vertical bar), and a *CeMCAK* (RNAi) embryo. All series start at the beginning of anaphase B. Anterior is on the left, posterior on the right. Spindle poles are indicated (arrowheads). Scale bar: $10\,\mu\mathrm{m}$. b) Corresponding traces of spindle pole position along the AP axis as a function of time. Arrowheads indicate the times for which the frames in a) are displayed. Please refer to the movies "Ch2M02 WT WTirr.mov" and "Ch2M03 CeMCAK.mov".

WT		WT irr		*CeMCAK* (RNAi)	
A	P	A	P	A	P
$\lvert v_x^{max}\rvert$ (μm/s)	$\lvert v_x^{max}\rvert$ (μm/s)	$\lvert v_x^{max}\rvert$ (μm/s)	$\lvert v_x^{max}\rvert$ (μm/s)	$\lvert v_x^{max}\rvert$ (μm/s)	$\lvert v_x^{max}\rvert$ (μm/s)
0.143	0.177	0.566	0.856	0.193	0.419
0.185	0.332	0.291	0.846	0.249	0.593
0.325	0.342	0.559	0.816	0.159	0.395
0.218	0.223	0.515	0.733	0.178	0.466
0.21	0.373	0.642	0.699	0.245	0.483
0.242	0.263	0.663	1.019	0.16	0.283
0.106	0.318	0.479	0.833	0.44	0.665
0.321	0.387	0.527	1.04	0.362	0.644
0.325	0.281	0.687	1.321	0.363	0.384
0.251	0.276	1.175	1.106	0.141	0.351
0.14	0.241	0.566	0.905	0.262	0.506
0.162	0.241	0.529	0.966	0.384	0.371
0.121	0.185	0.863	0.803	0.726	0.425
0.101	0.283	1.013	1.246	0.233	0.554
0.122	0.245	0.362	0.984	0.384	0.423
0.103	0.185	0.761	1.061	0.162	0.445
0.152	0.202	0.855	1.165	0.124	0.415
0.18	0.262	0.972	1.232	0.326	0.516
0.134	0.183	0.61	0.74	0.225	0.539
0.303	0.282	0.91	1.02	0.505	0.431
		0.546	0.702		
		0.492	0.895		
		0.57	0.723		
		0.66	0.767		
		1.	0.708		
		0.879	0.892		
		0.502	0.85		
		0.639	0.989		
		0.429	0.633		
		0.769	0.78		
		0.543	0.802		
		0.502	0.964		
		0.545	1.023		
		0.624	0.894		
0.192	0.264	0.654	0.912	0.291	0.465
$\pm$0.078	$\pm$0.063	$\pm$0.202	$\pm$0.171	$\pm$0.149	$\pm$0.098

Table 2.1 Peak velocities $\lvert v_x^{max}\rvert$ of anterior (A) and posterior (P) spindle poles during anaphase B in wild-type (WT, $N = 20$), wild-type irradiated (WT irr, $N = 34$) and *CeMCAK* (RNAi) (*CeMCAK* (RNAi), $N = 20$) embryos. The absolute error for each $\lvert v_x^{max}\rvert$ is estimated to be $\pm 0.05\,\mu$m/s. Bottom row: average values $\pm$ standard deviation.

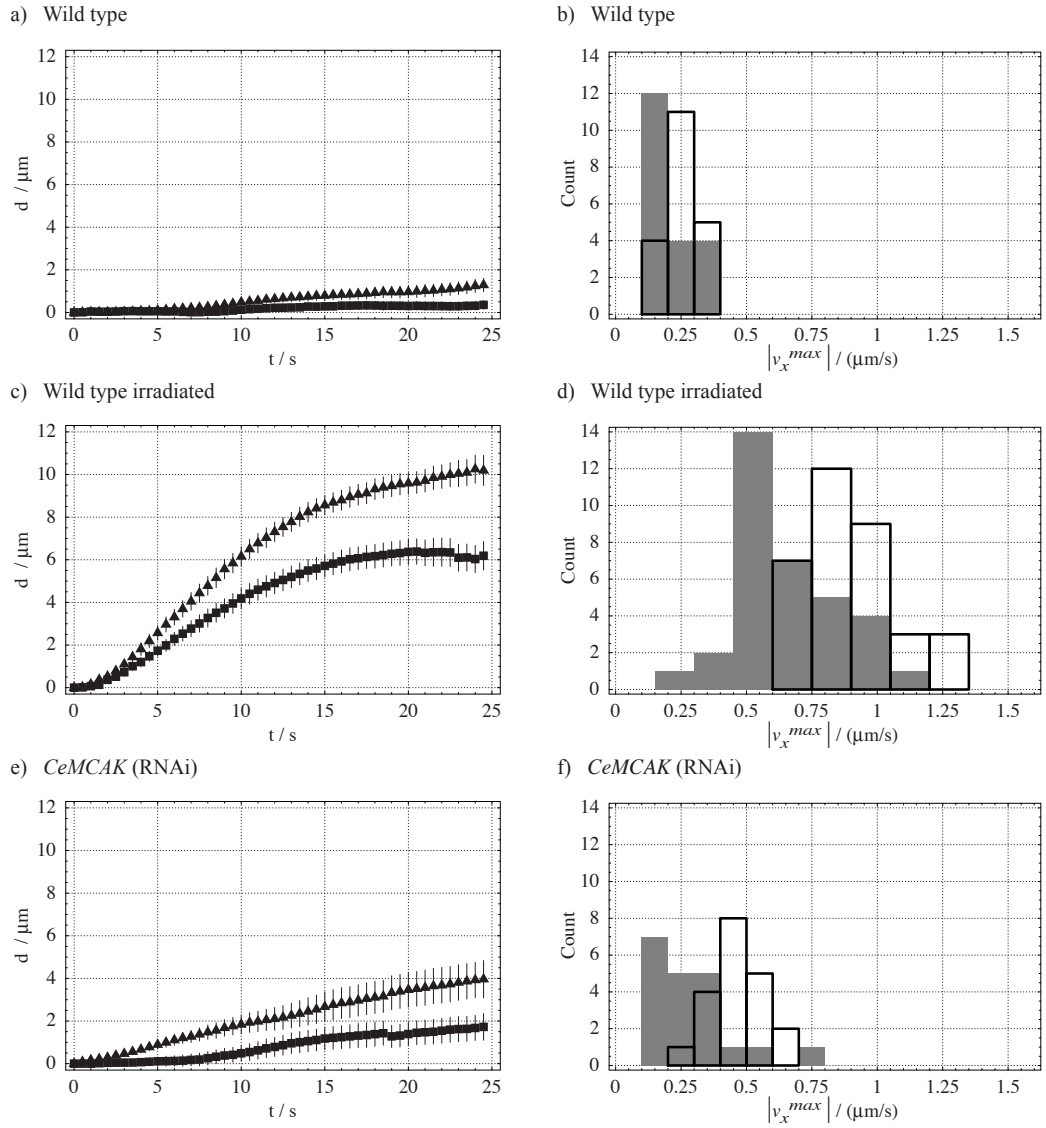

Fig. 2.6 Spindle pole movement in wild-type, wild-type irradiated and *CeMCAK* (RNAi) embryos. a), c) and e) Average displacement d of the anterior (■) and the posterior (▲) spindle pole as a function of time. Actual movements are in opposite directions. For c) and e), $t = 0\,\mathrm{s}$ corresponds to the time of spindle breakage, which can be determined to about $\pm 2\,\mathrm{s}$. Bars represent the standard error of mean with a confidence interval of 0.95. b), d) and f) Histogram analysis of the measured peak velocities $|v_x^{max}|$ of the anterior (gray) and the posterior (boxed) spindle pole from table 2.1. Binning size is $0.1\,\mu\mathrm{m/s}$ for b) and f), and $0.15\,\mu\mathrm{m/s}$ for d).

spindle pole as a function of time after breakage. On can see that in the irradiated wild-type as well as in the *CeMCAK* (RNAi) embryos the posterior spindle pole travels a greater distance than the anterior one. Table 2.1 is a complete list of peak velocities $|v_x^{max}|$ with the mean values, figure 2.6 b) displays the corresponding histogram distributions. For spindle severing with the UV laser, the hypothesis that the mean peak velocities of the posterior and the anterior spindle pole are equal after severing is rejected when submitting the data (table 2.1) to a two-sided mean difference test (significance level of 99%, where 0% corresponds to no significance and 100% to full significance). The same behavior is observed for the *CeMCAK* (RNAi) experiments, indicating that mean peak velocities are different for the two spindle poles in these cases.

In summary, after severing the spindle with the UV laser the posterior spindle pole travels on average at an about 40% higher peak velocity than the anterior one, it travels further, and it undergoes transverse oscillations in proximity of the cell cortex.

WT irr metaphase	
A	P
$\lvert v_x^{max}\rvert (\mu\text{m}/\text{s})$	$\lvert v_x^{max}\rvert (\mu\text{m}/\text{s})$
0.359	0.51
0.15	0.215
0.237	0.336
0.278	0.116
0.457	0.6
0.156	0.554
0.429	0.709
0.571	0.588
0.634	0.505
0.569	0.814
0.465	0.576
0.393	0.648
0.489	0.647
0.859	0.845
0.432	0.547
$\pm$0.194	$\pm$0.207

Table 2.2 Peak velocities $|v_x^{max}|$ of anterior (A) and posterior (P) spindle poles following spindle severing with the UV laser during late metaphase in the wild-type embryo (WT irr metaphase, $N = 14$). The absolute error for each $|v_x^{max}|$ is estimated to be $\pm 0.05\,\mu\text{m}/\text{s}$. Bottom row: average values $\pm$ standard deviation.

2.2.2 Severing at metaphase in the wild-type embryo

To study cell cycle dependent variations of tensile stress within the spindle structure, spindle severing experiments were performed during metaphase. Embryos were severed with the UV laser between 10 and 20 seconds after the pronuclear envelope was no longer visible in DIC. At this time the spindle is built up, but the sister chromatids as well as the spindle poles have not yet begun to separate. In *C. elegans* embryos there is no clear transition from anaphase A (chromosome separation) to anaphase B (spindle elongation), as a large part of chromosome segregation is accomplished by spindle elongation [142]. However, the embryo still is in metaphase 10 to 20 s after nuclear envelope breakdown (as judged by DIC). Table 2.2 presents the peak velocities of the anterior and the posterior spindle pole following spindle severing with the UV laser between 10 and 20 s after nuclear envelope breakdown. Both spindle poles travel at lower peak velocities when compared to spindle severing at the time of anaphase ($|v_x^{max}|$ for the anterior is reduced to 66%, and $|v_x^{max}|$ for the posterior to 60%). The mean value for $|v_x^{max}|$ of the anterior spindle poles is 21% lower than for the posterior spindle poles. However, with the current statistics (N=14) the hypothesis that the mean peak velocities of the posterior and the anterior spindle pole are equal after severing fails to be rejected when submitting the data (table 2.2) to a two-sided mean difference test (significance level of 99%).

2.2.3 *par-2* and *par-3* mutant backgrounds

To study how the *par* genes influence the properties of spindle pole movement following removal of the spindle, spindle severing experiments were performed in *par-2* and *par-3* mutant embryos. In both of these mutant embryos, the spindle stays symmetrically positioned throughout anaphase. Spindle severing was either done by irradiation with the pulsed UV laser or by removal of both CeMCAK and PAR-2 or both CeMCAK and PAR-3 by RNAi.

When the spindle was severed with the UV laser in *par-2* and *par-3* mutant embryos, in both experimental situations both spindle poles immediately start to move after the cut, as can be seen in figure 2.7. However, in the *par-2* mutant both spindle poles now travel at similar speeds (table 2.3) and about the same distance (figures 2.7 and 2.8). The same is true in the *par-3* mutant, both spindle poles travel at similar but higher speeds (table 2.3), and they now both move all the way to the cortex (see figures 2.7 and 2.8).

Both for *par-2* (N=30) and *par-3* (N=20), the hypothesis that the mean peak velocities of the posterior and the anterior spindle pole are equal after

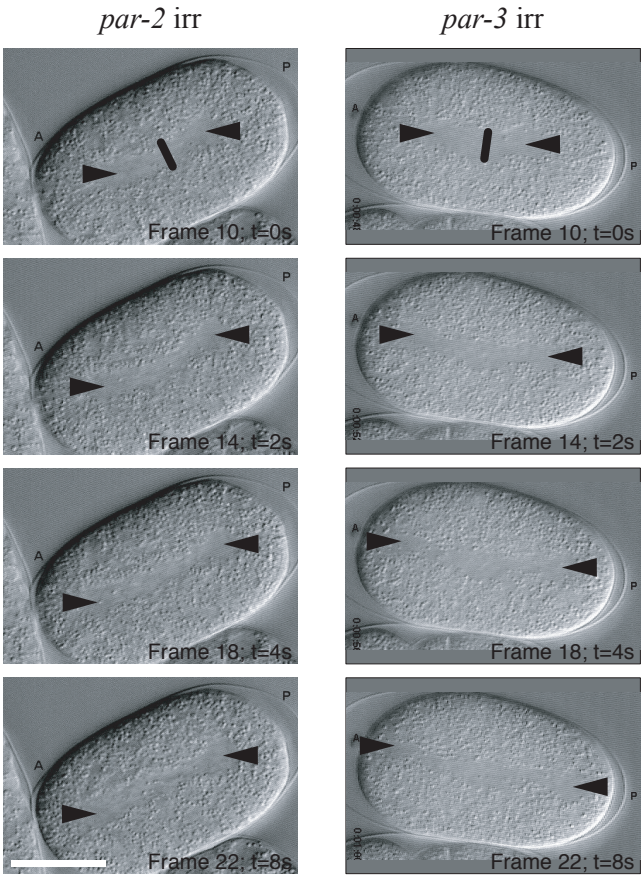

Fig. 2.7 DIC image series of a *par-2* (it5) and a *par-3* (it71) *C. elegans* embryo where the spindle has been severed with the UV laser at $t = 0\,\mathrm{s}$ at the location indicated by the bar. Anterior is on the left, posterior on the right. Spindle poles are indicated (arrowheads). Please refer to the movies "Ch2M04 Par2irr.mov" and "Ch2M05 Par3irr.mov" (corresponding frame numbers are indicated). Scale bar: $20\,\mu\mathrm{m}$.

par-2 irr		*par-3* irr	
A	P	A	P
$\lvert v_x^{max}\rvert(\mu\text{m}/\text{s})$	$\lvert v_x^{max}\rvert(\mu\text{m}/\text{s})$	$\lvert v_x^{max}\rvert(\mu\text{m}/\text{s})$	$\lvert v_x^{max}\rvert(\mu\text{m}/\text{s})$
0.75	0.716	1.205	1.016
0.541	0.843	0.646	0.843
0.759	0.786	0.747	0.916
0.752	0.477	0.876	0.882
0.602	0.814	0.799	0.955
0.544	0.677	1.199	1.183
0.61	0.373	0.772	1.24
0.62	0.491	1.365	0.96
0.832	0.854	0.771	0.712
0.885	0.885	0.942	0.894
0.567	0.402	0.71	0.741
0.727	0.886	1.003	0.864
0.569	0.684	0.791	0.824
0.759	0.557	0.731	0.675
0.63	0.697	0.498	0.607
0.77	0.638	1.205	1.016
0.906	0.711	0.526	0.802
0.706	0.57	0.756	1.023
0.323	0.419	1.222	0.856
0.457	0.45	1.061	0.976
0.745	0.527		
0.707	0.292		
0.359	0.493		
0.549	0.336		
0.635	0.534		
0.512	0.414		
0.798	0.55		
0.388	0.608		
0.56	0.884		
1.039	0.837		
0.653	0.614	0.891	0.899
$\pm$0.164	$\pm$0.181	$\pm$0.247	$\pm$0.157

Table 2.3 Peak velocities $\lvert v_x^{max}\rvert$ of anterior (A) and posterior (P) spindle poles during anaphase B in *par-2 (it5)* irradiated (*par-2* irr, $N = 30$) and *par-3 (it71)* irradiated embryos (*par-3* irr, $N = 20$) embryos. The absolute error for each $\lvert v_x^{max}\rvert$ is estimated to be $\pm 0.05\,\mu\text{m}/\text{s}$. Bottom row: average values $\pm$ standard deviation.

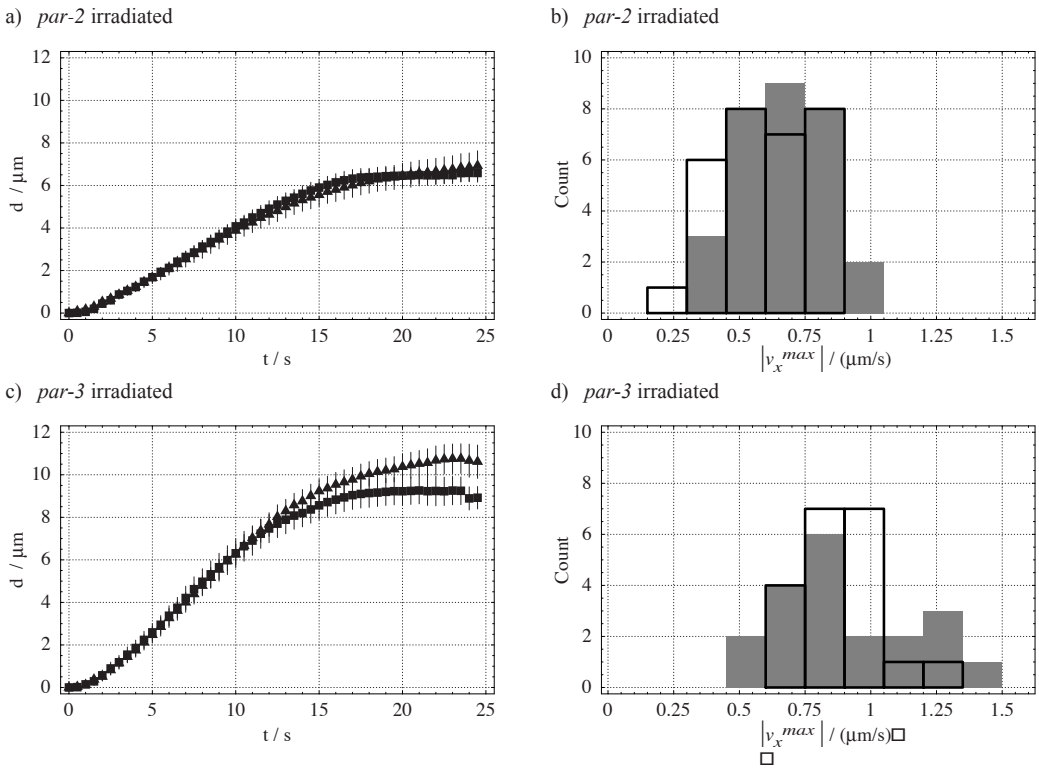

Fig. 2.8 Spindle pole movement in *par-2* (it5) irradiated and *par-3* (it71) irradiated embryos. a) and c) Average displacement d of the anterior (■) and the posterior (▲) spindle pole after irradiation as a function of time, $t = 0\,\mathrm{s}$ corresponds to the time of irradiation. Actual movements are in opposite directions. Bars represent the standard error of mean with a confidence interval of 0.95. b) and d) Histogram analysis of the measured peak velocities $|v_x^{max}|$ of the anterior (gray) and the posterior (boxed) spindle pole from table 2.3. Binning size is $0.15\,{}^{\mu\mathrm{m}}/_{\mathrm{s}}$.

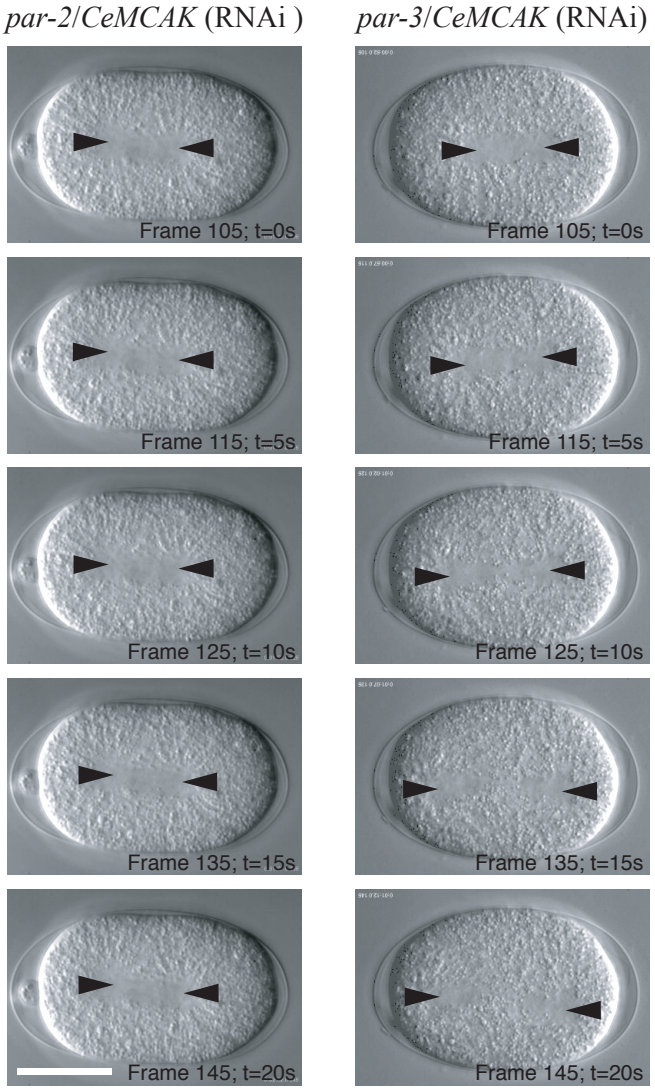

Fig. 2.9 DIC image series of *par-2/CeMCAK* double RNAi and *par-3/CeMCAK* double RNAi embryos. Series start at the beginning of anaphase B. Anterior is on the left, posterior is on the right. Spindle poles are indicated (arrowheads). Note that spindle breakage still occurs in the *par-3/CeMCAK* double RNAi, whereas it does not take place in the *par-2/CeMCAK* double RNAi. Please refer to the movies "CH2M06 Par2 CeMCAK RNAi.mov" and "Ch2M07 Par3 CeMCAK RNAi.mov" (corresponding frame numbers are indicated). Scale bar: 20 μm.

severing fails to be rejected (significance level of 99%), indicating that the mean peak velocities are likely to be the same for both spindle poles in these mutants. Moreover, the hypothesis that each spindle pole in irradiated *par-2* mutants exhibits the same mean peak velocity as the anterior spindle pole in irradiated wild-type embryos fails to be rejected (significance level of 99%). The same is true in comparing both spindle poles in irradiated *par-3* mutants with the posterior spindle pole in irradiated wild-type mutants. This indicates that the peak velocity of the anterior spindle pole in wild-type and that of both spindle poles in *par-2* mutants are likely to be the same, and the peak velocity of the posterior spindle pole in wild-type and the peak velocities of both spindle poles after spindle severing in *par-3* mutants are likely to be the same.

When removing the spindle midzone by RNAi of CeMCAK, the following was observed: no spindle breakage events occurred in *par-2/CeMCAK* double RNAi experiments. To assure that coinjecting dsRNA corresponding to PAR-2 and dsRNA corresponding to CeMCAK results in the cumulative effect, only the embryos displaying both the polar body defect (resulting from the removal of CeMCAK) and a symmetric division (resulting from the removal of PAR-2) were analyzed (N=12). Out of these, none displayed a spindle breakage phenotype (figure 2.9). However, when both PAR-3 and CeMCAK were removed by RNAi (taking the same measures for analyzing the cumulative effect), spindle breakage still occurred in 4 out of 14 embryos (figure 2.9).

2.2.4 Disintegration of centrosomes

Instead of performing a spindle severing experiment with the UV laser and measuring peak velocities of both spindle poles, the same results should be obtained when one of the spindle poles is destroyed using the laser, and the movement of the remaining intact spindle pole is analyzed. As a control, experiments were repeated by disintegrating either centrosome in wild-type , *par-2* and *par-3* embryos and measuring peak velocities of the intact spindle pole. Figure 2.10 shows a DIC time lapse of an anterior and a posterior centrosome disintegration (CD). The movement of the intact spindle pole is marked (arrowheads). Following disintegration of the posterior centrosome, the anterior spindle pole travels at a lower peak velocity than the posterior spindle pole after disintegration of the anterior centrosome. Furthermore, the posterior spindle pole travels all the way to the cortex and starts to oscillate transverse to the anterior-posterior axis, whereas the anterior spindle positions itself stably.

Table 2.4 lists the x component (along the AP axis) $|v_x^{max}|$ of peak ve-

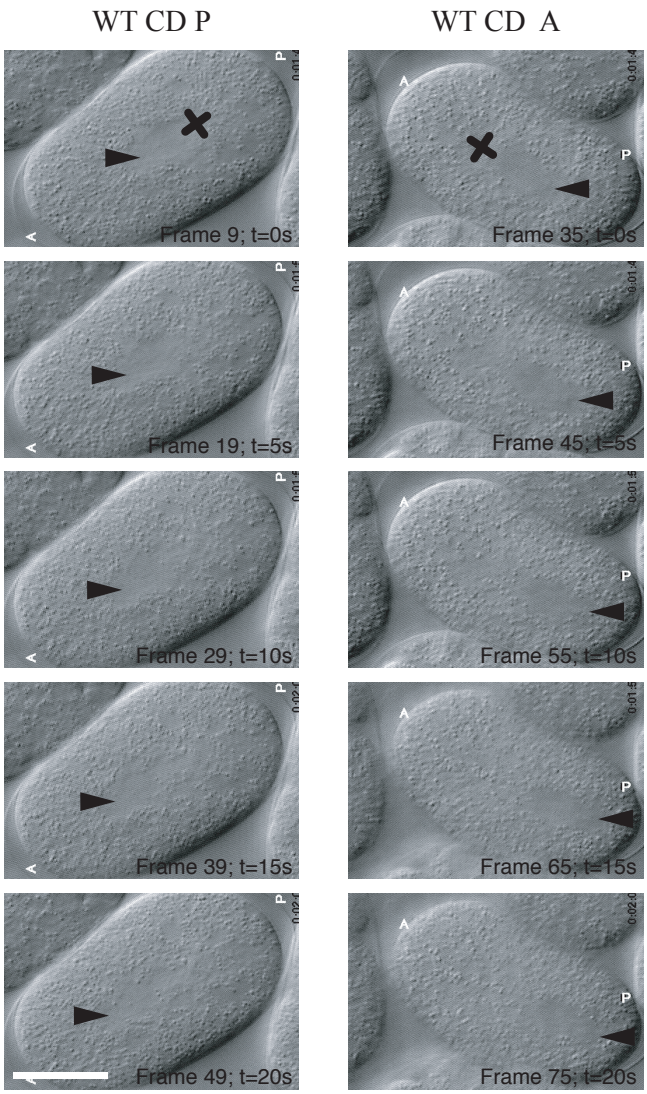

Fig. 2.10 DIC image series of an anterior and a posterior centrosome disintegration (CD) in the wild-type embryo (WT CD A and WT CD P, respectively). Series start at the beginning of anaphase B. Anterior is on the left, posterior on the right. The intact spindle poles are indicated (arrowheads). CD is indicated by a cross. Please refer to the movies "Ch2M08 A CD WT.mov" and "Ch2M09 P CD WT.mov" (corresponding frame numbers are indicated). Scale bar: 20 μm.

locities of intact spindle poles after anterior and posterior centrosome disintegration experiments in wild-type, *par-2* and *par-3* embryos. The hypothesis that the mean peak velocities of the posterior and the anterior spindle

WT CD		*par-2* CD		*par-3* CD	
A	P	A	P	A	P
$\lvert v_x^{max}\rvert$ (μm/s)	$\lvert v_x^{max}\rvert$ (μm/s)	$\lvert v_x^{max}\rvert$ (μm/s)	$\lvert v_x^{max}\rvert$ (μm/s)	$\lvert v_x^{max}\rvert$ (μm/s)	$\lvert v_x^{max}\rvert$ (μm/s)
0.537	0.711	0.708	0.612	0.622	0.969
0.733	0.662	0.732	0.666	0.869	0.625
0.527	0.662	0.719	0.524	0.856	0.895
0.522	0.564	0.536	0.494	1.174	1.063
0.556	1.037	0.537	0.474	0.99	0.451
0.717	0.464		0.605	0.492	0.841
0.649	0.944		0.528	0.734	0.895
0.597	0.886		0.402	0.729	0.847
0.394	0.845		0.57	0.887	1.1
0.672	0.807				
0.403	0.615				
0.429	0.713				
0.477	0.703				
0.555	0.74	0.646	0.542	0.817	0.854
±0.114	±0.159	±0.101	±0.081	±0.202	±0.205

Table 2.4 Peak velocities $\lvert v_x^{max}\rvert$ of anterior (A) and posterior (P) spindle poles during anaphase B in wild-type (WT CD, $N = 34$), *par-2 (it5)* (*par-2* CD, $N = 5$ anterior and $N = 9$ posterior) and *par-3 (it71)* CD embryos (*par-3* CD, $N = 9$). The absolute error for each $\lvert v_x^{max}\rvert$ is estimated to be $\pm 0.05\,\mu$m/s. Bottom row: average values ± standard deviation.

pole in the wild-type centrosome disintegrations are equal after centrosome disintegration is rejected when submitting the data (N=13, table 2.4) to a two-sided mean difference test (significance level of 99%). This indicates that the mean peak velocities are different for the two spindle poles. Moreover, both for *par-2* centrosome disintegrations (anterior: N=5, posterior: N=9) and *par-3* centrosome disintegrations (N=9), the hypothesis that the mean peak velocities of the posterior and the anterior spindle pole are equal after centrosome disintegration fails to be rejected (significance level of 99%), indicating that mean peak velocities are likely to be the same for both spindle poles after centrosome disintegration in these mutants.

In summary, disintegration of either centrosome qualitatively confirms the results obtained by performing spindle severing experiments.

2.3 Optically induced centrosome disintegration

To distinguish between global and confined cortical force generation and to study the phenomenon of transverse oscillations by testing for the presence of tensile stress within a microtubule aster, *optically induced centrosome disintegration* (OICD) experiments were performed in wild-type, *par-2* and *ags-3* (RNAi) embryos. There is a distinct difference to the CD experiments performed in section 2.2.4, where the remaining intact centrosome was tracked and the trajectory analyzed. Here, OICD is performed and the movement of astral microtubules and centrosomal fragments towards the cell cortex is analyzed.

It should be noted that the use of a solid state UV laser is crucial to the experiments in this section, as the outward yolk granule flow is not reproducibly detectable when using the N_2 laser with the PALM setup. This is most likely caused by the differences in the beam profiles.

One aim of the experiments in the wild-type embryo is to compare the distribution of yolk granule flow following centrosome disintegration of a moving centrosome with the distribution following the disintegration of a stationary centrosome, as to study differences in the tensile stress within each spindle aster. Yolk granules can attach to microtubules and sometimes move towards the minus end in a dynein-dependent fashion [64]. Therefore they can be used to track the movement of centrosomal fragments following OICD.

The time of late anaphase was chosen for OICD. At this time the posterior spindle pole oscillates transverse to the anterior-posterior axis, whereas the anterior spindle pole assumes a relatively fixed position. The posterior OICD experiments were performed at the time of maximum speed of the posterior spindle pole, just as it crosses the AP axis. They therefore represent the class of moving centrosomes. As the anterior spindle pole remains relatively fixed, anterior OICD experiments represent the class of stationary centrosomes.

2.3.1 Centrosome disintegration in the wild-type embryo

To completely destroy a centrosome, OICD was performed in the following way (methods section, chapter 6.1): 100 UV laser pulses at 50 Hz were shot at the sample while the microscope stage was rapidly moved around the borders of a $2 \times 2\,\mu$m rectangle. As the laser is focused into a fixed point in the focal plane, the boundaries of a $2 \times 2\,\mu$m area are irradiated. As the region of high microtubule density around a centrosome has a diameter of about $3\,\mu$m, this should result in the complete destruction of a centrosome if sufficient pulse energies are employed.

To demonstrate the effect of OICD, single embryo immunofluorescence was performed on embryos where the anterior or the posterior centrosome has been disintegrated. The embryos were stained for DNA, tubulin and γ-tubulin, a centrosomal marker [150]. Figure 2.11 shows the distribution of DNA, tubulin and γ-tubulin in two typical examples. Both for the anterior and the posterior centrosome disintegrations it is demonstrated that a complete destruction was accomplished. The anterior centrosome fragmented into three "mini-centrosomes". For the OICD experiment of the posterior centrosome, microtubules were dragged towards the cortex and lined up along it (figure 2.11). In both cases, levels of γ-tubulin are substantially reduced at centrosomes that underwent OICD (compare to the intact centrosomes). The DNA is placed in two distinct regions along the spindle, demonstrating that both embryos are in late anaphase. It is concluded that OICD results in a total destruction of a centrosome, whereas the untreated centrosome is unaffected.

To further demonstrate the effect of OICD in living embryos, posterior and anterior centrosome disintegration experiments were performed in a transgenic GFP-α-tubulin embryo. The recording was switched from wide field transmission DIC prior to OICD to spinning-disk-confocal (SDC) fluorescence afterwards. Since UV laser irradiation bleaches the GFP-tubulin in regions close to the irradiated areas, lower UV laser powers have to be used in comparison to OICD experiments performed in DIC only. This allows for the acquisition of images with an acceptable signal to noise ratio in the SDC channel after OICD. However, since the centrosomes are not completely disintegrated, the resulting effects are reduced when comparing them to the OICD experiments in the DIC.

Figure 2.12 displays an image series of an anterior OICD experiment. The time and region of OICD are marked by a black box. After irradiation recording was switched to the SDC channel (900 ms integration time, 50 mW power for the 488 nm argon-ion laser). Although the centrosome was not completely disintegrated, one can see that microtubule-structures move away from the center towards the cortex. Figure 2.13 shows the corresponding posterior OICD experiment. Again, small centrosome-like structures move outwards to the cortex.

For analyzing yolk granule flow following centrosome disintegration, OICD experiments were recorded in transmission DIC at a rate of two frames per second. From these recordings, the flow of individual yolk granules was manually tracked for 12.5 s, starting after the end of irradiation. It should be pointed out that it was usually not possible to follow a single granule for the full period of time. In these cases, tracking was continued by switching to a neighboring granule. For this reason it was not possible to generate

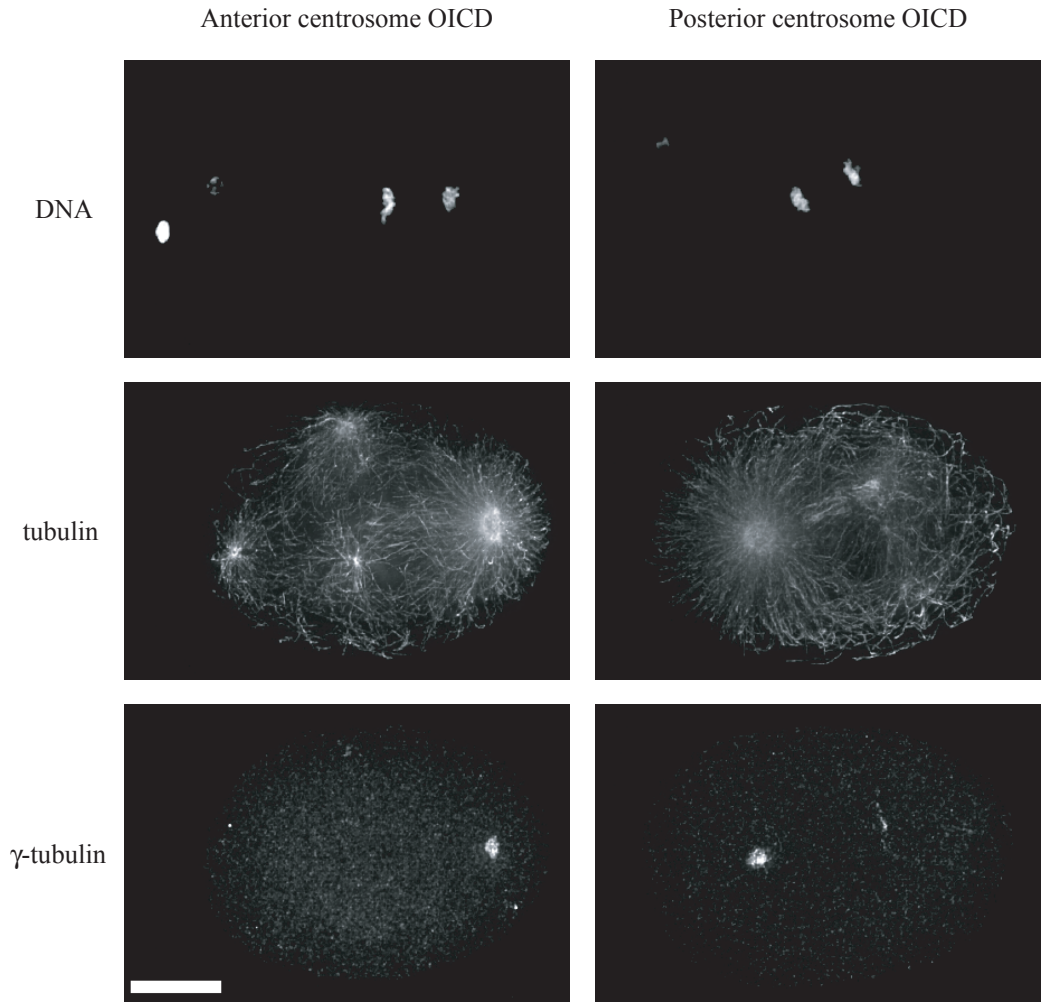

Fig. 2.11 Indirect immunofluorescence following OICD of an anterior (left) and a posterior (right) centrosome. All embryos are wild-type and in anaphase B. Anterior (A) is on the left, posterior (P) is on the right. The distribution of DNA (Hoechst, top), tubulin (anti-tubulin antibody [142], middle) and a γ-tubulin (anti-γ-tubulin antibody [150], bottom) are depicted. Images are projections over the whole depth of the embryo. Scale bar: 10 μm.

an efficient algorithm for automation of the quantification. As the errors in measuring the precise radial distribution of flow are expected to be significantly lower than the differences in the distribution of flow from experiment to experiment, no further effort was directed towards the automation of the quantification.

Figure 2.14 shows a representative DIC image series of an anterior and a posterior OICD experiment. Yolk granule flow is tracked as indicated by dots.

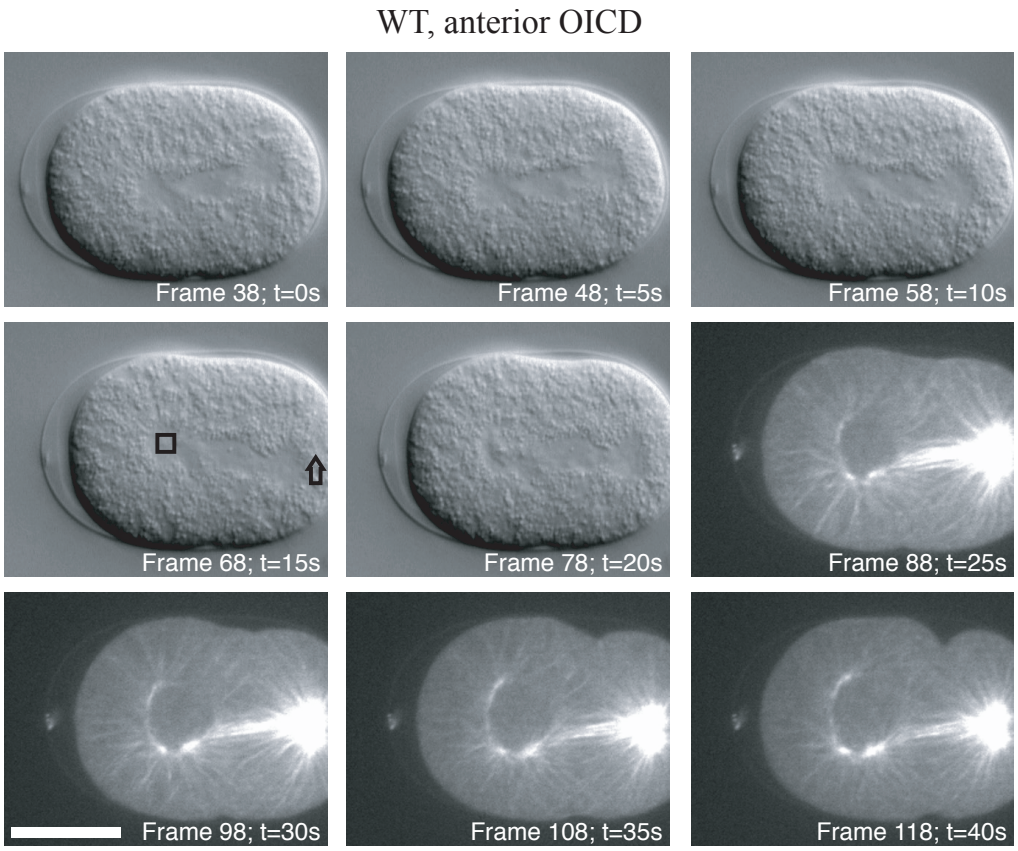

Fig. 2.12 Combined DIC and SDC fluorescence (GFP-tubulin) image series of an anterior centrosome disintegration. OICD is marked by a box. Direction of movement of posterior centrosome prior to OICD is indicated by an arrow. Please refer to the movie "Ch2M10 Ant OICD WT.mov" (corresponding frame numbers are indicated). Scale bar: 20 μm.

First of all, in both cases most of the yolk granules travel away from where the centrosome was originally positioned. Furthermore, one can see that for the anterior centrosome, representing the class of stationary centrosomes, the yolk granules flow away from the centrosome in a symmetric fashion. However, the initial flow of yolk granules for the posterior OICD, representing the class of moving centrosomes, is biased towards the direction of movement of the posterior spindle pole prior to OICD (indicated by an arrow).

The radial speed distribution $v(\phi)$ of flow of granules was computed in the following way: the original center of the centrosome marks the origin of the radial speed distribution. The increase in the distance to the origin over 7.5 s was calculated for each tracked particle, resulting in an average speed

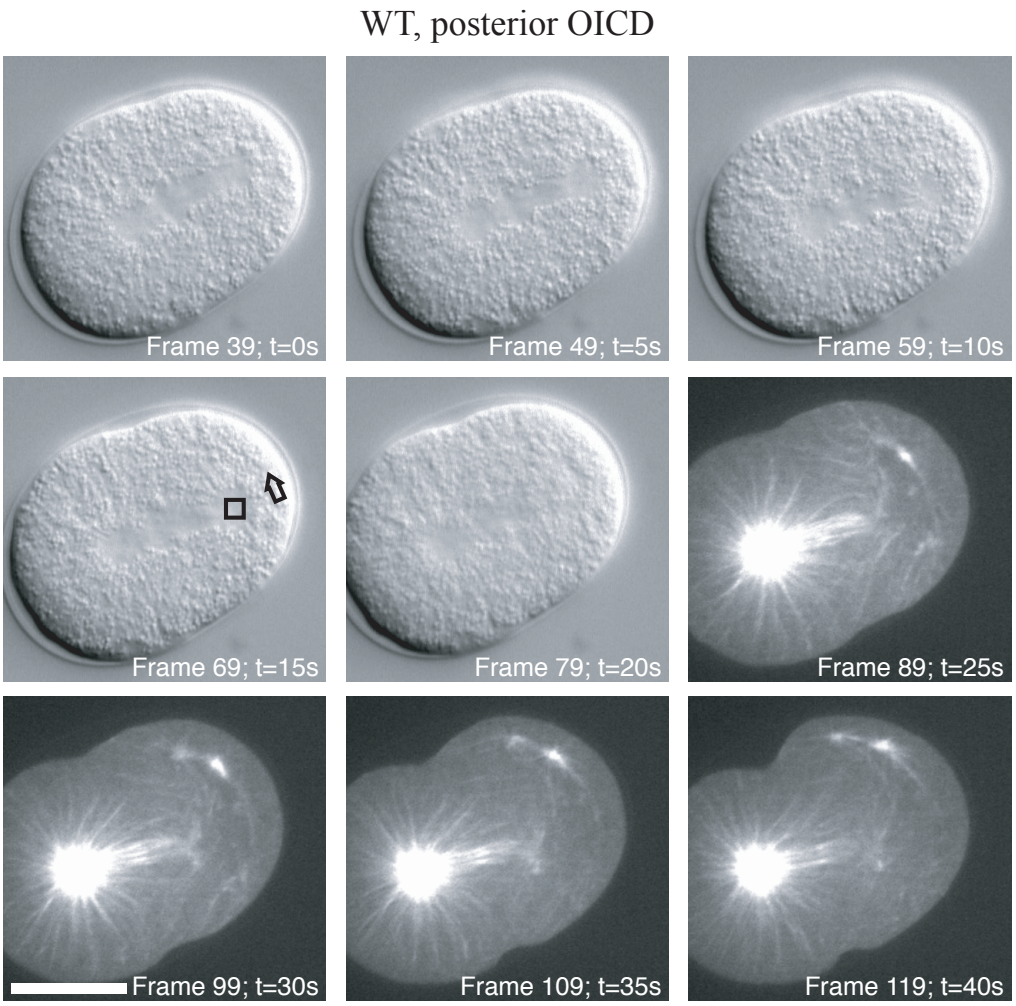

Fig. 2.13 Combined DIC and SDC fluorescence (GFP-tubulin) image series of a posterior centrosome disintegration. OICD is marked by a box. Direction of movement of posterior centrosome prior to OICD is indicated by an arrow. Please refer to the movie "Ch2M11 Post OICD WT.mov" (corresponding frame numbers are indicated). Scale bar: 20 μm.

in radial direction over a time of 7.5 s. Each value was presumed to be a representative value for the speed of yolk granule flow in an angular range of $\pi/36$. Particles travelling in direction of the origin after OICD (e.g. not away from the centrosome, but towards it) were excluded from the analysis. As this method is sensitive to the original center of the centrosome, the center was manually tracked multiple times and averaged. Again it is presumed that any error resulting from imprecise quantification is significantly lower

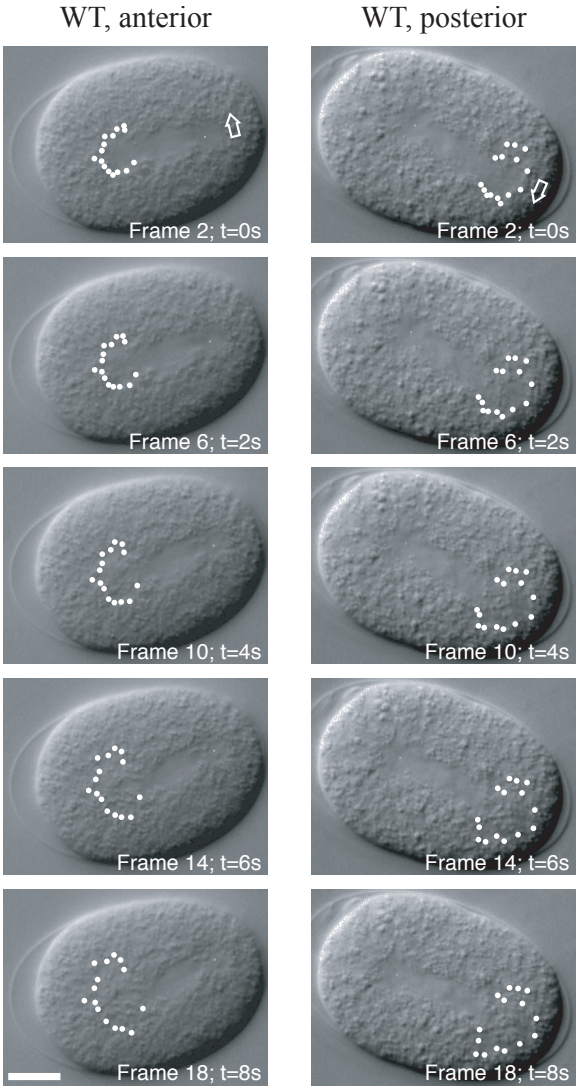

Fig. 2.14 DIC image series of an anterior (WT, anterior) and a posterior (WT, posterior) centrosome disintegration experiment. Yolk granule flow has been tracked and is marked by white dots. The direction of movement of posterior centrosome prior to OICD is indicated by an arrow. Please refer to the movies "CH2M12 A25 OICD WT trkd.mov" and "Ch2M13 P06 OICD WT trkd.mov" (frame numbers are indicated). The corresponding radial speed distributions are plotted in figure 2.15 on page 60 for the anterior (A25) and in figure 2.16 on page 61 for the posterior OICD (P06). Scale bar: 10 μm.

than differences between individual experiments.

Figure 2.15 shows the radial speed distributions for the 32 anterior OICD experiments performed. $\phi = 0$ represents the attachment point of the spindle, $\phi = \pi$ points along the AP axis in direction of the cortex. The posterior centrosome was travelling in the direction of $\phi = \pi/2$ prior to OICD. One can see that there are considerable variations in the distributions from experiment to experiment.

Figure 2.16 shows the radial speed distributions for the 30 posterior OICD experiments performed. Again, $\phi = 0$ represents the attachment point of the spindle and $\phi = \pi$ points in direction of the cortex along the AP axis. The centrosome was travelling in the direction of $\phi = \pi/2$ prior to OICD. Although there are substantial variations in the distributions from experiment to experiment, a bias of flow towards the direction of movement of the posterior spindle pole prior to OICD ($\pi/2$) can be seen in many of the individual distributions.

This bias becomes apparent when the average radial speed distributions of yolk granule flow $\bar{v}(\phi)$ of the anterior an the posterior OICD experiments are compared (figure 2.17). While the distribution for the anterior is symmetric with respect to π, the distribution for the posterior OICD experiments exhibits higher average speeds in the direction of movement of the posterior spindle pole prior to OICD ($\phi = \pi/2$) than in the opposite direction ($\phi = 3\pi/2$). Furthermore, for the anterior centrosome disintegration experiments, granules flowing away from the centrosome at an angle of π (along the AP axis) travel at slightly lower speeds than the granules moving at slightly higher or lower angles, as the radial distribution consists of two peaks separated by a dip at an angle of π.

To rule out the possibility that this apparent asymmetry is an artifact resulting from the averaging process, the amount of asymmetry transverse to the AP axis is determined for each individual OICD experiment and compared. The amount of asymmetry transverse to the AP axis (TA) is computed according to:

$$TA = \left| \frac{\int_0^{2\pi} \sin(\phi)\, v(\phi)\, \mathrm{d}\phi}{\int_0^{2\pi} |\sin(\phi)\, v(\phi)|\, \mathrm{d}\phi} \right|, \tag{2.9}$$

where $v(\phi)$ is the radial distribution of granule speed. TA ranges from 0 (symmetric) to 1 (asymmetric) and is unitless. Figure 2.18 a) lists the values of the transverse asymmetry TA for all OICD experiments performed in the wild-type embryo together with the mean values. One can see that for the anterior OICD experiments, TA is about 30% lower than for the posterior

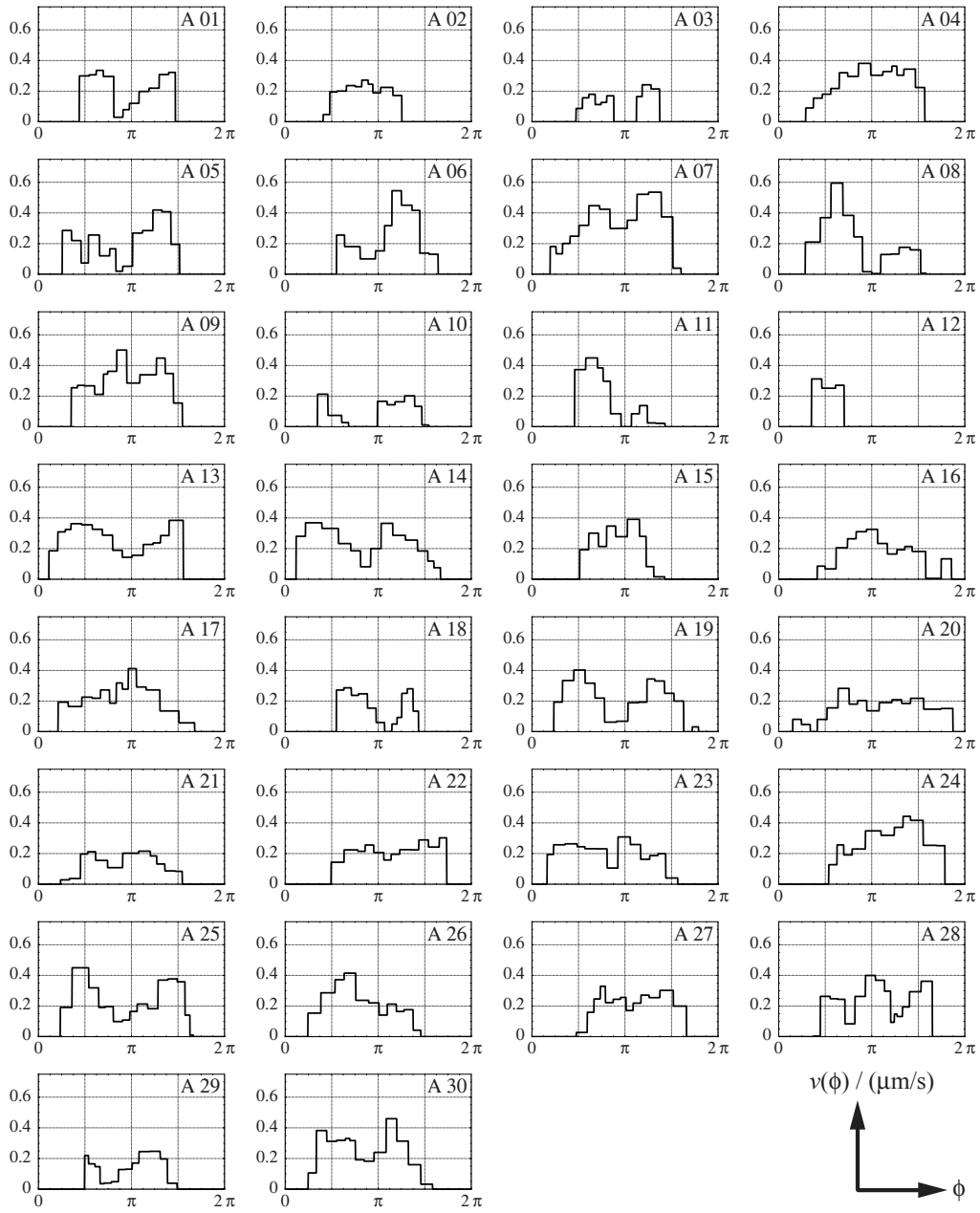

Fig. 2.15 Radial speed distribution $v(\phi)$ of yolk granule flow following 30 OICD experiments of the anterior centrosome in the wild-type embryo. The posterior centrosome was travelling in the direction of $\pi/2$ prior to irradiation. Speed is computed from a displacement over 7.5 s. The error of speed measurement is estimated to be $\pm 5\,\%$.

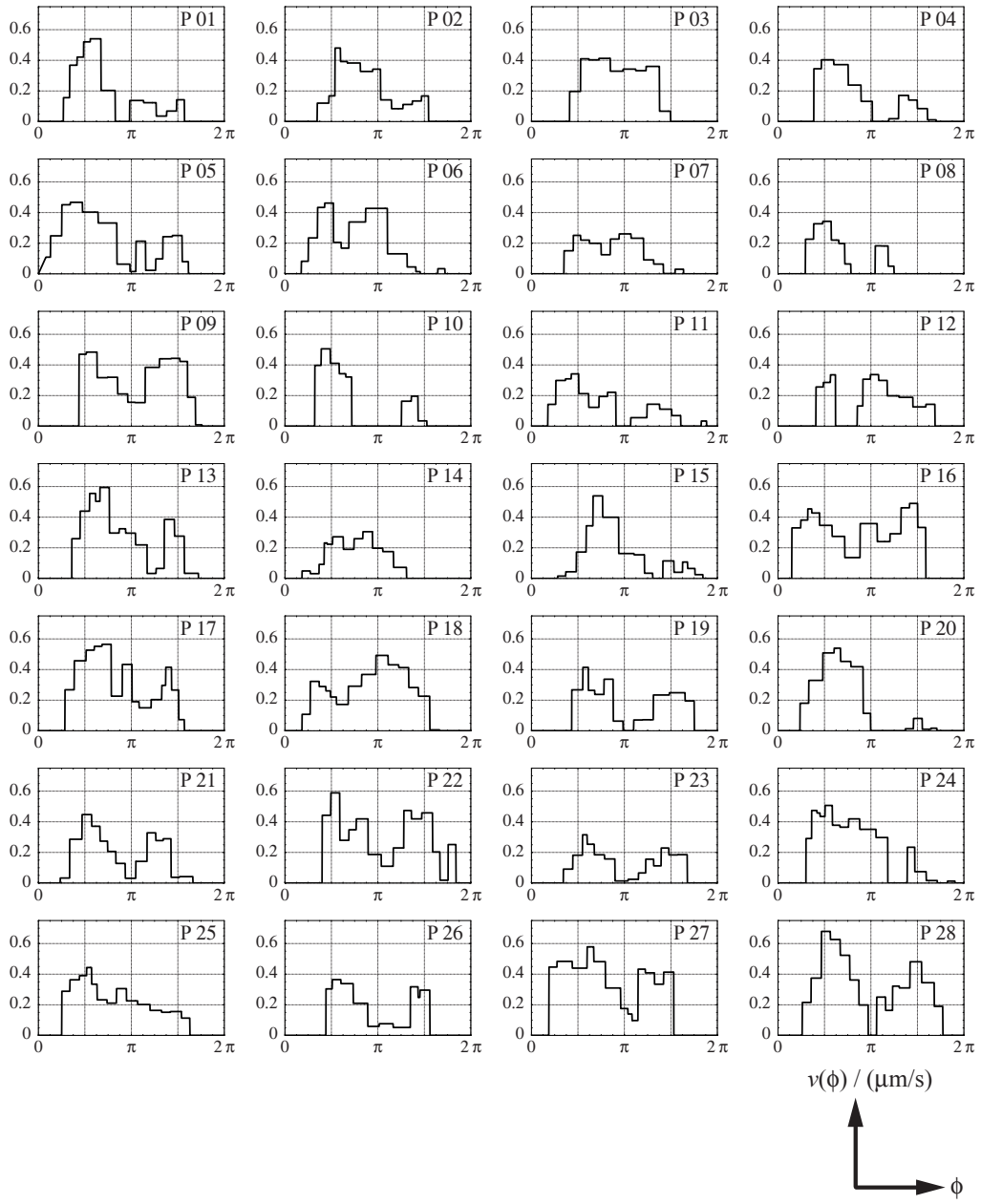

Fig. 2.16 Radial speed distribution $v(\phi)$ of yolk granule flow following 28 OICD experiments of the posterior centrosome in the wild-type embryo. The posterior centrosome was travelling in the direction of $\pi/2$ prior to irradiation. Speed is computed from a displacement over 7.5 s. The error of speed measurement is estimated to be $\pm 5\,\%$.

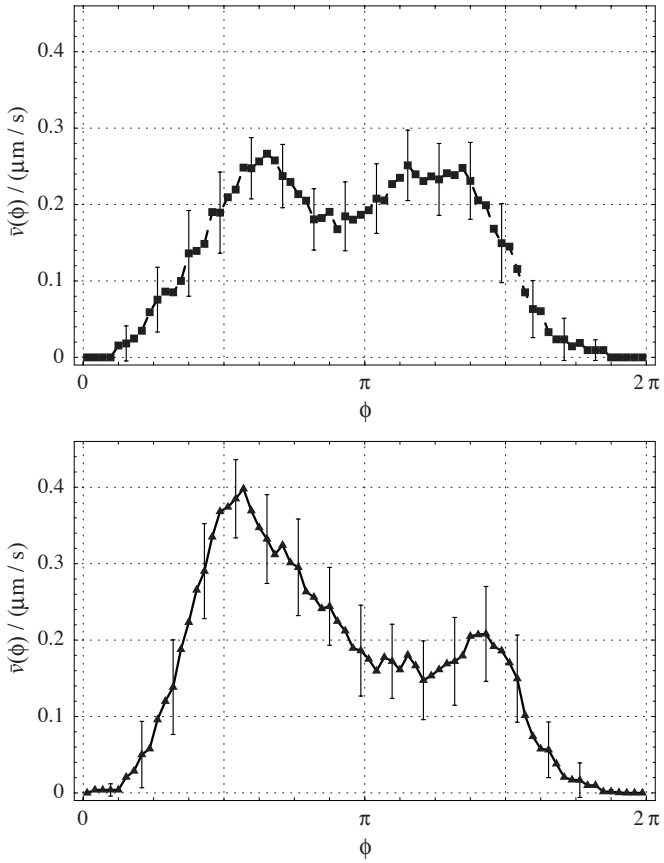

Fig. 2.17 Average radial speed distributions $\bar{v}(\phi)$ of yolk granule flow after OICD experiments in the wild-type embryo. Speed was computed from a displacement over 7.5 s for both the anterior (■, $N = 30$) and the posterior (▲, $N = 28$) centrosome disintegrations. Error bars represent the standard error of mean with a confidence interval of 0.95. For the sake of viewability some error bars are omitted.

a)

	WT	
	A	P
n	TA	TA
01	0.107	0.575
02	0.349	0.334
03	0.065	0.183
04	0.018	0.473
05	0.037	0.427
06	0.344	0.447
07	0.035	0.301
08	0.476	0.684
09	0.052	0.086
10	0.114	0.633
11	0.652	0.424
12	0.675	0.095
13	0.196	0.279
14	0.187	0.473
15	0.214	0.331
16	0.085	0.089
17	0.156	0.335
18	0.19	0.055
19	0.111	0.02
20	0.123	0.737
21	0.115	0.268
22	0.249	0.016
23	0.287	0.048
24	0.382	0.453
25	0.079	0.317
26	0.436	0.186
27	0.246	0.278
28	0.131	0.134
29	0.095	
30	0.231	
	0.215	0.31
	±0.172	±0.205

b)

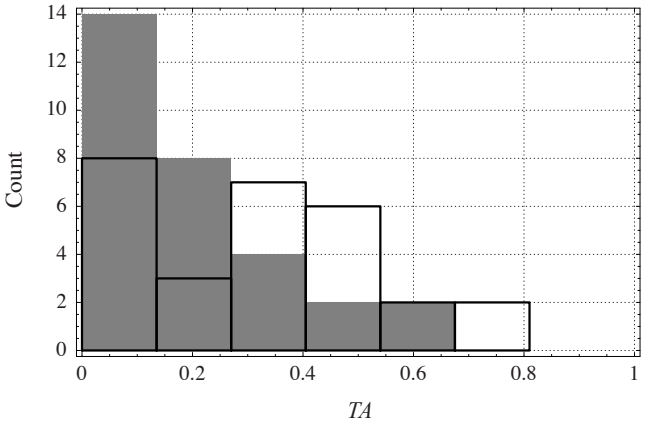

Fig. 2.18 a) Amount of transverse asymmetry (TA) in OICD experiments of the anterior (A, $N = 30$) and the posterior (P, $N = 28$) centrosome. TA is computed according to equation 2.9, ranges from 0 to 1, and is unitless. Bottom row, average values ± standard deviation. b) Corresponding histogram distribution. Anterior shaded in gray, posterior boxed in black. Binning size is 0.135.

OICD experiments. The spread of data, however, is very large, as can be seen in a histogram analysis (figure 2.18). It is concluded that the average transverse asymmetry TA in the radial speed distributions is higher for the posterior OICD experiments than for the anterior OICD experiments.

2.3.2 Centrosome disintegration in *par-2* and *ags-3* (RNAi)

To reveal the function of *ags-3* in the context of spindle positioning, centrosome disintegration experiments were performed in both *par-2* mutant embryos and embryos that have been depleted of AGS-3 by RNAi. In both the *par-2* mutant embryos and the *ags-3* (RNAi) the spindle stays symmetrically positioned throughout anaphase. In *par-2* embryos it has been demonstrated [107] that this is due to a lack of establishment of overall cell polarity. In *ags-3* (RNAi) embryos, however, markers of polarity are correctly distributed (Kelly Colombo, personal communication).

In the *par-2* mutant embryo, OICD of either centrosome leads to an outward flow of yolk granules (figure 2.19), similar to the anterior centrosome disintegration experiment in the wild-type embryo. In the *ags-3* (RNAi) embryos, there is no outward flow of yolk granules following OICD of either centrosome (see figure 2.19). The same UV laser pulse energy was used in all DIC centrosome disintegration experiments.

Table 2.5 shows a list of average velocities $\bar{v}$ of yolk granule flow following OICD as defined by:

$$\bar{v} = \frac{1}{2\pi} \int_0^{2\pi} v(\phi)\, \mathrm{d}\phi, \tag{2.10}$$

where $v(\phi)$ is the radial speed distribution of yolk granule flow. For both *par-2* and wild-type embryos, yolk granules traveled outward at average speeds greater than $0.1\,{}^{\mu\mathrm{m}}/_{\mathrm{s}}$ on average for anterior and posterior OICD experiments. In *ags-3* (RNAi) these speeds are reduced to less than $0.03\,{}^{\mu\mathrm{m}}/_{\mathrm{s}}$.

Furthermore, $\bar{v}$ for posterior centrosome disintegrations in the wild-type embryo is about 17% higher than $\bar{v}$ for anterior centrosome disintegrations in the wild-type embryo.

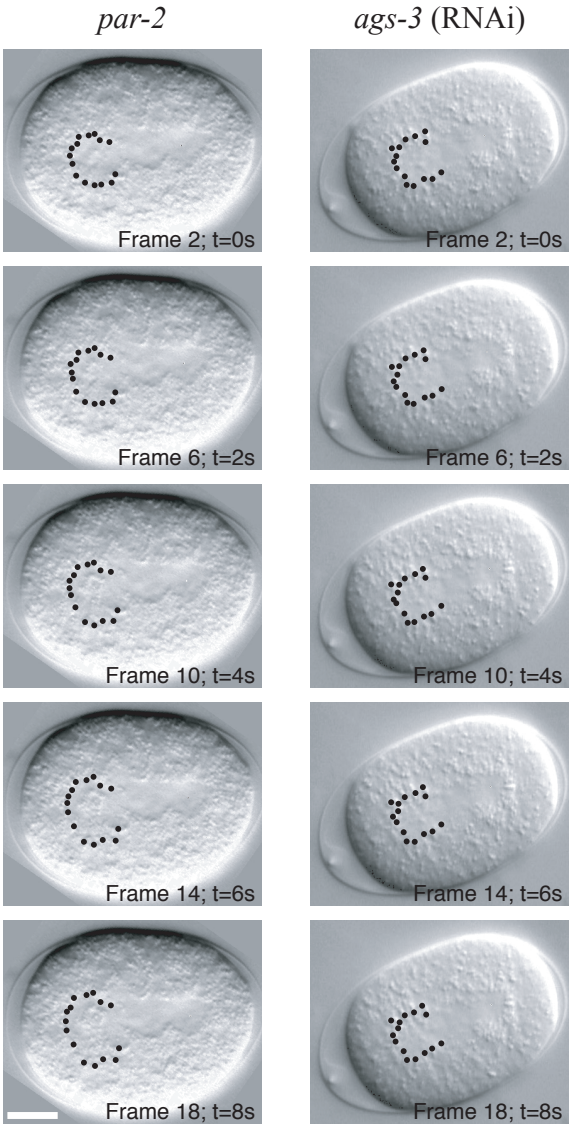

Fig. 2.19 DIC image series of anterior OICD experiments in *par-2* and *ags-3* (RNAi). Yolk granule flow has been tracked and is marked by dots. Please refer to the movies "Ch2M14 Par2 OICD trkd.mov" and "Ch2M15 AGS3 OICD trkd.mov" (corresponding frame numbers are indicated). Scale bar: 10 μm.

	WT		*par-2*		*ags-3* (RNAi)	
	A	P	A	P	A	P
n	$\overline{v}(\mu\mathrm{m}/\mathrm{s})$	$\overline{v}(\mu\mathrm{m}/\mathrm{s})$	$\overline{v}(\mu\mathrm{m}/\mathrm{s})$	$\overline{v}(\mu\mathrm{m}/\mathrm{s})$	$\overline{v}(\mu\mathrm{m}/\mathrm{s})$	$\overline{v}(\mu\mathrm{m}/\mathrm{s})$
01	0.117	0.13	0.055	0.096	0.012	0.01
02	0.085	0.137	0.159	0.171	0.002	0.025
03	0.055	0.171	0.136	0.094	0.018	0.039
04	0.176	0.116	0.145	0.054	0.015	0.045
05	0.139	0.189	0.053	0.138	0.016	0.026
06	0.139	0.167	0.128	0.063		
07	0.237	0.1	0.129	0.102		
08	0.144	0.074	0.064	0.141		
09	0.19	0.211				
10	0.058	0.098				
11	0.091	0.108				
12	0.057	0.117				
13	0.197	0.193				
14	0.193	0.097				
15	0.109	0.126				
16	0.127	0.235				
17	0.156	0.213				
18	0.077	0.212				
19	0.165	0.128				
20	0.135	0.145				
21	0.09	0.142				
22	0.137	0.226				
23	0.146	0.095				
24	0.185	0.184				
25	0.18	0.166				
26	0.139	0.111				
27	0.129	0.26				
28	0.157	0.262				
29	0.072					
30	0.168					
	0.135	0.158	0.109	0.107	0.013	0.029
	$\pm$0.047	$\pm$0.053	$\pm$0.044	$\pm$0.04	$\pm$0.006	$\pm$0.014

Table 2.5 Average velocities $\bar{v}$ of yolk granule flow (equation 2.10) using the radial speed distributions $v(\phi)$ from anterior (A) and posterior (P) OICD experiments in wild-type (anterior: 30, posterior: $N = 28$), *par-2* (it5) ($N = 8$) and *ags-3* (RNAi) ($N = 5$) embryos. Bottom row: average values $\pm$ standard deviation.

3 Model of spindle pole behavior during anaphase

Any model describing spindle pole behavior in the single cell *C. elegans* embryo has to reproduce the following observations (summarized in table 3.1).

1. The posterior spindle pole travels faster and further than the anterior one upon removal of the spindle midzone, and it oscillates transverse to the AP axis as it gets close to the cortex.

2. In late anaphase B, at the time of oscillations, the radial speed distribution of yolk granule flow following OICD of stationary centrosomes is symmetric with respect to π, whereas for moving centrosomes it is asymmetric.

3. In an unperturbed embryo the spindle assumes an eccentric position during anaphase as the posterior spindle pole oscillates transverse to the AP axis (oscillation frequency $\sim 1/25$ Hz).

Every developed model is based on a number of assumptions. These are divided into *biological assumptions*, describing the proposed nature of a biological process, and *descriptive assumptions* necessary for the translation into a mathematical model. The biological assumptions employed here are:

1. Forces acting on spindle poles are generated *at the cortex* and transmitted to the spindle pole via astral microtubules (as proposed by [12, 18]). These forces could result from cortical interactions via dynein and dynactin, microtubule polymerization forces do not play a role as demonstrated by the OICD experiments. Formally, force generation could also be actin-dependent, although this is not likely to be the case, since disruption of actin filaments by cytochalasin during anaphase B does not affect spindle positioning [105, 106].

2. The whole cortex is capable of actively generating force, as yolk granules flow in all directions following OICD experiments.

Experimental results					
A			P		
$\lvert v_{1,x}^{max}\rvert$	$\simeq$	$0.65\,\mu\text{m}/\text{s}$	$\lvert v_{2,x}^{max}\rvert$	$\simeq$	$0.91\,\mu\text{m}/\text{s}$
$d_1(5s)$	$\simeq$	$1.7\,\mu\text{m}$	$d_2(5s)$	$\simeq$	$2.6\,\mu\text{m}$
TA_1	$\simeq$	0.22	TA_2	$\simeq$	0.31
General trends					
$\lvert v_{1,x}^{max}\rvert < \lvert v_{2,x}^{max}\rvert$					
$d_1(5s) < d_2(5s)$					
$TA_1 < TA_2$					
$f \simeq \frac{1}{25}\,\text{Hz}$					

Table 3.1 Summary of experimental results. $i = 1$ refers to the anterior (A) and $i = 2$ to the posterior spindle pole (P). Top: average values of peak velocities $|v_{i,x}^{max}|$ (table 2.1) and the distance travelled $d_i(t) = |\vec{x}_i(t) - \vec{x}_i(0)|$ (figure 2.6) of spindle poles following spindle severing with the UV laser as well as the amount of transverse asymmetry TA_i (figure 2.18) of yolk granule flow following OICD in late anaphase. Bottom: general trends. Non-stationary spindle poles oscillate at frequencies close to f.

3. The distribution of actively pulling connections between the cortex and the microtubules of an aster as a function of time is a sufficient description of the system. Not much is known about the dynamic behavior of microtubules in living *C. elegans* embryos during anaphase. These properties are explicitly ignored.

4. All actively pulling connections of the whole cortex exert the same force on the corresponding spindle pole, independent of position, load and microtubule velocity.

5. The density of *connectors* (a possible point of connection between a microtubule and the cortex) is lower than the density of microtubules reaching the cortex (see figure 1.4 c on page 16). If furthermore the connector density σ is constant over the cortex, the geometry of the cortex alone defines the point of zero net force for spindle poles. Any displacement away from if will result in a restorative force pointing back. This is assumed to be the central mechanism of spindle pole positioning.

6. Spindle poles are mechanically connected by a spindle, which is assumed to elongate upon tension.

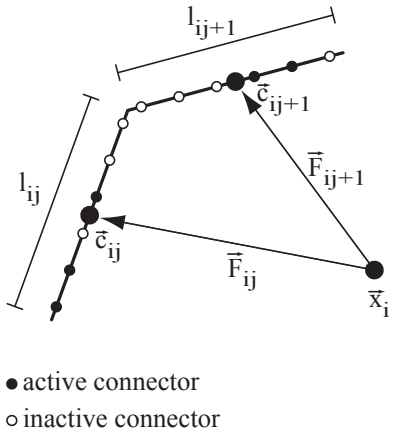

Fig. 3.1 The cortical element j of spindle pole i at the position $\vec{c}_{ij}$ with a length of l_{ij} exerts a force of $\vec{F}_{ij} = \kappa\ N_{ij}(t)\ \frac{\vec{c}_{ij}-\vec{x}_i(t)}{\left|\vec{c}_{ij}-\vec{x}_i(t)\right|}$ on the spindle pole i at $\vec{x}_i$ (equations 3.1 and 3.2). The number of connectors per cortical element is $\sigma\ l_{ij}$. Active and inactive connectors are denoted.

In addition, the following descriptive assumptions needed to be established:

1. A two-dimensional model provides a sufficient first description and is complete with respect to the observations that are to be reproduced.

2. The connection of an astral microtubule to the cortex is called a *connector*. Connectors are *active*, when a microtubule is attached and a force is transmitted to the spindle pole, and *inactive*, when no microtubule is attached and no force is transmitted. They are in either of the two states.

3. The cortex of the embryo is divided into *cortical elements*. The number of connectors in a cortical element is proportional to the length of the cortical element and the linear connector density σ (see figure 3.1). σ is constant for all cortical elements.

4. Connectors switch from the inactive to the active state at the rate r^{on} and from the active to the inactive state at the rate r^{off}. These rates are dependent on the velocity and the position of the spindle pole in such a manner that the *off* rate is decreased by ζ for a particular cortical element when a spindle pole moves towards this element. Therefore, microtubules are less likely to detach from a cortical element if the spindle pole is moving towards it.

5. Polarity controls the *on* and *off* rates and their dependency on the velocity and the position of the spindle pole in a manner compatible with the distribution of markers of polarity such as PAR-2 and PAR-3. All cortical elements in each section of the embryo will behave in the same way.

6. Cortical elements in the anterior section of the embryo exert forces on the anterior spindle pole, cortical elements in the posterior half of the embryo exert forces on the posterior spindle pole. The force exerted by a cortical element is proportional to the number of active connectors in that element.

7. Spindle poles move in a viscous medium according to the sum of all forces acting on them. Forces generated from inertia are ignored, the mass of a spindle pole is set to zero.

Microtubules can be visualized in *C. elegans* embryos using transgenic GFP-tubulin lines [142], therefore the rates of attachment to and detachment from the cortex should become measurable quantities in the near future. The model presented predicts the movement of spindle poles resulting from the *on* and *off* rates and their variation with position and velocity of spindle poles.

3.1 Set of differential equations

The following forces act on a spindle pole (see equations 3.1):

1. A frictional force $\vec{F}_F$ proportional to the speed of the spindle pole.

2. A force $\vec{F}_{SC}$ resulting from a spindle constraint, as there is a mechanical connection between the spindle poles.

3. A net cortical force $\vec{F}_i$.

The following set of inseparable differential equations is compatible with the above assumptions. Only explicit dependencies on time are denoted:

$$
\begin{aligned}
0 &= -\overbrace{\beta\ \partial_t \vec{x}_1(t)}^{\vec{F}_F} + \overbrace{\beta_s\ \frac{\vec{x}_2(t)-\vec{x}_1(t)}{\left|\vec{x}_2(t)-\vec{x}_1(t)\right|}\ \partial_t\left|\vec{x}_2(t)-\vec{x}_1(t)\right|}^{\vec{F}_{SC}} + \vec{F}_1 \\
0 &= -\beta\ \partial_t \vec{x}_2(t) - \beta_s\ \frac{\vec{x}_2(t)-\vec{x}_1(t)}{\left|\vec{x}_2(t)-\vec{x}_1(t)\right|}\ \partial_t\left|\vec{x}_2(t)-\vec{x}_1(t)\right| + \vec{F}_2, \\
&\textit{where}\quad \vec{F}_i = \sum_{j=1}^{j_{max}} \kappa\ N_{ij}(t)\ \frac{\vec{c}_{ij}-\vec{x}_i(t)}{\left|\vec{c}_{ij}-\vec{x}_i(t)\right|}; \qquad (3.1)
\end{aligned}
$$

$$
\begin{aligned}
\partial_t N_{ij}(t) &= \big(\sigma\ l_{ij} - N_{ij}(t)\big) R_{ij}^{on} - N_{ij}(t) R_{ij}^{off}, \\
&\textit{where}\quad R_{ij}^{on} = r^{on} \\
&\qquad\quad R_{ij}^{off} = r^{off}\ \left(1 - \zeta_i(t)\ \Theta\Big(\big(\vec{c}_{ij}-\vec{x}_i(t)\big)\cdot \partial_t \vec{x}_i(t)\Big)\right). \qquad (3.2)
\end{aligned}
$$

As there are two mechanically connected spindle poles, equations 3.1 and 3.2 are a set of $2j_{max}+4$ inseparable differential equations: $\vec{x}_1(t)$ and $\vec{x}_2(t)$ represent the center positions of the anterior and posterior spindle pole, respectively; and the $2j_{max}$ functions $N_{ij}(t)$ describe the number of active connectors in each cortical elements as a function of time.

See figure 3.1 for a graphical description of some of the variables used. i denotes the spindle poles, $i = 1$ represents the anterior and $i = 2$ the posterior spindle pole. j_{max} is the number of cortical elements associated with each pole. β is the friction coefficient for the movement of a spindle pole in viscous medium. β_s represents the friction constant of spindle elongation. $\vec{c}_{ij}$ describes the position and l_{ij} the length of cortical element j of spindle pole i. R_{ij}^{on} is the rate at which connectors of cortical element j of spindle pole i switches from inactive to active. R_{ij}^{off} is the corresponding *off* rate. r^{on} and r^{off} are the basic *on* and *off* rates. σ is the linear connector density, $\sigma\ l_{ij}$ the total number of connectors for a particular cortical element. κ is the force exerted by a cortical element with a length l_{ij} of 1 μm in the case of all connectors being active. Θ is the Heavyside-function. $\zeta_i(t)$ describes the dependency of the *off* rates on the position and speed of spindle pole i. It is unitless, ranges from 0 (no dependency) to 1 (fully dependent) and may be a function of time. In particular, ζ_i is different for the anterior ($i = 1$) and

the posterior ($i = 2$) cortical elements.

$\vec{F}_{SC}$ results from a rigid body constraint corresponding to a mechanical connection which elongates under tension. $\vec{F}_{SC}$ is proportional to the rate of increase of spindle length $\partial_t \left| \vec{x}_2(t) - \vec{x}_1(t) \right|$ and is pointing in the direction of the other spindle pole. β_s is the corresponding friction coefficient.

$N_{ij}(t)$ describes the number of active connectors in each cortical element as a function of time. Cortical element j exerts a force proportional to the number of its active connectors N_{ij} in direction of the element j on the spindle pole i. The net cortical force $\vec{F}_i$ is the sum of all these forces.

The total number of active connectors N_{ij} in each cortical element varies according to a rate equation (equation 3.2, first line). All *on* rates R_{ij}^{on} of all elements are equal to r^{on}. However, *off* rates R_{ij}^{off} are dependent on the position and velocity of the corresponding spindle pole (equation 3.2). R_{ij}^{off} is equal to r^{off} when the spindle pole moves away from that particular cortical element. If the spindle pole moves towards it, R_{ij}^{off} is lowered to $(1 - \zeta_i) r_{ij}^{off}$. Therefore, ζ_i describes the amount of dependency of R_{ij}^{off} on the position and velocity of the spindle pole i. The ζ_i are also referred to as the *regulators of oscillatory motion.*

Increasing the *on* rate rather when a spindle pole moves towards a particular cortical element rather than decreasing the *off* rate results in a new set of differential equations, which, however, lead to very similar solutions once solved.

The $2j_{max} + 4$ inseparable differential equations cannot be solved in an analytical manner. To find an approximative solution for a particular set of variables, an iterative numerical approach was chosen. For small time steps Δt this will converge against the true solution. Convergence was checked for simplifications allowing for analytical solutions. As a starting condition, the initial speeds of the spindle poles are set to zero.

3.1.1 Circular geometry

Two spindle poles are placed in their own cortex of circular geometry (the radius is $16\,\mu$m).

β is set to a value allowing a force of 4 pN to move a spindle pole at a speed of $1\,{}^{\mu\mathrm{m}}/_{\mathrm{s}}$. r^{on} and r^{off} are set to values such that 33% of the connectors in each cortical element are active at steady state. σ and κ are set to values such that a cortex of $1\,\mu$m length exerts a force of 0.05 pN on average at steady state. This results in the following settings: $j_{max} = 20$, $\beta = 0.25\,{}^{\mu\mathrm{g}}/_{\mathrm{s}}$, $\beta_s = 0\,{}^{\mu\mathrm{g}}/_{\mathrm{s}}$, $\sigma = 0.15\,\mu\mathrm{m}^{-1}$, $\kappa = 1\,\mathrm{pN}$, $r^{on} = 0.2$, $r^{off} = 0.2$, $\zeta_1 = 0.05$ and $\zeta_2 = 1$.

The *off* rates of cortical elements of the anterior spindle pole are not

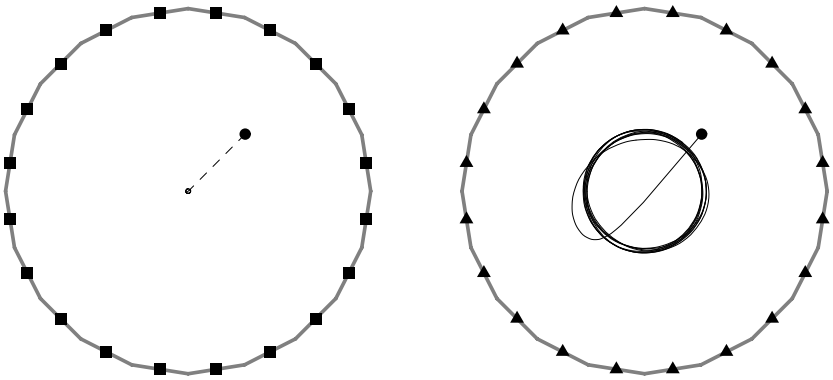

Fig. 3.2 Spindle pole positions in a circular geometry. Parametric plots of the numerical solution to equations 3.1 and 3.2 are displayed, where $j_{max} = 20$, $\beta = 0.25\,\mu\text{g/s}$, $\beta_s = 0\,\mu\text{g/s}$, $\sigma = 0.15\,\mu\text{m}^{-1}$, $\kappa = 1\,\text{pN}$, $r^{on} = 0.2$, $r^{off} = 0.2$, $\zeta_1 = 0.05$ and $\zeta_2 = 1$. Cortex consisting of cortical elements with anterior properties (■) on the left, cortex consisting of cortical elements with posterior properties (▲) on the right. Disks denote spindle pole center positions at $t = 0\,\text{s}$. Please refer to the movie "Ch3M01 CircularGeo.mov".

significantly dependent on the position and velocity of the anterior spindle pole, whereas on the posterior side the *off* rates are completely dependent on the position and velocity of the posterior spindle pole. Figure 3.2 shows parametric plots of the numerical solution of equations 3.1 and 3.2. Following an initial displacement (discs at $t = 0\,\text{s}$), the anterior cortex allows for the centering of the spindle pole, whereas the posterior spindle pole propagates in an oscillatory mode. This demonstrates that the generation of oscillatory motion in equations 3.1 and 3.2 is under control of the ζ_i.

3.1.2 Removing the spindle midzone

Two spindle poles are placed in an embryo-like geometry $51.5\,\mu\text{m}$ long and $32\,\mu\text{m}$ wide. The cortex is parametrisized using two half-circles with a radius of $16\,\mu\text{m}$ a distance of $18\,\mu\text{m}$ apart. The exact shape of the cortex should not have a great impact as it varies from embryo to embryo. Similar to the distribution of markers of polarity (PAR-2 and PAR-3) in the wild-type embryo, the cortex is half of anterior character and half of posterior character. At $t = 0\,\text{s}$ the connecting spindle structure is removed. This scenario is analogous to the experiments performed in section 2.2 on page 39.

Except for the cortical geometry, the constants in equations 3.1 and 3.2 are set to the same values as for the circular geometry. In particular, $\zeta_1 = 0.05$ and $\zeta_2 = 1$. Figure 3.3 a) shows parametric plots of the numerical solution

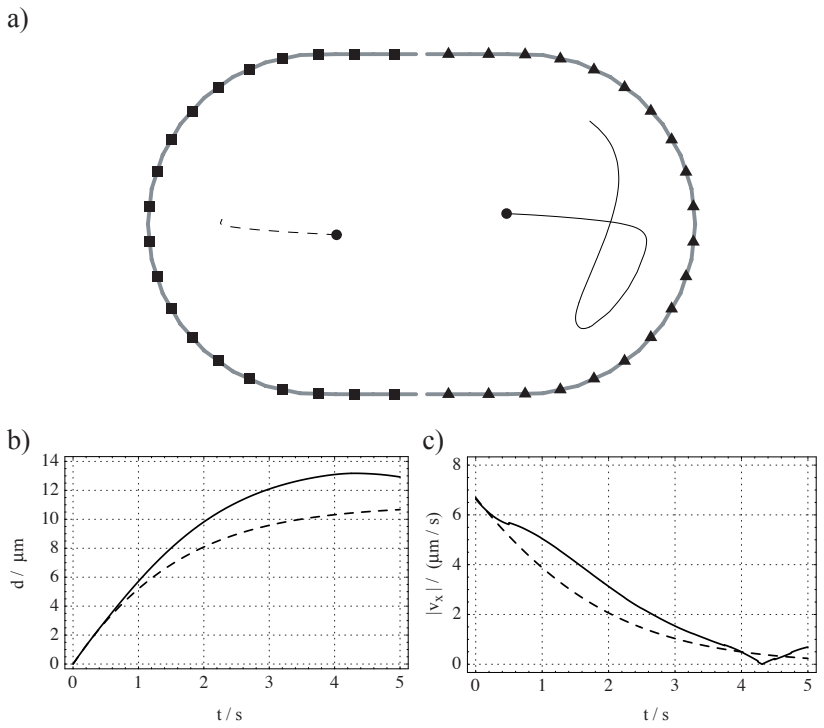

Fig. 3.3 Simulation of a spindle cut. The numerical solution to equations 3.1 and 3.2 is displayed, where $j_{max} = 20$, $\beta = 0.25\,\mu$g/s, $\beta_s = 0\,\mu$g/s, $\sigma = 0.15\,\mu\text{m}^{-1}$, $\kappa = 1\,\text{pN}$, $r^{on} = 0.2$, $r^{off} = 0.2$, $\zeta_1 = 0.05$ and $\zeta_2 = 1$. $t = 0$ corresponds to the time of spindle severing. a) Parametric plot of spindle pole positions. Cortex with anterior-type cortical elements (■) on the left, cortex with posterior-type cortical elements (▲) on the right. Spindle pole positions at $t = 0\,\text{s}$ are indicated by discs. Please refer to the movie "Ch3M02 SpCut.mov". b) Displacement $d(t) = |\vec{x}_i(t) - \vec{x}_i(0)|$ of the anterior (dashed) and the posterior spindle pole (solid) as a function of time. Actual movements are in opposite directions. c) $|v_x(t)|$ of the anterior (dashed) and the posterior (solid) spindle pole.

of equations 3.1 and 3.2. Figure 3.3 b) shows the distance travelled of both spindle poles following the removal of the spindle midzone. The posterior spindle pole travels further than the anterior one. This should be compared to figure 2.6 c) on page 43. Figure 3.3 c) shows $|v_x(t)|$ for both spindle poles. It is demonstrated that the posterior spindle pole travels faster than the anterior one.

3.1.3 Anaphase in the unperturbed embryo

Two spindle poles are placed in the embryo-like geometry described above. However, the spindle midzone is now kept in place while the regulator of

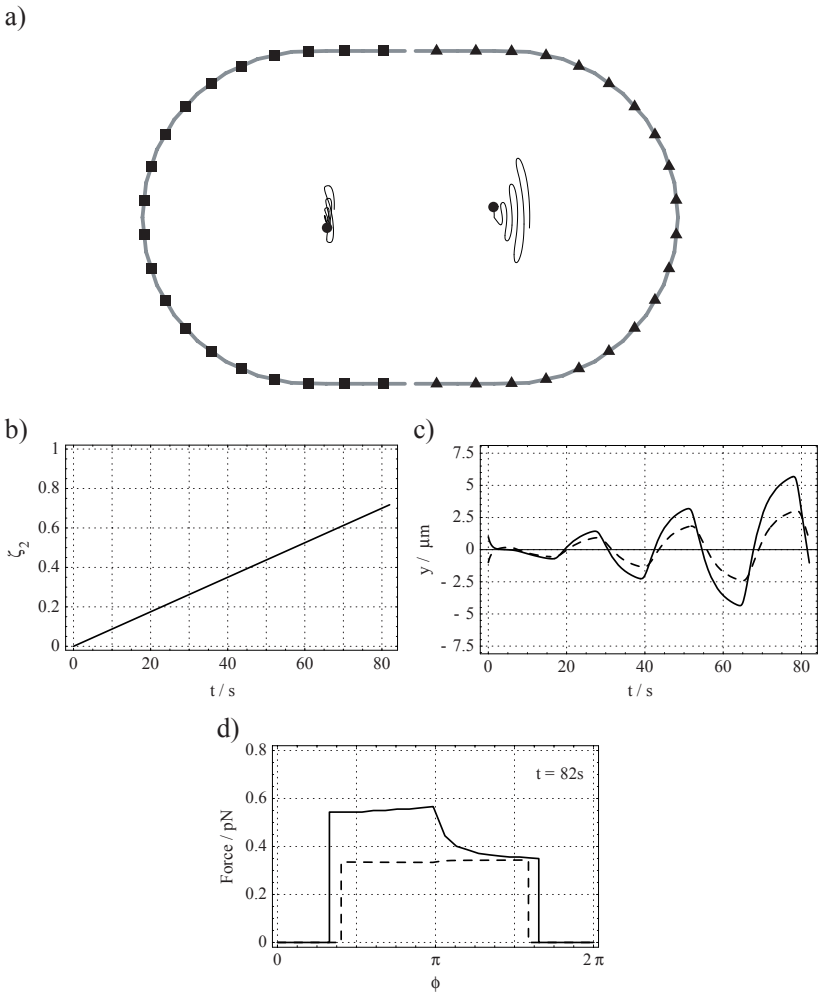

Fig. 3.4 Simulation of anaphase. The numerical solution of equations 3.1 and 3.2 is displayed, where $j_{max} = 20$, $\beta = 0.25\,\mu\text{g/s}$, $\beta_s = 50\,\mu\text{g/s}$, $\sigma = 0.15\,\mu\text{m}^{-1}$, $\kappa = 1\,\text{pN}$, $r^{on} = 0.2$, $r^{off} = 0.2$, $\zeta_1 = 0.05$ and $\zeta_2 = 8.75 \times 10^{-3}\ t$. a) Parametric plot of spindle pole positions during anaphase with a connecting spindle present. Cortex with anterior-type cortical elements (■) on the left, cortex with posterior-type cortical elements (▲) on the right. Spindle pole positions at $t = 0\,\text{s}$ are indicated by discs. Please refer to the movie "Ch3M03 Anaphase.mov". b) The regulator of oscillatory motion ζ_2 for the posterior spindle pole as a function of time. A linear increase from 0 to 0.7 within 80 s leads to the behavior presented in a). c) y coordinate of the anterior (dashed) and the posterior spindle pole (solid) as a function of time. d) Radial distribution of cortical forces F_i acting on the anterior (dashed) and the posterior spindle pole (solid) at $t = 82\,\text{s}$. Please refer to the movie "CH3M04 Anaphase RDF.mov".

Results from numerical simulation

A			P		
$\lvert v_{1,x}(2.5s)\rvert$	$\simeq$	$1.5\,\mu\mathrm{m}/\mathrm{s}$	$\lvert v_{2,x}(2.5s)\rvert$	$\simeq$	$2.2\,\mu\mathrm{m}/\mathrm{s}$
$d_1(5s)$	$\simeq$	$10.7\,\mu\mathrm{m}$	$d_2(5s)$	$\simeq$	$12.9\,\mu\mathrm{m}$
TA_1	$\simeq$	0.002	TA_2	$\simeq$	0.156

General trends

$$\lvert v_{1,x}(2.5s)\rvert < \lvert v_{2,x}(2.5s)\rvert$$
$$d_1(5s) < d_2(5s)$$
$$TA_1 < TA_2$$
$$f \simeq \tfrac{1}{25}\,\mathrm{Hz}$$

Table 3.2 Summary of results obtained from numerical simulation. $i = 1$ refers to the anterior (A) and $i = 2$ to the posterior spindle pole (P). Top, average values of velocities $|v_{i,x}(t)|$ and the distance travelled $d_i(t) = |\vec{x}_i(t) - \vec{x}_i(0)|$ over t seconds after removal of the spindle (see figure 3.3) as well as the amount of transverse asymmetry $TA_i = \left| \int_0^{2\pi} \sin(\phi)\, F_i(\phi)\, \mathrm{d}\phi \,/\, \int_0^{2\pi} |\sin(\phi)\, F_i(\phi)|\, \mathrm{d}\phi \right|$ of cortical forces F_i acting on spindle pole i at $t = 82\,\mathrm{s}$ in the unperturbed embryo (figure 3.4). Bottom, general trends. The non-stationary posterior spindle pole oscillates at a frequency close to f (figure 3.4). This table is to be compared to the experimental results (table 3.1).

oscillatory motion ζ_2 (for the posterior cortex) is increased in a linear manner from 0 to 0.7 within 80 s. This scenario corresponds to an unperturbed wild-type embryo undergoing anaphase spindle elongation. β_s is set to a value such that a force of 10 pN pulling on both spindle pole results in a $5\,\mu$m increase of spindle length over about 25 s.

The other constants in equations 3.1 and 3.2 are set to the same values as for the circular geometry, except for $\beta_s = 50\,\mu\mathrm{g}/\mathrm{s}$ and $\zeta_2(t) = 8.75 \times 10^{-3}\ t$. Figure 3.4 a) shows the corresponding parametric plot of the numerical solution of equations 3.1 and 3.2. One can see that the spindle elongates in direction of the posterior cortex: the anterior spindle pole stays about where it is, whereas the posterior spindle pole is displaced while oscillating transversely. Figure 3.4 b) shows a plot of the function $\zeta_2(t)$. Figure 3.4 c) is a plot of the transverse (y) coordinate of both spindle poles as a function of time, demonstrating an increase of oscillation amplitude with time. The oscillation frequency is in the order of 1/25 Hz. Figure 3.4 d) displays the radial force distribution acting on both spindle poles at t =82 s. At this time the posterior spindle pole is travelling downwards across the AP axis. This graph is to be compared with figure 2.17 on page 62, although caution has to be taken in the comparison as the properties plotted are different in

the two graphs. However, in both cases the distributions for the posterior spindle pole display an asymmetry towards the direction of movement of the posterior spindle pole ($\pi/2$).

Table 3.2 summarizes the results obtained from the numerical simulations. Rather than displaying peak velocities following spindle removal, as they are identical for the anterior and the posterior spindle pole in the numerical simulation due to the instantaneous removal of the spindle, $|v_x(t)|$ for $t = 2.5\,\mathrm{s}$ is displayed. This table has to be compared to the experimental results (table 3.1). The velocities and the distances travelled after spindle removal differ between the numerical simulation and the experimental results. Also the amounts of transverse asymmetry TA in the radial distribution of speeds of yolk granule flow after OICD fails to agree with the amount of transverse asymmetry in the force distribution acting on each spindle pole in the numerical simulation. However, the general trends are identical, and the oscillation frequency for non-stationary spindle poles is reproduced in the numerical simulation.

In summary, the set of differential equations 3.1 and 3.2 are capable of reproducing the general behavior of spindle poles in the wild-type embryo.

4 Discussion

The technique of rigid body constraint removal was applied to test for the presence of tensile stress both within the spindle structure and the individual microtubule asters of the one cell stage *C. elegans* embryo. Furthermore, the average diffusion coefficients of yolk granules located close to the anterior and close to the posterior cell cortex were determined separately. The experimental results were applied to generate a phenomenological model, which is able to reproduce essential features of anaphase spindle positioning.

Diffusive properties of yolk granules are similar at the anterior and at the posterior of the embryo

A MSD analysis of yolk granule diffusion for 92 granules located close to the anterior cell cortex and 90 granules located close to the posterior cell cortex of the one cell stage *C. elegans* embryo results in diffusion coefficients that are not significantly different (section 2.1). For yolk granules at the anterior D_A is measured to be $(3.3 \pm 1.4) \times 10^{-3}\,\mu\mathrm{m}^2/\mathrm{s}$, for yolk granules at the posterior the MSD analysis supplies a value of $D_P = (2.9 \pm 1.2) \times 10^{-3}\,\mu\mathrm{m}^2/\mathrm{s}$ (figure 2.3). Yolk granules have a diameter of $0.84 \pm 0.12\,\mu\mathrm{m}$, as determined optically for granules throughout the cytoplasm. There is no statistically significant difference of yolk granule diameters at the anterior compared to the posterior.

By applying the Einstein relation (equation 1.7 on page 29, $T = 296\,\mathrm{K}$), an estimate for the cytoplasmic viscosity is calculated, providing a value for the dynamic viscosity of $\eta = (0.11 \pm 0.05)\,\mathrm{Pa\,s}$. This estimate of the cytoplasmic viscosity is only valid for objects with a diameter below $1\,\mu\mathrm{m}$ not deforming the cytoskeletal network as they move, as yolk granules are not expected to deform the cytoskeleton while they undergo Brownian motion.

It is possible to estimate a lower limit for the force required to move a spindle pole through the cytoplasm at a speed of $1\,\mu\mathrm{m}/\mathrm{s}$. Assuming that the anterior and the posterior spindle poles are of similar size (figure 2.4 a on page 40), the viscous drag acting on a spindle pole is estimated by substituting a sphere with a hydrodynamic radius of $R_H = 5\,\mu\mathrm{m}$. Stoke's law ($\vec{F} = -6\,\pi\,\eta\,R_H\,\vec{v}$) then provides a lower limit for the force required to move

a spindle pole through the cytoplasm of the embryo at $v = 1\,\mu\text{m}/\text{s}$, which computes to about 10 pN.

In conclusion, the diffusive properties of yolk granules are not significantly different at the anterior and at the posterior of the embryo, supporting the possibility that the viscoelastic properties of the cytoplasm are isotropic and independent of overall cell polarity. The calculation of an effective cytoplasmic viscosity valid for objects not deforming the cytoplasm with a diameter below $1\,\mu$m enables the estimation of the minimal force required to move a spindle pole at the speeds observed (about 10 pN). As one single kinesin molecule is capable of generating up to 8 pN of force, it is possible that only a few motor proteins are involved in moving a spindle pole at the speeds observed.

The spindle is under tensile stress

To investigate the net active force acting on each spindle pole of the asymmetrically dividing one cell stage *C. elegans* embryo and to test for the presence of tensile stress within the spindle, the spindle midzone was removed in living *C. elegans* embryos (section 2.2). Spindle poles rapidly move apart from one another (figure 2.5 on page 41) after physical perturbation with a UV laser at the time of anaphase (figure 2.4 on page 40). Furthermore, silencing the expression of *CeMCAK* by RNAi also results in a diminished spindle midzone (figure 2.4 on page 40). Spindle poles again rapidly move apart from one another at late anaphase. Following UV laser irradiation, both spindle poles travel outwards at peak velocities that are increased three-fold when compared to unperturbed wild-type embryos (summarized in figure 4.1).

It can be immediately concluded that tensile stress is present within the spindle at the beginning of anaphase B. As both spindle poles move, there are active forces acting on *both* of the spindle poles, in contrast to the proposed mechanism of asymmetric spindle position depicted in figure 1.5 d (page 18). There is no further rigid body constraint keeping the distance of the anterior spindle pole to the anterior cortex constant.

Most interestingly, the two spindle poles behave differently after spindle severing: the posterior spindle pole travels both faster (figure 4.1) and further than the anterior spindle pole, and it undergoes transverse oscillations in proximity to the cell cortex. From this result it is concluded that the dynamic properties responsible for spindle pole positioning are different for the two spindle poles. The anterior spindle pole is capable of centering itself further away from the cell cortex, whereas the posterior spindle pole establishes a position closer to the cortex while propagating in an oscillatory mode. Furthermore, as viscoelastic properties are presumed to be uniform

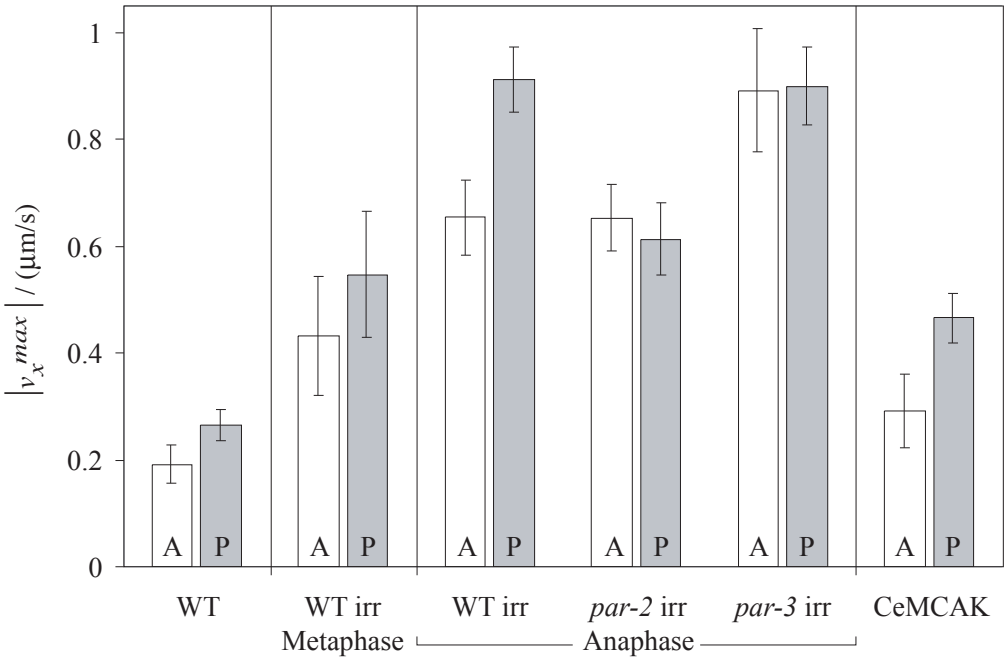

Fig. 4.1 Summary chart of peak velocities $|v_x^{max}|$ of anterior (A) and posterior (P) spindle poles of untreated wild-type embryos throughout metaphase and anaphase (WT, $N = 20$), wild-type embryos irradiated at the time of metaphase (WT irr, $N = 14$), wild-type embryos irradiated at anaphase (WT irr, $N = 34$), *par-2* embryos irradiated at anaphase (*par-2* irr, $N = 30$), *par-3* embryos irradiated at anaphase (*par-3* irr, $N = 20$) and *CeMCAK* (RNAi) (CeMCAK, $N = 20$) embryos. Error bars represent the standard error of mean with a confidence interval of 0.95. See tables 2.1, 2.2, and 2.3.

throughout the cytoplasm (section 2.1) and since the posterior spindle pole travels faster than the anterior one, a greater net force must be acting on the posterior spindle pole than on its anterior counterpart after spindle severing.

The spindle midzone acts as a limiter during spindle elongation, determining pole-to-pole distance. It is not possible for the spindle midzone to build up mechanical tension in embryos lacking important kinetochore components, resulting in a premature elongation of the spindle [142]. In *CeMCAK* (RNAi) embryos, pole-to-pole distance suddenly increases as the spindle breaks apart at the time of late anaphase B (section 2.2). However, spindle poles do not travel at velocities that are as high as the speeds observed for spindle poles after UV laser irradiation, probably because the spindle breaks apart 20 to 30 s later compared to the time the UV laser spindle severing experiments were performed. There are two explanations for the *CeMCAK* (RNAi) phenotype: either the spindle midzone is mechanically destabilized, or the forces pulling on the spindle are increased, resulting in

spindle rupture. CeMCAK has been demonstrated to localize to centrosomes and kinetochores in *C. elegans* embryos [142], therefore it could be possible that it participates in maintaining a mechanically stable spindle midzone. The exact function of CeMCAK in the context of anaphase spindle positioning remains to be determined.

Tensile stress is also present within the spindle during metaphase, as demonstrated by spindle severing at the time of metaphase. However, the two spindle poles move apart at slower speeds relative to when the spindle is severed during anaphase (figure 4.1). As spindle pole sizes do not increase significantly from metaphase to anaphase, it is concluded that there is less tensile stress present within the spindle at metaphase than at anaphase.

Cell polarity controls the net active force exerted on each spindle pole

To address the question of how cell polarity influences the net active force exerted on each spindle pole, spindle severing experiments were performed in *par-2* and *par-3* mutant embryos (section 2.2.3). In both of these mutant embryos the spindle is symmetrically positioned throughout anaphase B. In wild-type, PAR-3 is restricted to the anterior cortex and PAR-2 to the posterior cortex. In *par-2* mutants, PAR-3 is found both at the posterior and anterior cortex of the embryo, leading to a cortex which has anterior character throughout. Conversely, in *par-3* mutant embryos, PAR-2 fills the entire cortex of the embryo, which thus has posterior character throughout.

The spindle midzone was severed at anaphase with a UV laser. Interestingly, in severed *par-2* mutant embryos, the resulting peak velocities of both spindle poles resembled that of the anterior spindle pole in wild-type irradiated embryos (figure 4.1). Conversely, in severed *par-3* mutant embryos, peak velocities of both spindle poles resembled that of the posterior spindle pole in wild-type irradiated embryos (figure 4.1). Furthermore, spindle breakage events still occurred when both PAR-3 and CeMCAK were removed, while none were observed when abolishing the expression of both PAR-2 and CeMCAK by RNAi. This indicates that the tensile stress present within the spindle in the absence of *par-2* function is not large enough to trigger spindle rupture, whereas the tensile stress is increased for *par-3* mutant embryos, resulting in the breakage of the spindle in 36% of the embryos observed.

Taken together, these observations imply that the first division in *par-2* and *par-3* mutant embryos is symmetric because the dynamic properties of the force generating interactions between astral microtubules and the cell cortex are identical on both sides, leading to equal net active forces being exerted on each spindle pole (section 2.2.3), resulting in a symmetric spindle position at the end of anaphase.

As a control experiment, centrosome disintegration (CD) experiments were performed for each of the spindle poles, and the trajectory of the remaining spindle pole was determined (section 2.2.4). As this is another method of breaking the connection between the two spindle poles, spindle pole behavior should be similar to when performing spindle severing experiments. As documented in figure 2.10 and table 2.4 (on pages 51 and 52), disintegration of either centrosome qualitatively confirms the results obtained by performing spindle severing experiments. In general, the absolute peak velocities are reduced, probably due to inefficient disintegration (the PALM setup was used for these experiments).

In summary, the spindle is under tensile stress at the time of anaphase. The net active force exerted on each spindle pole is under the control of overall cell polarity and increases from metaphase to anaphase.

Forces are generated all over the cortex

It is an interesting possibility that the generation of oscillations is linked to the establishment of a larger net active force, as a cortex of posterior character generates both oscillations and a larger net active force. To address this question it is important to know whether confined cortical force generation or global cortical force generation is responsible for spindle pole positioning. To distinguish between these two possibilities and to study the phenomenon of transverse oscillations by testing for the presence of tensile stress within a microtubule aster, OICD experiments were performed at anaphase both with the stationary anterior and the oscillatory posterior centrosome (section 2.3).

Upon disintegration of either centrosome in a fluorescence assay, centrosomal fragments move out in all directions towards the cortex (figures 2.12 and 2.13 on pages 56 and 57). The same result is visible in a DIC assay using yolk granules as a marker for the outward movement of centrosomal structures (figure 2.14 on page 58). Yolk granules can attach to a microtubule and sometimes move towards its minus end (in direction of the centrosome). This happens in a dynein-dependent fashion [64]. However, yolk granule movement away from the centrosome is never observed (see for example the movie "Ch1M02 WT Anaphase DIC.mov"). Following OICD, yolk granules, which are presumably still attached to microtubules, flow away from the centrosome in all directions, sometimes even reaching the cell cortex. From this result it is concluded that there is no confined cortical site of force generation, instead the force generating interactions are distributed all over the cell cortex in the one cell stage *C. elegans* embryos. Also, microtubule polymerization forces are ruled out to be the driving force for anaphase spindle pole positioning due to the *outward* flow of yolk granules.

In the case of the stationary anterior spindle pole, OICD results in a symmetric outward flow of yolk granules, whereas for the moving posterior spindle pole the flow of granules is biased in the direction of movement (figure 2.17 on page 62). This result is interpreted in the following way: a spindle pole could be stably positioned by active pulling from all directions, whereas an imbalance, possibly resulting from the selective detachment or attachment of microtubules to the cortex, would result in a net active force in the direction of the bias. Oscillatory behavior would result if the imbalance changes with the position and speed of the spindle pole.

However, such an interpretation implies a relationship between the measured speed of a granule in a specific direction and an active force exerted in that direction. This relationship can only be discussed in terms of a detailed model, which needs to consider that the disintegration of a centrosome is not instantaneous and that centrosomal fragments are possibly interconnected by branches of microtubules, as can be seen in figure 2.12 (page 56). However, a larger active force in a given direction is likely to result in a faster outward flow of yolk granules in that direction following OICD.

The average radial distribution of yolk granule flow displays a dip along the AP axis in the direction of the anterior cortex (figure 2.17 on page 62). This effect may result from a previous displacement of the spindle towards the posterior cortex, which might have caused detachment of some of the astral microtubules radiating from the anterior spindle pole in the direction opposite to the displacement. Also, the average speed $\bar{v}$ of yolk granules flowing outward after OICD of the posterior centrosome is only 17% higher than $\bar{v}$ for anterior centrosome disintegrations (section 2.3.2), implying that the basic mechanisms of cortical force generation may be similar at the anterior and the posterior cortex.

In summary, both microtubule asters are under tensile stress as the whole cortex is capable of generating force. Oscillations are the result of an imbalance of forces acting on a particular spindle pole, as demonstrated by figure 2.17 (page 62). The imbalance of forces acting on the posterior spindle pole compared to the balanced situation at the anterior is presumed to be due to either a change in behavior of the astral microtubules, or a change in the behavior of the cortical interactions. Interestingly, the cortex is equally divided by the localization of PAR-2 and PAR-3 (figure 1.9 on page 24), consequently cell polarity could modify the behavior of these interactions in a manner compatible with these localizations.

Heterotrimeric G proteins and their activators are involved in cortical force generation

To study the function of AGS-3, an activator of G-protein mediated signalling, OICD experiments were performed for the anterior and the posterior centrosome in *ags-3* (RNAi) embryos, and the results are compared to OICD experiments in *par-2* mutant embryos (section 2.3.2). In both cases, the spindle stays symmetrically positioned throughout anaphase, and neither spindle pole undergoes transverse oscillations. In *par-2*, this is presumed to be due to a lack of establishing polarity along the anterior-posterior axis, which results in equal net active forces being exerted on both spindle poles throughout anaphase. In *ags-3* (RNAi) embryos, however, markers of polarity such as PAR-2 and PAR-3 are properly localized (Kelly Colombo, personal communication).

Similar to the OICD of the anterior spindle pole in the wild-type embryo, yolk granules move out towards the cortex in a symmetric fashion following OICD of either centrosome in *par-2* mutant embryos (figure 2.19 on page 65). However, yolk granules *do not flow outward at all* after OICD of either centrosome in *ags-3* (RNAi) embryos. The average speed $\bar{v}$ of yolk granule flow after OICD of either centrosome in wild-type and in *par-2* mutant embryos is on average above $0.1\,{}^{\mu\mathrm{m}}/_{\mathrm{s}}$; this value is reduced to less than $0.03\,{}^{\mu\mathrm{m}}/_{\mathrm{s}}$ for either centrosome following OICD in *ags-3* (RNAi) embryos. From this result it is concluded that AGS-3 is required for cortical force generation. The spindle stays symmetrically positioned in these cases, because microtubule polymerization forces together with the elastic properties of microtubules will drive the spindle to a symmetric position within the embryo. Interestingly, AGS-3 is enriched in cortical domains, therefore it could interact with astral microtubules reaching the cortex (Kelly Colombo, personal communication). Because AGS-3 functions in activating the Gα-subunits of heterotrimeric G proteins, the lack of the two relevant Gα proteins is also expected to result in the inability of cortical force generation, especially since the DIC phenotype is identical to *ags-3* (RNAi).

In summary, it was shown that upon removal of AGS-3, no forces are generated at the cortex.

Central features of anaphase spindle positioning are reproduced in a simple model in which the rate of microtubule detachment is decreased for cortical regions towards which the spindle pole is moving

Chapter 3 presents a phenomenological model capable of reproducing essential features of anaphase spindle positioning.

In this simplified model, a limited number of cortical anchor points are presumed to be responsible for the centering capabilities of a spindle pole (figure 1.4 c on page 16). The behavior of cortical elements with time, consisting of connectors generating pulling forces if a microtubule attaches, describes the system (figure 3.1 on page 69). Each active connector generates forces of equal size, independent of spindle pole speed and position. The model predicts the movement of spindle poles resulting from the *on* and *off* rates of cortical microtubule attachment and detachment and the variation of these rates with position and velocity of spindle poles (equations 3.1 and 3.2 on page 71).

It is possible for a spindle pole to stably position itself at the center of a circular geometry (figure 3.2 on page 73). Oscillatory motion results if the rates of microtubule detachment from the cortex are changed such that the rate drops for a particular cortical element if the spindle pole is moving towards it (figure 3.2 on page 73). In other words, if a spindle pole moves in a particular direction, more microtubules are being attached and are pulling in the regions towards which the spindle pole is moving. At the same time, fewer microtubules remain attached in cortical regions the spindle pole moves away from. These properties amplify an initial displacement by increasing the net force in the direction of movement, thereby generating an unstable situation which results in circular motion of a spindle pole within a circular geometry. The dependency of the detachment rate on the position and the direction of movement of the spindle pole is governed by the variable ζ, which is referred to as the *regulator of oscillatory motion*.

The geometry is adapted to the shape of an embryo without the variation of any other parameters. For the anterior half of the cortex, where PAR-3 is localized, the rates of attachment and detachment are independent of the movement of a spindle pole (the regulator of oscillatory motion in the anterior half ζ_1 is set to 0.05). For the posterior half, where PAR-2 is localized, these rates change as described above ($\zeta_2 = 1$). The anterior spindle pole is assumed to interact only with the PAR-3 region of the cortex, whereas the posterior spindle pole interacts only with the PAR-2 region. Microtubules radiating out from the posterior centrosome and connecting to the PAR-3 region of the cell cortex (and vice-versa) are not considered. To reproduce spindle pole behavior following spindle severing in the wild-type embryo (section 2.2), the rigid body constraint (the spindle) is removed at the time $t = 0\,\mathrm{s}$. This results in an immediate outward movement of both spindle poles in the model (figure 3.3 on page 74), in accordance with the experimental results. Furthermore, the posterior spindle pole travels both faster and further than the anterior one, and it undergoes transverse oscillations, whereas the anterior spindle pole stably positions itself. Taken together, essential features of

spindle pole behavior following the physical removal of the spindle midzone in the experiment are reproduced in the phenomenological model.

The model is then used to predict the behavior of the two spindle poles in the unperturbed wild-type embryo without changing any other parameters. Two more assumptions need to be made: first, the spindle midzone elongates upon tensile stress with a friction coefficient of β_s. Second, the regulator of oscillatory motion ζ_2 for the posterior cortex is linearly increased with time as to mimic the metaphase to anaphase transition, whereas it is constant for the anterior cortex ($\zeta_1 = 0.05$). Applying these settings results in an elongation of the spindle towards the posterior of the embryo concomitant with an increase of transverse oscillations of the posterior spindle pole (figure 3.4 on page 75), similar to what is observed for the wild-type one cell stage *C. elegans* embryo undergoing anaphase (figure 1.7 on page 22). Furthermore, the radial distribution of forces acting on the posterior of the spindle pole displays an asymmetry towards the direction of movement (figure 3.4 d on page 75), similar to what is observed for the radial speed distribution of yolk granule flow following OICD of the posterior centrosome in the wild-type embryo (figure 2.17 on page 62).

In summary, the phenomenological model demonstrates that it is possible to link the generation of oscillatory motion to the displacement of the mitotic spindle towards the posterior of the embryo. The model is compatible with the observation that forces acting on spindle poles are generated all over the cortex in a global fashion (section 2.3). Notably, the properties of the interactions between microtubules and the cortex vary according to the distribution of markers of polarity, which is the most obvious way of keeping the process of asymmetric spindle positioning under control of cell polarity. By stabilizing the interactions at the anterior (a previously proposed function of PAR-3 [115, 119, 151]) and destabilizing them at the posterior, the posterior spindle pole becomes oscillatory, tending to be positioned closer to the cortex and thereby dragging the whole spindle towards the posterior cortex. It should be noted, however, that the model presented is only capable of reproducing the general behavior (compare tables 3.1 and 3.2 on pages 68 and 76). More sophisticated models, involving the biophysical properties of the molecular components, need to be developed to reproduce the observations in a more quantitative manner.

5 Summary

The technique of rigid body constraint removal has been applied to test for the existence of tensile stress within the mitotic spindle at the times of metaphase and anaphase in the asymmetrically dividing one cell stage *C. elegans* embryo. These experiments revealed that there are active forces acting on both spindle poles, which increase from metaphase to anaphase. In the dynamic situation following spindle severing, a larger net force is acting on the posterior spindle pole than on its anterior counterpart. The magnitude of these active forces is under the control of genes involved in the establishment of overall cell polarity. It is presumed that these forces act to position the spindle appropriately in the asymmetrically dividing embryo.

Furthermore, by performing OICD experiments it is revealed that each individual microtubule aster is under tensile stress, as active forces pulling on the spindle poles are generated all over the cell cortex. There is no confined site of cortical force generation. Interestingly, a continuous imbalance of forces results in the oscillatory behavior observed for the posterior spindle pole, whereas the anterior spindle pole is positioned stably through a balanced distribution of radial forces acting upon it. The magnitude of the forces involved are similar for the anterior and the posterior spindle pole, indicating that similar mechanisms might be acting in generating these forces.

A simple model, describing the dynamics of the interactions between microtubules and the cell cortex, is capable of reproducing essential features of spindle positioning. In this model, cell polarity changes the properties of these interactions in a manner compatible with the distribution of markers of cell polarity. The anterior cell cortex is assumed to stabilize the interactions between the cell cortex and the microtubules, whereas the posterior cell cortex displays weaker interactions. These are such that the net force is increased in the direction of movement, resulting in an oscillatory behavior. Oscillations are linked to the generation of asymmetry in spindle positioning, as the oscillatory posterior spindle pole is capable of generating a larger pulling force in the direction of the posterior cortex, thereby displacing the whole spindle structure.

This study can serve as a basis for further investigations on more detailed aspects of the mechanics involved in spindle positioning as well as further functional studies revealing the contributions of different proteins to the process of asymmetric spindle positioning. An understanding of the underlying mechanical principles is necessary for an accurate characterization of the molecular components. Accordingly, AGS-3, an activator of G-protein mediated signalling, has been demonstrated to be required for the generation of the cortical forces by performing OICD experiments.

It is necessary to define all the molecular components involved in asymmetric spindle positioning [55]. Most importantly, the molecular nature of the complexes involved in cortical force generation at the one cell stage are unknown. Dynein is most likely to be involved. OICD experiments are a promising tool for analyzing the role of dynein in cortical force generation. Furthermore, OICD could help to identify the function of ZYG-8 in the context of asymmetric spindle positioning. In a *zyg-8* mutant embryo, the whole mitotic spindle suddenly accelerates towards the posterior cortex [152]. It is possible to detect variations in the distribution of actively pulling interactions between the astral microtubules and the cell cortex in *zyg-8* mutant embryos by OICD.

To study the dynamics of all constituents of the mitotic spindle, one would ideally want to be capable of imaging the process with high spatial and temporal resolution. This would lead to a complete picture as to how, for example, the microtubules dynamically assemble into the mitotic spindle, which then elongates and is displaced towards the posterior. However, to fully understand these processes it is necessary to perturb the system in a controlled manner and to look at the system response. Models are selected upon the capability to predict the experimental outcome. In a similar manner, genetic perturbations are utilized in biological experiments for studying the response of an organism to the loss of one of its proteins. For these reasons it is presumed that methods similar to the technique of "UV laser rigid body constraint removal" will be an effective tool for future research of the mechanics of complex biological processes, as they present a simple way of contact-free mechanical perturbation.

To conclude, the basic mechanical principles acting as to position the mitotic spindle asymmetrically in the one cell stage *C. elegans* embryo have been investigated, a process which is at the heart of generating cellular diversity in a developing organism.

6 Appendix

6.1 Methods

In this section some of the methods used in the course of the work are presented in more detail.

Culture conditions, strains and recordings

Basic methods of *C. elegans* culture and handling were as previously described [149]. Strains carrying the following mutations were used: *daf-7* (e1372) *par-2* (it5) III [120] and *par-3* (it71) *unc-32* (e189)/qC1 [119, 153]. Embryos derived from homozygous mutant mothers are referred to as "mutant embryos". Wild-type and *par-3* worms were grown at 16^oC. *par-2* worms were grown at 16^oC until L3, and then shifted to 24.5^oC. Transgenic embryos expressing GFP-α-tubulin (th2) [142] were grown at 24.5^oC. Sample preparation and time-lapse DIC recordings at two frames per second followed standard procedures [149]. Polarity of the embryos was determined in all cases by examining the position of the male pronucleus, which defines the posterior of the embryo [103].

UV laser spindle severing experiments

Experiments were performed using a commercially available laser microdissection apparatus (PALM Mikrolaser Technologie GmbH). The pulsed N2 laser ($\lambda = 337\,\mathrm{nm}$) is focused into a spot with a diameter of about $1.5\,\mu\mathrm{m}$ in the focal plane (using the following objective lens: Fluar 100x, NA 1.3, oil immersion, Zeiss). *C. elegans* embryos were mounted on the inverted microscope (Axiovert 100, Zeiss) and as soon as a slight transverse movement of the posterior spindle pole became visible, indicating the beginning of anaphase B, about 10 shots at 30 Hz were applied to the spindle midzone. If the same number of shots were applied to regions between the spindle and the cell cortex, an increase of pole-to-pole distance was not observed. The time lapse video sequences were recorded on a Macintosh G3 using the NIH

Image program version 1.62 (US National Institutes of Health). For analyzing the data, the position of both spindle poles were manually tracked in the DIC recordings using a custom made NIH Image macro. Data was analyzed using Mathematica 4.0 (Wolfram Research, Inc.), where all the parameters presented (such as spindle pole peak velocity) were computed. Importantly, tracking data was smoothed using an eight-frame running average filter as this gave consistent results for repeated tracking of movies.

RNA-mediated interference

Double-stranded RNA-mediated interference (RNAi) was performed using standard procedures [142, 55]. After preparation of double-stranded RNA (dsRNA) to the genes K11D9.1 (*CeMCAK*, primers aattaaccctcactaaaggtcctgttcgtatggctcctc and taatacgactcactataggtcctctttgagcccaacaac), F58B6.3 (*par-2*, primers aattaaccctcactaaaggtctcaaaactcggccacata and taatacgactcactataggacctctgcccaaattttcaa), F54E7.3 (*par-3*, primers aattaaccctcactaaaggttttccttccgagaccttcc and taatacgactcactatagggtgaccggacgtgaaactg), and C38C10.4 (*ags-3.3*, primers aattaaccctcactaaaggtctggcagcagacagttcag and taatacgactcactataggagcatgtgattccacacgtc) following [142] the dsRNA is injected into the gonad of the mother worm. After about 24 hours the newly fertilized embryos lack the protein to which the dsRNA corresponds [101]. The embryos are extracted from the mother after 24-26 hours and further analyzed either by fixation and staining or by UV laser irradiation experiments. It should be noted that the genes C38C10.4 (*ags-3.3*) and F22B7.13 (*ags-3.2*) are indistinguishable by RNAi due to the 98% sequence identity. The RNAi phenotype is expected to correspond to the loss-of-function phenotype of both genes together. In this context, "*ags-3*" refers to both of these genes.

Single-embryo indirect immunofluorescence

Indirect immunofluorescence of single embryos was carried out with some modifications to allow visualization of single embryos at defined stages [83]. A $24 \times 60\,\mathrm{mm}^2$ coverslip (Gold Seal, Fischer Scientific GmbH) is coated with 1% poly-L-lysine (Sigma, P1524) in PBS, after a small region on the back of the coverslip had been marked using a diamond glass cutter. One single pronuclear migration stage embryo together with a multicellular control embryo is pipetted onto the marked area of the coverslip. The single cell stage embryo is imaged on the inverted microscope, and time-lapse image sequences are recorded. At the time of anaphase, the spindle midzone is irradiated, when applicable. The coverslip immersion fluid is wiped off, and

the embryo is immediately frozen on a block of dry ice. It is crucial to keep the time between UV laser irradiation and freezing small (typically below 20 s). Care has to be taken, however, as the coverslips are very fragile. The embryos are then fixed by a "freeze-crack" procedure, as previously described [149]. Antibody staining follows standard methods [149], using the antitubulin monoclonal DM1α (Sigma-Aldrich) [142] and antibodies to ZYG-9 (a gift from A. Pozniakovsky, Max-Planck Institute of Molecular Cell Biology and Genetics, Dresden, Germany) [150]. Images are recorded using a widefield DeltaVision microscope (Applied Precision, Inc.) and deconvolved [142].

Single particle tracking of yolk granules

Yolk granules are automatically tracked from the DIC image series at two frames per second using the following algorithm: The embossing effect viewable in images recorded in DIC transmission [154] is undone by displacing the image along the DIC displacement axis and subtracting it from the original image. The resulting image is smoothed using a 3×3 pixel running average filter. Then a threshold is applied, and the center of gravity of the signal above the threshold is computed. Yolk granules of which the center of gravity is displaced by more than 0.5 μm in 0.5 s are excluded from the analysis, as speeds of that magnitude are expected to be the result of active transport. Granules that could not be tracked for less than 25 s were also excluded from further analysis. Please refer to "Ch2M09 Tracked YG.mov" for an animation of a tracked yolk granule using the SPT algorithm (scale bar: 2 μm). The tracking data was submitted to a mean-square-displacement analysis as described in section 2.1. Mathematica 4.0 (Wolfram Research, Inc.) was used for this analysis.

Optically induced centrosome disintegration

At the time of late anaphase, when the posterior spindle pole undergoes prominent transverse oscillations, 100 UV laser pulses at 50 Hz were shot at the desired centrosome while the microscope stage was rapidly moved around the borders of a $2 \times 2\,\mu$m rectangle. As the laser is focused into a fixed point in the focal plane of the sample, the boundaries of a $2 \times 2\,\mu$m area are irradiated. Microscope control and time lapse video sequences recording was performed using a PC computer (Dell) running an adapted version of the CCC software (Nick Salmon and Alfons Riedinger, EMBL Heidelberg). 15 yolk granules around the centrosome were manually tracked in the DIC recordings using a custom made NIH Image macro. Data was analyzed using Mathematica 4.0 (Wolfram Research, Inc.) as described in section 2.3.

6.2 Abbreviations

A	anterior
ADP	adenosine diphosphate
AP	anterior-posterior
ATP	adenosine triphosphate
CD	centrosome disintegration
DIC	differential interference contrast
DNA	deoxyribonucleic acid
GDP	guanosine diphosphate
GFP	green fluorescent protein
GTP	guanosine triphosphate
MAP	microtubule associated protein
MSD	mean square displacement
MTOC	microtubule organizing center
NA	numerical aperture
OICD	optically induced centrosome disintegration
P	posterior
RNA	ribonucleic acid
dsRNA	double-stranded RNA
RNAi	dsRNA mediated interference
SDC	spinning disk confocal
SPT	single particle tracking
TA	transverse asymmetry
UV	ultraviolet
WT	wild-type

Bibliography

[1] G. M. Cooper: *The cell: A molecular approach, second edition* (ASM Press, Washington DC, 2000).

[2] B. Alberts, D. Bray, J. Lewis, M. Raff, K. Roberts, and J. D. Watson: *Molecular biology of the cell* (Garland Publishing, New York, 1994).

[3] G. Woehlke and M. Schliwa: Walking on two heads: the many talents of kinesin, Nature Reviews Molecular Cell Biology **1**, 50 (2000).

[4] D. J. Sharp, G. C. Rogers, and J. M. Scholey: Microtubule motors in mitosis, Nature **407**, 41 (2000).

[5] J. C. Waters and E. D. Salmon: Pathways of spindle assembly, Current Opinion in Cell Biology **9**, 37 (1997).

[6] T. Gaglio, A. Saredi, J. B. Bingham, M. J. Hasbani, S. R. Gill, T. A. Schroer, and D. A. Compton: Opposing motor activities are required for the organization of the mammalian mitotic spindle pole, Journal of Cell Biology **135**, 399 (1996).

[7] F. J. Nedelec, T. Surrey, A. C. Maggs, and S. Leibler: Self-organization of microtubules and motors, Nature **389**, 305 (1997).

[8] T. Surrey, F. Nedelec, S. Leibler, and E. Karsenti: Physical properties determining self-organization of motors and microtubules, Science **292**, 1167 (2001).

[9] T. J. Mitchison and E. D. Salmon: Mitosis: a history of division, Nature Cell Biology **3**, E17 (2001).

[10] M. Osborn and K. Weber: Cytoplasmic microtubules in tissue culture cells appear to grow from an organizing structure towards the plasma membrane, Proceedings of the National Academy of Sciences of the United States of America **73**, 867 (1976).

[11] D. R. Kellogg, M. Moritz, and B. M. Alberts: The centrosome and cellular-organization, Annual Review of Biochemistry **63**, 639 (1994).

[12] P. Gönczy and A. Hyman: Cortical domains and the mechanisms of asymmetric cell division, Trends in Cell Biology **6**, 382 (1996).

[13] E. G. Conklin: Effects of centrifugal force on the structure and development of the egg of *Crepidula*, Journal of Experimental Zoology **22**, 311 (1917).

[14] R. Rappaport: Cytokinesis in animal cells, International Review of Cytology **31**, 169 (1971).

[15] D. Albertson: Formation of the first cleavage spindle in nematode embryos, Developmental Biology **101**, 61 (1984).

[16] R. Rappaport: Establishment of the mechanism of cytokinesis in animal cells, International Review of Cytology **105**, 245 (1986).

[17] S. Strome: Determination of cleavage planes, Cell **72**, 3 (1993).

[18] J. White and S. Strome: Cleavage plane specification in *C. elegans*: How to divide the spoils, Cell **84**, 195 (1996).

[19] J. A. Kaltschmidt, C. M. Davidson, N. H. Brown, and A. H. Brand: Rotation and asymmetry of the mitotic spindle direct asymmetric cell division in the developing central nervous system, Nature Cell Biology **2**, 7 (2000).

[20] A. Desai and T. J. Mitchison: Microtubule polymerization dynamics, Annual Review of Cell and Developmental Biology **13**, 83 (1997).

[21] T. Mitchison and M. Kirschner: Dynamic instability of microtubule growth, Nature **312**, 237 (1984).

[22] R. A. Walker, E. T. O'Brien, N. K. Pryer, M. F. Soboeiro, W. A. Voter, H. P. Erickson, and E. D. Salmon: Dynamic instability of individual microtubules analyzed by video light microscopy: rate constants and transition frequencies, Journal of Cell Biology **107**, 1437 (1988).

[23] T. Horio and H. Hotani: Visualization of the dynamic instability of individual microtubules by dark-field microscopy., Nature **321**, 605 (1986).

[24] F. Verde, M. Dogterom, E. Stelzer, E. Karsenti, and S. Leibler: Control of microtubule dynamics and length by cyclin A-dependent and cyclin B-dependent kinases in *Xenopus* egg extracts, Journal of Cell Biology **118**, 1097 (1992).

[25] R. Tournebize, S. S. L. Andersen, F. Verde, M. Doree, E. Karsenti, and A. A. Hyman: Distinct roles of PP1 and PP2A-like phosphatases in control of microtubule dynamics during mitosis, Embo Journal **16**, 5537 (1997).

[26] C. Walczak, T. Mitchison, and A. Desai: XKCM1: A *Xenopus* kinesin-related protein that regulates microtubule dynamics during mitotic spindle assembly, Cell **84**, 37 (1996).

[27] A. Desai, S. Verma, T. J. Mitchison, and C. E. Walczak: Kin I kinesins are microtubule-destabilizing enzymes, Cell **96**, 69 (1999).

[28] D. L. Gard and M. W. Kirschner: A microtubule-associated protein from *Xenopus* eggs that specifically promotes assembly at the *plus-end*, Journal of Cell Biology **105**, 2203 (1987).

[29] R. Tournebize, A. Popov, K. Kinoshita, A. J. Ashford, S. Rybina, A. Pozniakovsky, T. U. Mayer, C. E. Walczak, E. Karsenti, and A. A. Hyman: Control of microtubule dynamics by the antagonistic activities of XMAP215 and XKCM1 in *Xenopus* egg extracts, Nature Cell Biology **2**, 13 (2000).

[30] K. Kinoshita, I. Arnal, A. Desai, D. N. Drechsel, and A. A. Hyman: Reconstitution of physiological microtubule dynamics using purified components, Science **294**, 1340 (2001).

[31] R. J. Vasquez, D. L. Gard, and L. Cassimeris: XMAP from *Xenopus* eggs promotes rapid plus end assembly of microtubules and rapid microtubule polymer turnover, Journal of Cell Biology **127**, 985 (1994).

[32] M. Caplow, R. L. Ruhlen, and J. Shanks: The free energy for hydrolysis of a microtubule-bound nucleotide triphosphate is near zero: All of the free energy for hydrolysis is stored in the microtubule lattice, Journal of Cell Biology **127** (1994).

[33] T. Hill and M. Kirschner: Bioenergetics and kinetics of microtubule and actin filament assembly-disassembly, International Review of Cytology **78**, 1 (1982).

[34] S. Inoue and E. D. Salmon: Force generation by microtubule assembly disassembly in mitosis and related movements, Molecular Biology of the Cell **6**, 1619 (1995).

[35] J. Howard: *Mechanics of motor proteins and the cytoskeleton* (Sinauer Associates, Sunderland, 2001).

[36] A. Mogilner and G. Oster: The polymerization ratchet model explains the force-velocity relation for growing microtubules, European Biophysics Journal with Biophysics Letters **28**, 235 (1999).

[37] H. Felgner, R. Frank, and M. Schliwa: Flexual rigidity of microtubules measured with the use of optical tweezers, Journal of Cell Science **109**, 509 (1996).

[38] M. Kurachi, M. Hoshi, and H. Tashiro: Buckling of a single microtubule by optical trapping forces: direct measurement of microtubule rigidity, Cell Motility and the Cytoskeleton **30**, 221 (1995).

[39] M. Dogterom and B. Yurke: Measurement of the force-velocity relation for growing microtubules, Science **278**, 856 (1997).

[40] G. S. van Doorn, C. Tanase, B. M. Mulder, and M. Dogterom: On the stall force for growing microtubules, European Biophysics Journal with Biophysics Letters **29**, 2 (2000).

[41] M. Dogterom and S. Leibler: Physical aspects of the growth and regulation of microtubule structures, Physical Review Letters **70**, 1347 (1993).

[42] M. Dogterom and B. Yurke: Microtubule dynamics and the positioning of microtubule organizing centers, Physical Review Letters **81**, 485 (1998).

[43] M. S. Hamaguchi and Y. Hiramoto: Analysis of the role of astral rays in pronuclear migration in sand dollar eggs by the colcemid-UV method, Development Growth & Differentiation **28**, 143 (1986).

[44] U. Euteneuer and M. Schliwa: Evidence for an involvement of actin in the positioning and motility of centrosomes, Journal of Cell Biology **101**, 96 (1985).

[45] U. Euteneuer and M. Schliwa: Mechanism of centrosome positioning during the wound response in BSC-1 cells, Journal of Cell Biology **116** (1992).

[46] T. E. Holy, M. Dogterom, B. Yurke, and S. Leibler: Assembly and positioning of microtubule asters in microfabricated chambers, Proceedings of the National Academy of Sciences of the United States of America **94**, 6228 (1997).

[47] K. Visscher, M. J. Schnitzer, and S. M. Block: Single kinesin molecules studied with a molecular force clamp, Nature **400**, 184 (1999).

[48] K. Svoboda and S. M. Block: Force and velocity measured for single kinesin molecules, Cell **77**, 773 (1994).

[49] H. Kojima, E. Muto, H. Higuchi, and T. Yanagida: Mechanics of single kinesin molecules measured by optical trapping nanometry, Biophysical Journal **73**, 2012 (1997).

[50] K. Kawaguchi and S. Ishiwata: Temperature dependence of force, velocity, and processivity of single kinesin molecules, Biochemical and Biophysical Research Communications **272**, 895 (2000).

[51] E. Meyhöfer and J. Howard: The force generated by a single kinesin molecule against an elastic load, Proceedings of the National Academy of Sciences of the United States of America **92**, 574 (1995).

[52] F. Gittes, E. Meyhöfer, S. Baek, and J. Howard: Directional loading of the kinesin motor molecule as it buckles a microtubule, Biophysical Journal **70**, 418 (1996).

[53] A. J. Hunt, F. Gittes, and J. Howard: The force exerted by a single kinesin molecule against a viscous load, Biophysical Journal **67**, 766 (1994).

[54] G. Steinberg and M. Schliwa: Characterization of the biophysical and motility properties of kinesin from the fungus *Neurospora crassa*, Journal of Biological Chemistry **271**, 7516 (1996).

[55] P. Gönczy, C. Echeverri, K. Oegema, A. Coulson, S. J. M. Jones, R. R. Copley, J. Duperon, J. Oegema, M. Brehm, E. Cassin, E. Hannak, M. Kirkham, S. Pichler, K. Flohrs, A. Goessen, S. Leidel, A.-M. Alleaume, C. Martin, N. Özlü, P. Bork, and A. A. Hyman: Functional genomic analysis of cell division in *C. elegans* using RNAi of genes on chromosome III, Nature **408**, 331 (2000).

[56] M. A. McNiven, M. Wang, and K. R. Porter: Microtubule polarity and the direction of pigment transport reverse simultaneously in surgically severed melanophore arms, Cell **37**, 753 (1984).

[57] M. A. McNiven and K. R. Porter: Organization of microtubules in centrosome-free cytoplasm, Journal of Cell Biology **106**, 1593 (1988).

[58] M. Ueda, R. Graf, H. K. MacWilliams, M. Schliwa, and U. Euteneuer: Centrosome positioning and directionality of cell movements, Proceedings of the National Academy of Sciences of the United States of America **94**, 9674 (1997).

[59] S. C. Schuyler and D. Pellman: Search, capture and signal: games microtubules and centrosomes play, Journal of Cell Science **114**, 247 (2001).

[60] C. B. O'Connell and Y. L. Wang: Mammalian spindle orientation and position respond to changes in cell shape in a dynein-dependent fashion, Molecular Biology of the Cell **11**, 1765 (2000).

[61] J. L. Carminati and T. Stearns: Microtubules orient the mitotic spindle in yeast through dynein-dependent interactions with the cell cortex, Journal of Cell Biology **138**, 629 (1997).

[62] S. Busson, D. Dujardin, A. Moreau, J. Dompierre, and J. R. De Mey: Dynein and dynactin are localized to astral microtubules and at cortical sites in mitotic epithelial cells, Current Biology **8**, 541 (1998).

[63] M. P. Koonce, J. Kohler, R. Neujahr, J. M. Schwartz, I. Tikhonenko, and G. Gerisch: Dynein motor regulation stabilizes interphase microtubule arrays and determines centrosome position, Embo Journal **18**, 6786 (1999).

[64] P. Gönczy, S. Pichler, M. Kirkham, and A. A. Hyman: Cytoplasmic dynein is required for distinct aspects of MTOC positioning, including centrosome separation, in the one cell stage *Caenorhabditis elegans* embryo, Journal of Cell Biology **147**, 135 (1999).

[65] M. McGrail and T. S. Hays: The microtubule motor cytoplasmic dynein is required for spindle orientation during germline cell divisions and oocyte differentiation in *Drosophila*, Development **124**, 2409 (1997).

[66] A. R. Skop and J. G. White: The dynactin complex is required for cleavage plane specification in early *Caenorhabditis elegans* embryos, Current Biology **8**, 1110 (1998).

[67] A. A. Hyman: Centrosome movement in the early divisions of *Caenorhabditis elegans*: a cortical site determining centrosome position, Journal of Cell Biology **109**, 1185 (1989).

[68] L. Lee, J. Tirnauer, J. Li, S. Schuyler, J. Liu, and D. Pellman: Positioning of the mitotic spindle by a cortical-microtubule capture mechanism, Science **287**, 2260 (2000).

[69] W. Korinek, M. Copeland, A. Chaudhuri, and J. Chant: Molecular linkage underlying microtubule orientation toward cortical sites in Yeast, Science **287**, 2257 (2000).

[70] D. L. Beach, J. Thibodeaux, P. Maddox, E. Yeh, and K. Bloom: The role of Kar9p and Myo2 in orienting the mitotic spindle in budding yeast., Current Biology **10**, 1497 (2000).

[71] B. M. McCartney, D. G. McEwen, E. Grevengoed, P. Maddox, A. Bejsovec, and M. Peifer: *Drosophila* APC2 and Armadillo participate in tethering mitotic spindles to cortical actin, Nature Cell Biology **3**, 933 (2001).

[72] R. K. Miller, K. K. Heller, L. Frisen, D. L. Wallack, D. Loayza, A. E. Gammie, and M. D. Rose: The kinesin-related proteins, Kip2p and Kip3p, function differently in nuclear migration in yeast, Molecular Biology of the Cell **9**, 2051 (1998).

[73] R. A. Heil-Chapdelaine, N. K. Tran, and J. A. Cooper: Dynein-dependent movements of the mitotic spindle in *Saccharomyces cerevisiae* do not require filamentous actin, Molecular Biology of the Cell **11**, 863 (2000).

[74] L. Lee, S. K. Klee, M. Evangelista, C. Boone, and D. Pellman: Control of mitotic spindle position by the *Saccharomyces cerevisiae* formin Bni1p, Journal of Cell Biology **142**, 1501 (1999).

[75] R. Miller, D. Matheos, and M. Rose: The cortical localization of the microtubule orientation protein, Kar9p, is dependent upon actin and proteins required for polarization, Journal of Cell Biology **144**, 963 (1999).

[76] H. Yin, D. Pruyne, T. C. Huffaker, and A. Bretscher: Myosin V orients the mitotic spindle in yeast, Nature **406**, 1013 (2000).

[77] V. Allan and S. Näthke: Catch and pull a microtubule: getting a grasp on the cortex, Nature Cell Biology **3**, E226 (2001).

[78] P. Polakis: Wnt signaling and cancer, Genes & Development **14**, 1837 (2000).

[79] B. M. McCartney and M. Peifer: Teaching tumour suppressors new tricks, Nature Cell Biology **2**, E58 (2000).

[80] L. A. Ligon, S. Karki, M. Tokito, and E. L. F. F. Holzbaur: Dynein binds to beta-catenin and may tether microtubules at adherens junctions, Nature Cell Biology **3**, 913 (2001).

[81] P. T. Tran, L. Marsh, V. Doye, S. Inoue, and F. Chang: A mechanism for nuclear positioning in fission yeast based on microtubule pushing, Journal of Cell Biology **153**, 397 (2001).

[82] N. Bresgen, G. Czihak, and J. Linhart: Computer modeling of blastoderm formation in *Drosophila*, Naturwissenschaften **81**, 417 (1994).

[83] S. W. Grill, P. Gönczy, E. H. K. Stelzer, and A. A. Hyman: Polarity controls forces governing asymmetric spindle positioning in the *Caenorhabditis elegans* embryo, Nature **409**, 630 (2001).

[84] N. Schultz and A. Onfelt: Spindle positioning in fibroblasts supports an astral microtubule length dependent force generation at the basal membrane, Cell Motility and the Cytoskeleton **50**, 69 (2001).

[85] S. Reinsch and P. Gönczy: Mechanisms of nuclear positioning, Journal of Cell Science **111**, 2283 (1998).

[86] J. R. Aist and M. W. Berns: Mechanics of chromosome separation during mitosis in *Fusarium* (Fungi imperfecti): new evidence from ultrastructural and laser microbeam experiments, Journal of Cell Biology **91**, 446 (1981).

[87] R. J. Leslie and H. J. Pickett: Ultraviolet microbeam irradiations of mitotic diatoms: investigation of spindle elongation, Journal of Cell Biology **96**, 548 (1983).

[88] J. R. Aist, H. Liang, and M. W. Berns: Astral and spindle forces in PtK2 cells during anaphase B: a laser microbeam study, Journal of Cell Science **104**, 1207 (1993).

[89] J. C. Waters, R. W. Cole, and C. L. Rieder: The force-producing mechanism for centrosome separation during spindle formation in vertebrates is intrinsic to each aster, Journal of Cell Biology **122**, 361 (1993).

[90] L. D. Landau and E. Lifshitz: *Mechanics, third edition* (Pergamon Press, Oxford, 1976).

[91] H. Goldstein: *Classical Mechanics* (Addison-Wesley, Reading, Massachusetts, 1950).

[92] E. Wilson: *The cell in development and heredity* (Macmillan Inc, New York, 1925).

[93] C. Staiger: Cell division in plants, Current Opinion in Cell Biology **5**, 226 (1993).

[94] H. Horvitz and I. Herskowitz: Mechanisms of asymmetric cell division: two Bs or not two Bs, that is the question, Cell **68**, 237 (1992).

[95] S. Cohen and A. A. Hyman: Cell fate determination - when is a determinant a determinant, Current Biology **4**, 420 (1994).

[96] J. A. Knoblich: Asymmetric cell division during animal development, Nature Reviews Molecular Cell Biology **2**, 11 (2001).

[97] C. Q. Doe and B. Bowerman: Asymmetric cell division: fly neuroblast meets worm zygote, Current Opinion in Cell Biology **13**, 68 (2001).

[98] W. Wood: Introduction to *C. elegans* biology, in *The nematode Caenorhabditis elegans*, edited by W. Wood (Cold Spring Harbor Laboratory Press, 1988), pp. 1–16.

[99] J. E. Sulston, E. Schierenberg, J. G. White, and J. N. Thomson: The embryonic cell lineage of the nematode *Caenorhabditis elegans*, Developmental Biology **100**, 64 (1983).

[100] The *C. elegans* sequencing consortium: Genome sequence of the nematode *C. elegans*: a platform for investigating biology., Science **282**, 2012 (1998).

[101] A. Fire, S. Xu, M. K. Montgomery, S. A. Kostas, S. E. Driver, and C. C. Mello: Potent and specific genetic interference by double-stranded RNA in *Caenorhabditis elegans*, Nature **391**, 806 (1998).

[102] M. Gotta and J. Ahringer: Axis determination in *C. elegans*: initiating and transducing polarity, Current Opinion in Genetics & Development **11**, 367 (2001).

[103] B. Goldstein and S. Hird: Specification of the anteroposterior axis in *Caenorhabditis elegans*, Development **122**, 1467 (1996).

[104] S. Hird and J. White: Cortical and cytoplasmic flow polarity in early embryonic cells of *Caenorhabditis elegans*, Journal of Cell Biology **121**, 1343 (1993).

[105] D. Hill and S. Strome: An analysis of the role of microfilaments in the establishment and maintenance of asymmetry in *Caenorhabditis elegans* zygotes, Developmental Biology **125**, 75 (1988).

[106] D. Hill and S. Strome: Brief cytochalasin-induced disruption of microfilaments during a critical interval in 1-cell *C. elegans* embryos alters the partitioning of developmental instructions to the 2-cell embryo, Development **108**, 159 (1990).

[107] K. Kemphues and S. Strome: Fertilization and establishment of polarity in the embryo, in *C. elegans II*, edited by D. Riddle, T. Blumenthal, B. Meyer, and J. Priess (Cold Spring Harbor Laboratory Press, 1997), pp. 335–359.

[108] P. L. Sadler and D. C. Shakes: Anucleate *Caenorhabditis elegans* sperm can crawl, fertilize oocytes and direct anterior-posterior polarization of the 1- cell embryo, Development **127**, 355 (2000).

[109] K. F. O'Connell, K. N. Maxwell, and J. G. White: The spd-2 gene is required for polarization of the anteroposterior axis and formation of the sperm asters in the *Caenorhabditis elegans* zygote, Developmental Biology **222**, 55 (2000).

[110] M. R. Wallenfang and G. Seydoux: Polarization of the anterior-posterior axis of *C. elegans* is a microtubule-directed process, Nature **408**, 89 (2000).

[111] A. A. Hyman and J. G. White: Determination of cell division axes in the early embryogenesis of *Caenorhabditis elegans*, Journal of Cell Biology **105**, 2123 (1987).

[112] S. Guo and K. J. Kemphues: *par-1*, a gene required for establishing polarity in c-elegans embryos, encodes a putative Ser/Thr kinase that is asymmetrically distributed, Cell **81**, 611 (1995).

[113] D. J. Levitan, L. Boyd, C. C. Mello, K. J. Kemphues, and D. T. Stinchcomb: par-2, a gene required for blastomere asymmetry in *Caenorhabditis elegans*, encodes zinc-finger and ATP-binding motifs, Proceedings of the National Academy of Sciences of the United States of America **91**, 6108 (1994).

[114] L. Boyd, S. Guo, D. Levitan, D. T. Stinchcomb, and K. J. Kemphues: PAR-2 is asymmetrically distributed and promotes association of P granules and PAR-1 with the cortex in *C. elegans* embryos, Development **122**, 3075 (1996).

[115] B. Etemad-Moghadam, S. Guo, and K. Kemphues: Asymmetrically distributed PAR-3 protein contributes to cell polarity and spindle alignement in early *C. elegans* embryos, Cell **83**, 743 (1995).

[116] T. J. Hung and K. J. Kemphues: PAR-6 is a conserved PDZ domain-containing protein that colocalizes with PAR-3 in *Caenorhabditis elegans* embryos, Development **126**, 127 (1999).

[117] Y. Tabuse, Y. Izumi, F. Piano, K. J. Kemphues, J. Miwa, and S. Ohno: Atypical protein kinase C cooperates with PAR-3 to establish embryonic polarity in *Caenorhabditis elegans*, Development **125**, 3607 (1998).

[118] K. Kemphues: PARsing embryonic polarity, Cell **101**, 345 (2000).

[119] N. Cheng, C. Kirby, and K. Kemphues: Control of cleavage spindle orientation in *Caenorhabditis elegans*: the role of the genes par-2 and par-3, Genetics **139**, 549 (1995).

[120] K. Kemphues, J. Priess, D. Morton, and N. Cheng: Identification of genes required for cytoplasmic localization in early *C. elegans* embryos, Cell **52**, 311 (1988).

[121] R. R. Zwaal, J. Ahringer, H. G. van Luenen, A. Rushforth, P. Anderson, and R. H. Plasterk: G proteins are required for spatial orientation of early cell cleavages in C. elegans embryos, Cell **86**, 619 (1996).

[122] M. Gotta and J. Ahringer: Distinct roles for G alpha and G beta gamma in regulating spindle position and orientation in *Caenorhabditis elegans* embryos, Nature Cell Biology **3**, 297 (2001).

[123] A. R. Bausch, F. Ziemann, A. A. Boulbitch, K. Jacobson, and E. Sackmann: Local measurements of viscoelastic parameters of adherent cell surfaces by magnetic bead microrheometry, Biophysical Journal **75**, 2038 (1998).

[124] F. H. C. Crick and A. F. W. Hughes: The physical properties of cytoplasm: a study by the meanch of the magnetic particle method, Experimental Cell Research **1**, 37 (1949).

[125] F. Ziemann, J. Radler, and E. Sackmann: Local measurements of viscoelastic moduli of entangled actin networks using an oscillating magnetic bead micro-rheometer, Biophysical Journal **66**, 2210 (1994).

[126] A. Ashkin, J. M. Dziedzic, and T. Yamane: Optical trapping and manipulation of single cells using infrared-laser beams, Nature **330**, 769 (1987).

[127] A. Ashkin and J. M. Dziedzic: Optical trapping and manipulation of viruses and bacteria, Science **235**, 1517 (1987).

[128] S. M. Block, D. F. Blair, and H. C. Berg: Compliance of bacterial flagella measured with optical tweezers, Nature **338**, 514 (1989).

[129] E. L. Florin, A. Pralle, J. K. H. Horber, and E. H. K. Stelzer: Photonic force microscope based on optical tweezers and two- photon excitation for biological applications, Journal of Structural Biology **119**, 202 (1997).

[130] A. Rohrbach and E. H. K. Stelzer: Optical trapping of dielectric particles in arbitrary fields, Journal of the Optical Society of America A **18**, 839 (2001).

[131] E. L. Florin, V. T. Moy, and H. E. Gaub: Adhesion forces between individual ligand-receptor pairs, Science **264**, 415 (1994).

[132] A. Ashkin, K. Schütze, J. M. Dziedzic, U. Euteneuer, and M. Schliwa: Force generation of organelle transport measured *in vivo* by an infrared-laser trap, Nature **348**, 346 (1990).

[133] V. T. Moy, E. L. Florin, and H. E. Gaub: Intermolecular forces and energies between ligands and receptors, Science **266**, 257 (1994).

[134] E. Evans, K. Ritchie, and R. Merkel: Sensitive force technique to probe molecular adhesion and structural linkages at biological interfaces, Biophysical Journal **68**, 2580 (1995).

[135] A. Pralle, P. Keller, E. L. Florin, K. Simons, and J. K. H. Horber: Sphingolipid-cholesterol rafts diffuse as small entities in the plasma membrane of mammalian cells, Journal of Cell Biology **148**, 997 (2000).

[136] L. D. Landau and E. M. Lifshitz: *Theory of elasticity* (Pergamon Press, Oxford, 1959).

[137] N. W. Tschoegl: *The phenomenological theory of linear viscoelastic behavior* (Springer-Verlag, Heidelberg, 1989).

[138] A. R. Bausch, W. Moller, and E. Sackmann: Measurement of local viscoelasticity and forces in living cells by magnetic tweezers, Biophysical Journal **76**, 573 (1999).

[139] L. Eichinger, B. Koppel, A. A. Noegel, M. Schleicher, M. Schliwa, K. Weijer, W. Witke, and P. A. Janmey: Mechanical perturbation elicits a phenotypic difference between *Dictyostelium* wild-type cells and cytoskeletal mutants, Biophysical Journal **70**, 1054 (1996).

[140] N. Q. Balaban, U. S. Schwarz, D. Riveline, P. Goichberg, G. Tzur, I. Sabanay, D. Mahalu, S. Safran, A. Bershadsky, L. Addadi, and B. Geiger: Force and focal adhesion assembly: a close relationship studied using elastic micropatterned substrates, Nature Cell Biology **3**, 466 (2001).

[141] A. Maniotis and M. Schliwa: Microsurgical removal of centrosomes blocks cell reproduction and centriole generation in BSC-1 cells, Cell **67**, 495 (1991).

[142] K. Oegema, A. Desai, S. Rybina, M. Kirkham, and A. A. Hyman: Functional analysis of kinetochore assembly in *Caenorhabditis elegans*, Journal of Cell Biology **153**, 1209 (2001).

[143] K. O. Greulich: *Micromanipulation by light in biology and medicine - the laser microbeam and optical tweezers* (Birkhaeuser Verlag, Basel, 1998).

[144] H. Qian, M. P. Sheetz, and E. L. Elson: Single partical tracking (Analysis of diffusion and flow in two dimensional systems), Biophysical Journal **60**, 910 (1991).

[145] A. Kusumi, Y. Sako, and M. Yamamoto: Confined lateral diffusion of membrane receptors as studied by single particle tracking (nanovid microscopy). Effects on calcium-induced differentiationin cultured epethelial cells, Biophysical Journal **65**, 2021 (1993).

[146] J. A. Steyer: *Beobachtung exozytischer Vesikel mit Totalreflexionsfluoreszenz - Mikroskopie* (doctoral thesis, Ruprecht-Karls-Universität Heidelberg, 1997).

[147] L. Wordeman and T. Mitchison: Identification and partial characterisation of mitotic centromere-associated kinesin, a kinesin-related protein that associates with centromeres during mitosis, Journal of Cell Biology **128**, 95 (1995).

[148] H. Wein, M. Foss, B. Brady, and W. Cande: DSK1, a novel kinesin-related protein from the diatom *Cylindrotheca fusiformis* that is involved in anaphase spindle elongation, Journal of Cell Biology **133**, 595 (1996).

[149] P. Gönczy, H. Schnabel, T. Kaletta, A. D. Amores, T. Hyman, and R. Schnabel: Dissection of cell division processes in the one cell stage *Caenorhabditis elegans* embryo by mutational analysis, Journal of Cell Biology **144**, 927 (1999).

[150] E. Hannak, M. Kirkham, A. A. Hyman, and K. Oegema: Aurora-A kinase is required for centrosome maturation in *Caenorhabditis elegans*, Journal of Cell Biology **155**, 1109 (2001).

[151] L. S. Rose and K. Kemphues: The let-99 gene is required for proper spindle orientation during cleavage of the *C. elegans embryo*, Development **125**, 1337 (1998).

[152] P. Gönczy, J. M. Bellanger, M. Kirkham, A. Pozniakowski, K. Baumer, J. B. Phillips, and A. A. Hyman: *zyg-8*, a gene required for spindle positioning in *C. elegans*, encodes a doublecortin-related kinase that promotes microtubule assembly, Developmental Cell **1**, 363 (2001).

[153] D. Morton, J. Roos, and K. Kemphues: par-4, a gene required for cytoplasmic localisation and determination of specific cell types in *Caenorhabditis elegans* embryogenesis, Genetics **130**, 771 (1992).

[154] C. J. Cogswell and C. J. R. Sheppard: Confocal differential interference contrast (DIC) microscopy - including a theoretical-analysis of conventional and confocal DIC imaging, Journal of Microscopy-Oxford **165**, 81 (1992).

Publications

S. W. Grill, P. Gönczy, E. H. K. Stelzer, and A. A. Hyman: Polarity controls forces governing asymmetric spindle positioning in the *Caenorhabditis elegans* embryo, Nature **409**, 630 (2001).

P. Gönczy, S. Grill, E. H. K. Stelzer, M. Kirkham, and A. A. Hyman: Spindle positioning during the asymmetric first cell division of *C. elegans* embryos, Cell Cycle and Development (Novartis Foundation Symposium) **237**, 164 (2001).

Acknowledgments

I would like to thank

Professor Erich Sackmann for acting as the external supervisor of my thesis;

Tony Hyman and Ernst Stelzer for giving me a chance to work in their research laboratories at the EMBL in Heidelberg and later at the MPI in Dresden, for their ideal supervision, and for their endless support;

Pierre Gönczy for teaching me everything and for driving the project forward by his immense support and help;

the former and current members of the Stelzer laboratory for the great atmosphere and all the help, in particular Samo Fisinger, Ernst-Ludwig Florin, Jan Huisken, James Jonkman, Regine Neubecker, Alexander Rohrbach, Nick Salmon, Jim Swoger, and Jamie White;

the former and current members of the Hyman laboratory for all the help and all the fun, in particular Mark van Breugel, Carrie Cowan, Arshad Desai, Chris Echeverri, Eva Hannak, Kazu Kinoshita, Matthew Kirkham, Karen Oegema, Nurhan Özlü, Sophie Quintin, Andrej Pozniakovsky, Sonja Rybina, Stephanie Schoenegg, Anne Schwager and Martin Srayko;

the members of the electronic workshop at the EMBL, in particular Alfons Riedinger and Georg Ritter;

Anne Ephrussi and Mattias Hentze for the EMBL PreDoc course;

and finally Thomas, Celia, Sylvia, Valentina, Antonio, Tobi, Uwe the world-champion, Peter, Jens, Giovanni, Valeria, Michel, Cagla, Philipp, Rebecca, Paolo, and Karo.